THE PARAMETER SPACE BOUNDARY FOR ESCAPE AND CHAOS IN THE DUFFING TWIN-WELL OSCILLATOR

A thesis presented in partial

fulfilment of the requirements

for the degree

of doctor of philosophy

in Physics at

Massey University

Christopher I. Reid

November 1999

Contents

List of Tables

List of Figures

Abstract

The Duffing 'twin-well' oscillator is investigated both experimentally and theoretically. The construction of a physical, nonlinear air-track oscillator with an ultrasound position detection system permits observation of a wide range of oscillatory behaviours, including chaotic motion, on a human scale (amplitudes of ~metre).

Phase space and Poincaré sections are constructed in real time and, in the case of chaos, Lyapunov exponents determined. The range of control space conditions which give rise to chaos is investigated. In particular, the boundaries between chaotic and periodic motion are measured experimentally.

An analytic description of the primary boundaries of interest is constructed via a harmonic-balance generated solution to the governing differential equation and a perturbation style stability analysis. Successful theoretical prediction of the chaos boundary is achieved without recourse to numerical methods.

Acknowledgements

It is a pleasure to acknowledge the contributions of the following people:

My supervisor, Dr Scott Whineray of the Department of Physics, Albany, for his guidance, wisdom and wit.

Mr Joe Wang and Dr Geoffrey Dingley of the Department of Physics who built the stepping motor drive system and controlling software described in section 2.2.

Dr Peter Kay of Computer Science, who lent valuable assistance in establishing RS-232 communication between the PC and the ultrasound detection system (section 2.3).

Professor Ian Watson for assisting with the funding of the project and Professor David Parry for his support.

Introduction

If the simple harmonic oscillator (SHO) is of central importance to physics in describing, by virtue of a (Taylor) series expansion, small oscillations in the vicinity of an equilibrium position, then, expanding the series to third order and investigating the resulting 'cubic' oscillations is a natural next step. Harmonically forced oscillations of a body, mass m, under such a restoring force are governed by Duffing's equation:

$$m\ddot{x} + \gamma\dot{x} - \alpha x + \beta x^3 = \Gamma cos\omega t \tag{0.1}$$

where $x = x(t)$ is the position of the body and the Greek symbols denote parameters of the system. In particular, viscous damping is characterised by γ and the excitation by Γ and ω (respectively, forcing amplitude and frequency). Systems modelled by equation 0.1 exhibit a rich spectrum of phenomena including subharmonics, hysteresis, coexistence and chaos. What oscillations are possible depends on the parameters.

Duffing's [8] seminal work of 1918 establishes relationships between the frequency and amplitude of periodic oscillations, relationships which he tested using pendulum-spring combinations. Such apparatus allows investigation of the case $\alpha < 0$, $\beta > 0$ (significant linear term, small cubic term) and slight damping.

Our interest is specifically the case where α and β are both positive. This gives rise to the so-called 'twin-well' potential, a system intuitively described by a 'ball' confined to the symmetric potential depicted in figure 0.1. The linear term in the restoring force contributes the 'hump' to the otherwise quartic potential. The system has three equilibria, one unstable at $x = 0$, and two stable at $x = \pm\sqrt{\alpha/\beta}$ where the opposing linear and cubic components of the restoring force cancel.

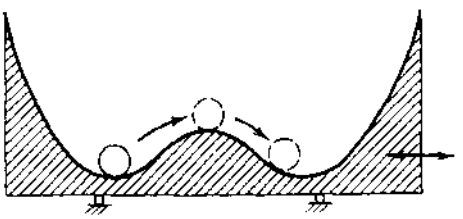

Figure 0.1: Intuitive representation of a twin-well potential system.

To maintain motion in the face of light frictional damping, the system is driven harmonically, the ball making cross-well transitions if it has sufficient energy.

Experimental Duffing oscillators are rare. Previous experimental systems have most often been achieved with a 'bending beam' apparatus. A twin-well potential, in such cases, is established by making use of an external attractive field. Thus Moon [18], for example, establishes a twin-well potential by suspending a 'hack-saw' blade over two separated magnets - while Berger and Nunes [4] upright the blade, making use of gravity to create the twin-well effect. Our air-track based system employs springs and rods to effect a cubic restoring force and makes use of an external field (gravity) to drive the oscillation. This latter technique minimises the possibility of introducing a significant and negative α.

That chaotic oscillations occur in the Duffing twin well system is well established ([29], [13], [18]). Less well understood is the range of parameter values which give rise to chaos and the boundary(s) in parameter space which mark its onset. Varying only the forcing amplitude and frequency, the onset of chaos is marked by a line in the (ω, Γ) plane (Moon [18], [20]). This line is seen in figure 0.2 as the 'V-shape' located near $\omega = \nu = 0.8$, $F = 0.07$, where parameter values below the line give rise to periodic motion in one well and those above, double-well chaos.

Moon's [19] experimental results suggest a possible fractal character to the boundary, yet it is easily verified numerically, and we find *via* experiment, that this is not the case.

There have been several efforts made to analytically predict the chaos boundary, most notably Kapitaniak [16], Janicki and Szemplińska-Stupnicka [14], Moon

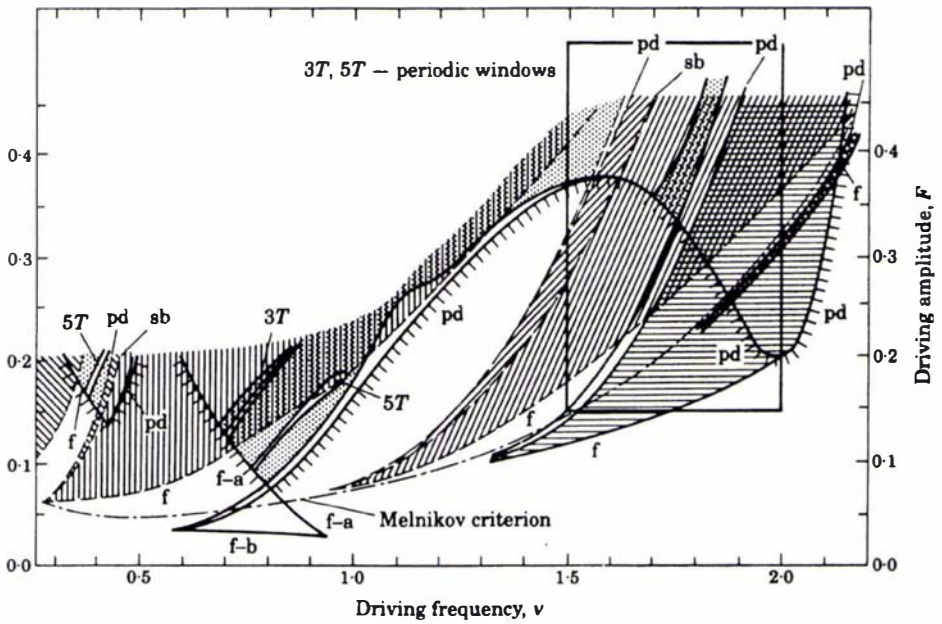

Figure 4. Regions of existence of various attractors in the control space. ▥, $1T$ SO exists below this line; ▤, $2T$ SO; ▩, $3T$ SO; ▥ $1T$ LO symmetric; ▧, $1T$ LO unsymmetric; ■, $3T$ LO symmetric; ▨, $3T$ LO unsymmetric; ■ cross-well chaos. Bifurcations: f—fold (saddle-node), pd—period doubling, sb—symmetry breaking.

Figure 0.2: Numerical results reproduced from figure 4, Janicki and Szemplińska-Stupnicka [14] for parameter values $\alpha = 0.5$, $\beta = 0.5$ and $\gamma = 0.1$.

[18], [19], Holmes [13] and Guckenheimer and Holmes [11]. Of these, [16] and [14] are the most successful, but both, crucially, depend on numerical methods at some point.

The aims of this thesis, then, are broadly these:

1. Construction of an experimental Duffing twin-well oscillator, enabling measurement of the (ω, Γ) plane chaos boundary, and,
2. Mathematically modelling the system to obtain a theoretical prediction of the above boundary.

It is emphasised that the theoretical component of the project is not intended to be a rigorous mathematical analysis. Indeed, high levels of rigour are unlikely to produce useful results - as one may observe from the Holmes-Melnikov criterion for the above boundary (refer [20], [11] or section 4.2.2). Here, we are led by the experimental results and, through valid approximations, develop models which predict the observed behaviour.

Chapter 1

Cubic Oscillations

1.1 Cubic Oscillators

Experimental observation of cubic oscillations is achieved with an air track and glider, using a position dependent restoring force on the glider established by the rod/spring configuration shown in figure 1.3. Here the springs, tensioned vertically and at a perpendicular distance L from the air track, are connected to the glider by rods of length l. The springs have length $2l_s$ when at rest and tension[1] T_0.

The restoring force on the glider is then:

$$f = -4T_0 sin\theta cos\psi \tag{1.2}$$

[1]Strictly speaking, the spring tension is y dependent. If the springs have force constant k, and unstretched length l_w, then the spring tension is $T_y = (2\sqrt{y^2 + l_s^2} - l_w)/k$ which, if y is small becomes $T_0 = (2l_s - l_w)/k$, that is, a constant. We make this assumption.

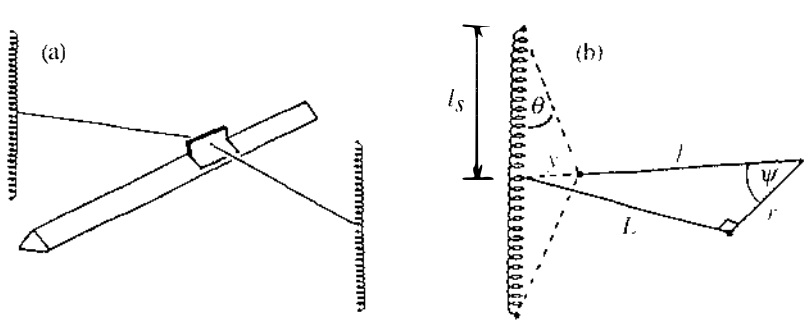

Figure 1.3: Spring geometry (a) Glider orientation (b) Variables defined.

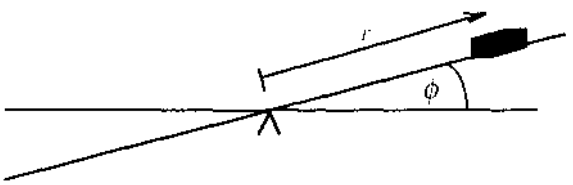

Figure 1.4: Glider coordinates defined.

$$(l+y)^2 = r^2 + L^2 \tag{1.3}$$

rearranging 1.3, we find, for small y:

$$y = \frac{r^2 + L^2 - l^2}{2l} \tag{1.4}$$

eliminating ψ, θ, and y we find for $r^2 << (L^2 + l^2)$

$$f(r) = W_0 \frac{(l^2 - L^2)r - r^3}{(l^2 + L^2)l_s} \tag{1.5}$$

$f(r)$ therefore has the form

$$f(r) = \alpha r - \beta r^3 \tag{1.6}$$

where α and β are constants defined by equation 1.5.

Driven oscillations are achieved by 'see-sawing' the track about a central pivot. The Lagrangian for the glider, mass m, rotational inertia I, is then given by

$$L = \frac{1}{2}m\dot{r}^2 + \frac{1}{2}m(r\dot{\phi})^2 + \frac{1}{2}I\dot{\phi}^2 - mgrsin\phi - V(r) \tag{1.7}$$

where (r, ϕ) are the polar coordinates (figure 1.4) of the glider (origin at the pivot) and $V(r)$ is the potential function associated with the spring displacement. $V(r)$ is related to the spring force function, $f(r)$, by $f(r) = -dV/dr$. As the dimensions of the glider itself are small (0.3 m in length), we neglect the inertia term $\frac{1}{2}I\dot{\phi}^2$. The equation of motion for the displacement is then

$$m\ddot{r} - f(r) - mr\dot{\phi}^2 + mgsin\phi = -\gamma\dot{r} \tag{1.8}$$

where γ is the viscous drag coefficient. The sinusoidal variation of the track slope

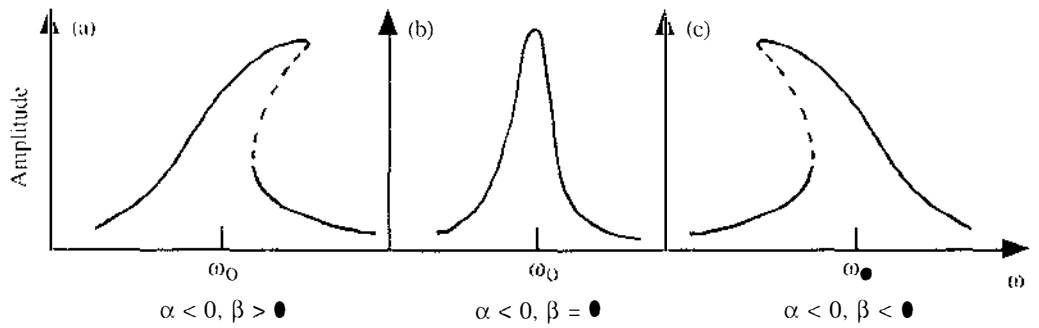

Figure 1.5: Typical response curves for (a) 'Hard' spring. (b) Linear spring. (c) 'Soft' spring.

can be expressed as

$$sin\phi = -\phi_0 cos(\omega t) \tag{1.9}$$

Thus the centrifugal term of equation 1.8 can be written

$$mr\dot{\phi}^2 = mr(\omega\phi_0 sin(\omega t))^2/(1 - \phi_0^2 cos^2(\omega t)) \tag{1.10}$$

We shall see (section 2.2) that the amplitude of the drive term, ϕ_0, never exceeds 0.08 rad. and therefore the contribution of the centrifugal term, while being ω-dependent, is negligible (for example, with $\phi_0 = 0.08$ rad, $\omega = 3$, $m = 0.352$, $r = 0.5$, $mr\omega^2{\phi_0}^2 \approx 1 \times 10^{-2}$). Neglecting the centrifugal term, the differential equation for the motion of the glider is then Duffing's equation

$$m\ddot{r} + \gamma\dot{r} - \alpha r + \beta r^3 = \Gamma cos\omega t \tag{1.11}$$

where $\Gamma = mg\phi_0$.

When $\alpha < 0$ (the normal simple harmonic oscillator case), the cases $\beta > 0$ and $\beta < 0$ correspond to third order Taylor approximations to 'hard' and 'soft' springs respectively. Of these two cases, our apparatus would permit investigation of the former by choosing the rod length l, such that $l < L$. Figure 1.5 shows the typical response curves of amplitude versus frequency of both cases with the driven simple harmonic oscillator (SHO) ($\beta = 0$) for comparison. Thus, the familiar SHO response curve 'tilts' to the right or left depending on the sign of β. In

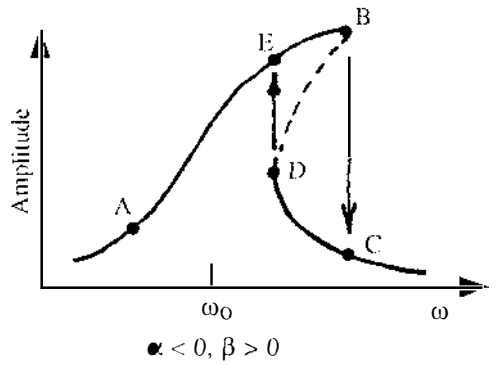

Figure 1.6: Hysteresis sequence A-B-C-D-E illustrated for the 'Hard' spring case.

each case, the response curves are centred at the linear-approximation, 'resonance' frequency, $\omega_0 = \sqrt{-4m\alpha - 2\gamma^2}/2m$.

As Γ increases so does the degree of tilt; the curves become multivalued for certain ω (as in the cases illustrated), the broken-line sections in figure 1.5 indicating unstable solutions of equation 1.11. In such cases, a hysteresis effect is observed with the amplitude making a sudden 'jump' as the frequency changes. The jump points correspond to the response curve having vertical tangents. Figure 1.6 summarises this behaviour in the case of the 'hard' spring: As ω is increased from point A, the amplitude increases until point B is reached where, having 'nowhere to go', it suffers a sudden drop to point C. Decreasing ω from this point (or any higher frequency) results in the amplitude increasing sharply until the curve is vertical - at D, whereupon it jumps up to the top - point E. An equivalent process occurs for the soft spring case.

1.2 Pure cubic oscillator

From equation 1.5 we see that when $l = L$, $\alpha = 0$ and the restoring force is purely cubic. This case is considered in Whineray [32] and Whineray *et al.* [33] for relaxation (damped, undriven) and driven oscillations respectively. The experimental response curve obtained in [33] is shown in figure 1.7. Like the 'hard' spring case, the response curve tilts to the right by comparison with the driven SHO, but, as $\alpha = 0$ there is no fixed natural frequency for small undriven oscillations.

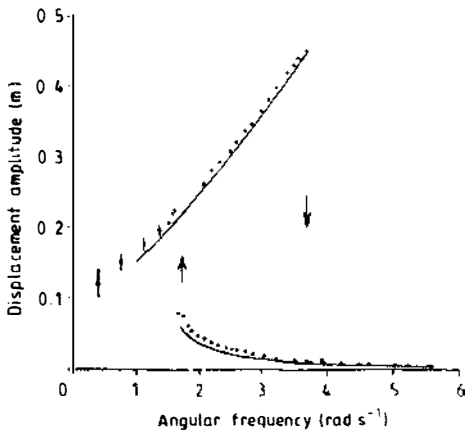

Figure 1.7: Experimental response curve from [32].

The frequency of such oscillations is amplitude dependent and has the important property that the period-amplitude product, TA is approximately constant. This accounts for the linearity evident in the amplitude-frequency plot of figure 1.7.

1.3 Duffing's method of solution

Periodic solutions $r = r(t)$ of equation 1.11 are not harmonically pure and consequently, in the preceding discussion, the term 'amplitude' has been used loosely. The presence of these higher harmonics in the solution of equation 1.11 is a direct result of the nonlinear term. An approximate method of solution, employed by Duffing [8], for the case $\gamma = 0$ illustrates this: We rewrite equation 1.11 as follows

$$m\ddot{r} = \alpha r - \beta r^3 + \Gamma cos\omega t \tag{1.12}$$

and substitute in an initial approximation to the solution, $r_1(t) = Acos\omega t$, giving

$$m\ddot{r_1} = (\alpha A - \frac{3}{4}\beta A^3 + \Gamma)cos\omega t - \frac{1}{4}\beta A^3 cos3\omega t \tag{1.13}$$

Integrating equation 1.13 twice (and dividing by m) recovers the second approximation, specifically,

$$r_2(t) = \frac{1}{m\omega^2}(\frac{3}{4}\beta A^3 - \alpha A - \Gamma)cos\omega t + \frac{1}{36m\omega^2}\beta A^3 cos3\omega t \tag{1.14}$$

The original amplitude, A, is equated to the new $cos\omega t$ coefficient giving

$$0 = \frac{3}{4}\beta A^3 - A(\alpha + m\omega^2) - \Gamma \tag{1.15}$$

This relationship between A and the parameters of the system produces curves similar to those of figure 1.5. Equation 1.14 indicates that the solution is dominated by the fundamental and hence its amplitude, A, is taken to be indicative of the 'size' of the oscillation. In the particular case of the undriven, undamped, pure cubic oscillator ($\gamma = 0$, $\alpha = 0$, $\beta > 0$, $\Gamma = 0$) of section 1.2, equation 1.15 can be rearranged to the following

$$TA = 4\pi\sqrt{\frac{m}{3\beta}} \tag{1.16}$$

where $T = 2\pi/\omega$. This is the $TA = constant$ result obtained in [33] and elsewhere via an elliptic integral. There's a pattern here: for a quadratic potential (SHO), T is constant; for an x^4 potential, TA is constant; for an x^6 potential TA^2 is constant; etc.

1.4 Twin-Well Oscillator

For $l \neq L$, the restoring force contains both linear and cubic terms, the case $l > L$ ($\alpha > 0$, $\beta > 0$), giving rise to the so-called 'twin-well' potential, $V(r) = -\int f(r)dr$, for which the rod/spring configuration has three equilibria:

$$r = 0, \pm\sqrt{l^2 - L^2} \tag{1.17}$$

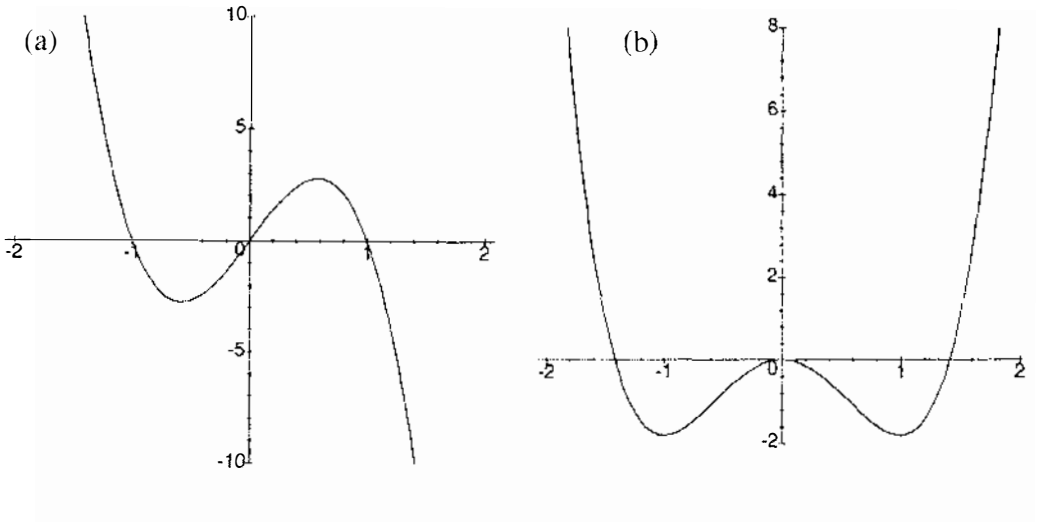

Figure 1.8: (a) Restoring force $f(x)$ *vs* x and (b) Potential $V(x)$ *vs* x for $a = 7.21$.

In considering this case, it is convenient to scale equation 1.11

$$\ddot{x} + c\dot{x} - ax(1 - x^2) = F cos\omega t \tag{1.18}$$

where $a = \alpha/m$, $c = \gamma/m$, $x = r\sqrt{3/\alpha}$ and $F = \Gamma\sqrt{3/\alpha}/m$. Now the stable equilibria are located at $x = \pm 1$, the force function is $f(x) = ax(1 - x^2)$ and the potential $V(x) = \frac{a}{4}(x^4 - 2x^2)$ (see figure 1.8). The Hamiltonian is therefore

$$H = \frac{1}{2}v^2 + \frac{a}{4}x^2(x^2 - 2) \tag{1.19}$$

It is helpful to write equation 1.18 in the following form :

$$\frac{d\mathbf{X}}{dt} = \mathbf{G}(\mathbf{X}, \mathbf{L}) \tag{1.20}$$

where $\mathbf{G}$ is a vector function of the phase-space vector $\mathbf{X} = (x, v, z)$ and the set of parameters $\mathbf{L} = (a, c, F, \omega)$. The above system of differential equations (1.20) is then

$$\begin{aligned} \dot{x} &= v \\ \dot{v} &= F cosz + ax(1 - x^2) - cv \\ \dot{z} &= \omega \end{aligned} \tag{1.21}$$

The eigenvalues of the Jacobian matrix, $\mathbf{M_{nm}} = \frac{\partial \dot{x}_n}{\partial X_m}$, determine the nature of solutions in the vicinity of critical (equilibrium) points[2]. We obtain

$$\mathbf{M} = \begin{bmatrix} 0 & 1 & 0 \\ a(1-3x^2) & -c & -Fsinz \\ 0 & 0 & 0 \end{bmatrix} \tag{1.22}$$

Consider the undriven system ($F = 0$). $\mathbf{M}$ then has two eigenvalues given by

$$\lambda = \frac{1}{2}\left(-c \pm \sqrt{c^2 + 4a(1-3x^2)}\right) \tag{1.23}$$

For the Hamiltonian case ($c = 0$) equation 1.23 gives rise to the eigenvalues $\lambda = \pm i\sqrt{2a}$, at the critical points $x = \pm 1$. This imaginary pair indicates stable centres. That is, the local solutions take the form $x = Acos\sqrt{2a}t + Bsin\sqrt{2a}t$. Thus $\sqrt{2a}$ is the natural frequency of small oscillations confined to one well.

At $x = 0$ we obtain $\lambda = \pm\sqrt{a}$, a real pair, indicating an unstable saddle point. Local solutions take the form $x = Aexp(\sqrt{a}t) + Bexp(-\sqrt{a}t)$. These local behaviours are illustrated in figure 1.9 where the curves are obtained by plotting v *vs* x for the Hamiltonian function (equation 1.19).

For $c \neq 0$, $c^2 < 8a$, the system is no longer Hamiltonian but the local behaviours can still be determined. The critical point at $x = 0$ remains a saddle, but at $x = \pm 1$, the eigenvalues are the complex conjugate pair $\lambda = \frac{1}{2}(-c \pm i\sqrt{8a - c^2})$. Here the imaginary part contributes the oscillatory character of the solution and the real part the exponential decay. Local solutions take the form $x = exp(-ct/2)(Acos\frac{1}{2}\sqrt{8a - c^2}t + Bsin\frac{1}{2}\sqrt{8a - c^2}t)$, that is, a stable spiral. The introduction of damping to the system then, has the effect of 'collapsing' the stable centres of figure 1.9 to asymptotically stable spirals. Figure 1.10 depicts the new situation where the curves indicate the local behaviour at each respective critical point.

The spirals cause adjacent trajectories to converge whereas the saddle can cause, depending on initial conditions, neighbouring trajectories to converge or

[2]Refer to Kreyszig [17] for example.

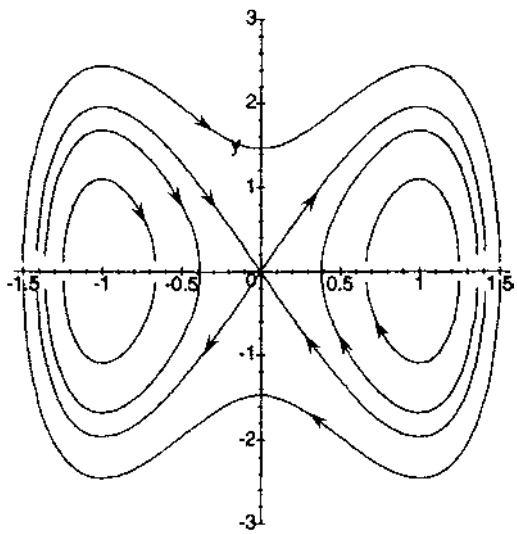

Figure 1.9: Phase plane (v *vs* x) behaviour for $c = 0$, $F = 0$, $a = 7.21$, from the Hamiltonian, equation 1.19, for $H = 1.2$, 0, -0.4 and -1.2.

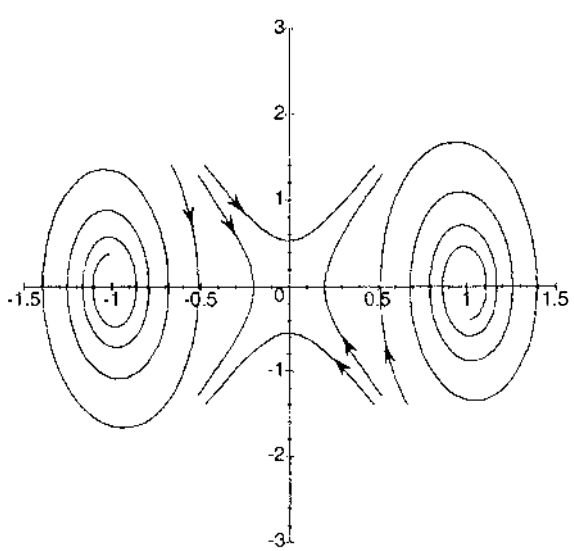

Figure 1.10: Phase plane character near critical points for $c \neq 0$, $F = 0$, $a = 7.21$.

diverge. The exponents which characterise the rate of growth or decay of the separation of neighbouring trajectories in the phase plane are the local Lyapunov exponents. Since, in general, these exponents vary throughout the phase plane, the average rate of separation 'seen' by any given orbit must be evaluated numerically along the entire trajectory. These techniques are employed in section 3.3 where such exponents are used to diagnose - i.e. provide a measure of - chaos.

When $F \neq 0$, corresponding to the driven oscillator, the solution becomes more complex. As a 'first look' we apply Duffing's method (again with $\gamma = 0$) specifically to the twin well case, starting with

$$x(t) = E + A\cos\omega t \tag{1.24}$$

Differentiating and substituting equation 1.24 in equation 1.12 gives, on expansion and use of trigonometric identities:

$$\begin{aligned}\ddot{x} = {} & F\cos(w\,t) + a\,A\cos(w\,t) + a\,E - \frac{1}{4}\,a\,A^3\cos(3\,w\,t) \\ & - \frac{3}{4}\,a\,A^3\cos(w\,t) - \frac{3}{2}\,a\,A^2\,E\cos(2\,w\,t) - \frac{3}{2}\,a\,A^2\,E - 3\,a\,A\cos(w\,t)\,E^2 \\ & - a\,E^3.\end{aligned} \tag{1.25}$$

Integrating the above twice with respect to t we obtain:

$$\begin{aligned}x = {} & (-\frac{1}{2}\,a\,E^3 + \frac{1}{2}\,a\,E - \frac{3}{4}\,a\,A^2\,E)\,t^2 + C_1 t + C_2 \\ & + (-\frac{F}{w^2} - \frac{a\,A}{w^2} + 3\,\frac{a\,A\,E^2}{w^2} + \frac{3}{4}\,\frac{a\,A^3}{w^2})\cos(w\,t) + \frac{3}{8}\,\frac{\cos(2\,w\,t)\,a\,A^2\,E}{w^2} \\ & + \frac{1}{36}\,\frac{\cos(3\,w\,t)\,a\,A^3}{w^2}\end{aligned} \tag{1.26}$$

where C_1 and C_2 are constants of the integration. Equating coefficients of equations 1.24 and 1.26, we obtain:

$$E = 0,\ E^2 = 1 - \frac{3}{2}\,A^2 \tag{1.27}$$

$$A\,w^2 = -F - a\,A + 3\,a\,A\,E^2 + \frac{3}{4}\,a\,A^3 \tag{1.28}$$

Equation 1.27 is obtained by demanding that the coefficient of t^2 in equation 1.26 be zero. Equation 1.28 results from equating the coefficient of $cos\omega t$ in equation 1.26 with A. Eliminating E from equations 1.24 and 1.28 gives

$$x(t) = \pm\sqrt{1 - \frac{3}{2}A^2} + Acos\omega t \tag{1.29}$$

$$0 = \frac{15}{4}aA^3 + A(w^2 - 2a) + F \tag{1.30}$$

Equation 1.30 relates the amplitude, A, to the parameters of the system and therefore, for $E \neq 0$, the solution $x(t)$ describes local oscillations in either well. Comparing equation 1.30 with equation 1.15 (setting $m = 1, \Gamma = F, \alpha = -2a, \beta = -5a$) , we see that the response has the character of a 'soft' spring as the β value implied is negative. We shall see (sections 4.1, 4.3) that the accuracy of equation 1.30 in describing the twin-well behaviour, while not great, does nevertheless give a qualitative indication of single well response. Roots for A in equation 1.30 for certain parameter values may be obtained via a Newton-Raphson method or other such numerical technique. As we will need to plot more complex response curves, the algorithm given in appendix B.4 was constructed. It employs interval bisection to find roots without the need for differentiation. Figure 1.11 is a plot of $|A|$ *vs* ω from equation 1.30. Similar to the response curve of a driven SHO, the lack of damping in the system causes a discontinuity in the response (unlike the continuous response peaks of figure 1.5). Thus the magnitude of A is plotted since the sign of A may be positive or negative[3]; the upper branch of the response curve has the negative sign.

1.4.1 Numerical Analysis

The smooth and continuous nature of the force function (equation 1.6) ensures that Duffing's equation (1.11) is readily integrated by numerical methods. Indeed, many studies have been based entirely on data so obtained. The paper of Ueda

[3]cf. undamped SHO response where the solution suffers a 180° phase change as the system passes through resonance.

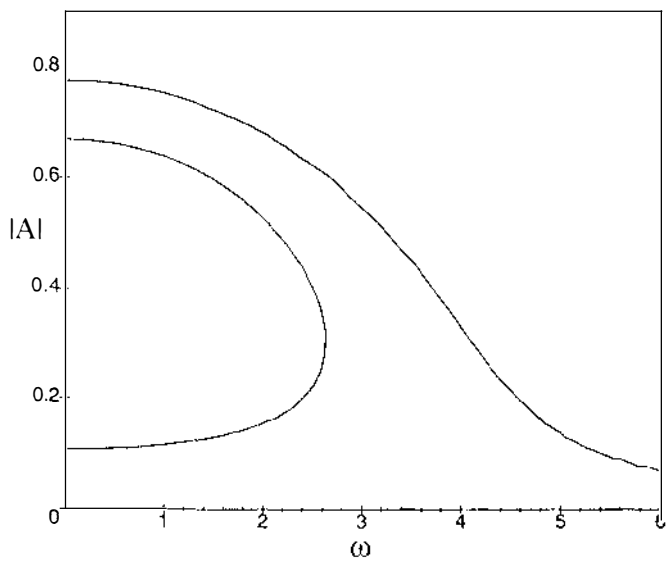

Figure 1.11: Response curve given by roots to equation 1.30 for $a = 7.21$, $F = 1.51$.

[29], for example, explores the many oscillations possible for different system parameters.

It is not the intention of the present investigation to repeat such analyses. However, occasionally, use is made of numerical algorithms for the purpose of comparison with experimental or theoretical results. An example is the chaos boundary measurement of chapter 3. Determining this boundary numerically (computer) requires changing parameters 'on the run', waiting for transient oscillations to die down and 'back-tracking' if parameter changes have been too hasty. While it is relatively simple to code numerical routines such as 'fourth-order Runge Kutta' (RK4) in a high-level programming language like *Pascal*, such algorithms do not normally afford the advanced level of user interaction here described. For this reason, use was made of the software package *Chaotic Dynamics Workbench* (CDW) [26]. CDW integrates Duffing's equation, while meeting the above requirements and displaying the phase plane trajectories in real time. The software performs RK4 integration and, when necessary, Lyapunov exponent computation is made using conventional techniques (such as the algorithm of Wolf *et al.* [36]).

Chapter 2

Experimental Apparatus

This chapter describes the nonlinear oscillator and associated apparatus used to realise, in the laboratory, the oscillations described in chapter 1 - particularly the Duffing twin-well oscillation.

The basic rod/spring configuration which gives rise to the twin well potential has been described in section 1.1. Harmonically driven oscillations in such a potential are established experimentally using an air track which pivots about its midpoint. Sinusoidal variation of the track slope, achieved using a stepping motor, applies a sinusoidal force on the glider whose position, $x(t)$, is governed by Duffing's equation 1.18. The position of the glider is measured in real time using an ultrasound detection system called V-scope [31].

2.1 Physical Description

Photographs of the apparatus are seen in figures 2.12 - 2.15. A standard laboratory air track is used, the glider is essentially a length of v-section aluminium. Air, pumped into the hollow track, escapes through small holes in the track surface. This efflux creates a cushion of air on which the glider floats. Bolted to the underside of the air track is an aluminium frame which supports the vertically oriented springs, positioned a distance L, from the track. Horizontal fibre-glass rods connect the springs to the glider and pivot freely at both ends. This entire structure (air track + frame + springs/rods + glider) is attached to a cradle and axle

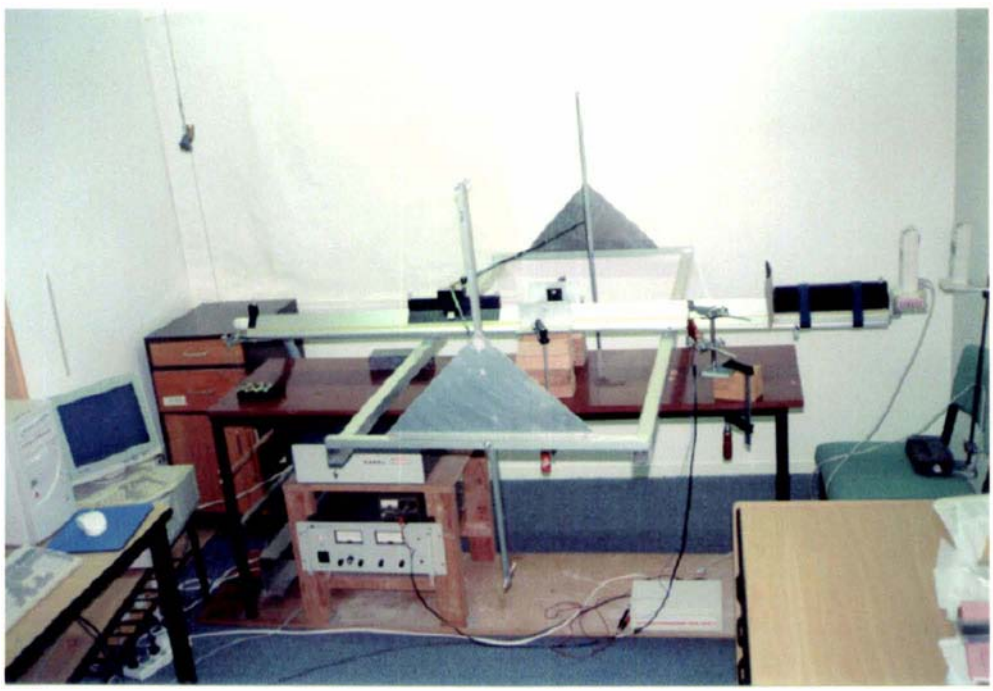

Figure 2.12: Overview of the apparatus. The stepping motor cable and counterweight are seen in the top left of the figure.

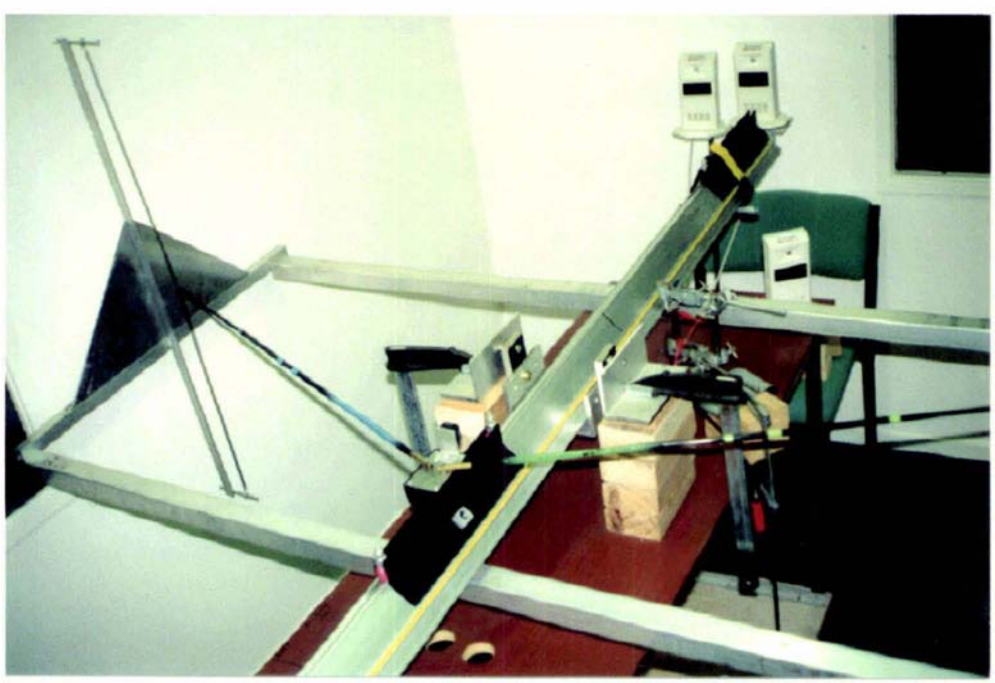

Figure 2.13: Close-up view of the air track showing the spring geometry and V-scope receiver towers.

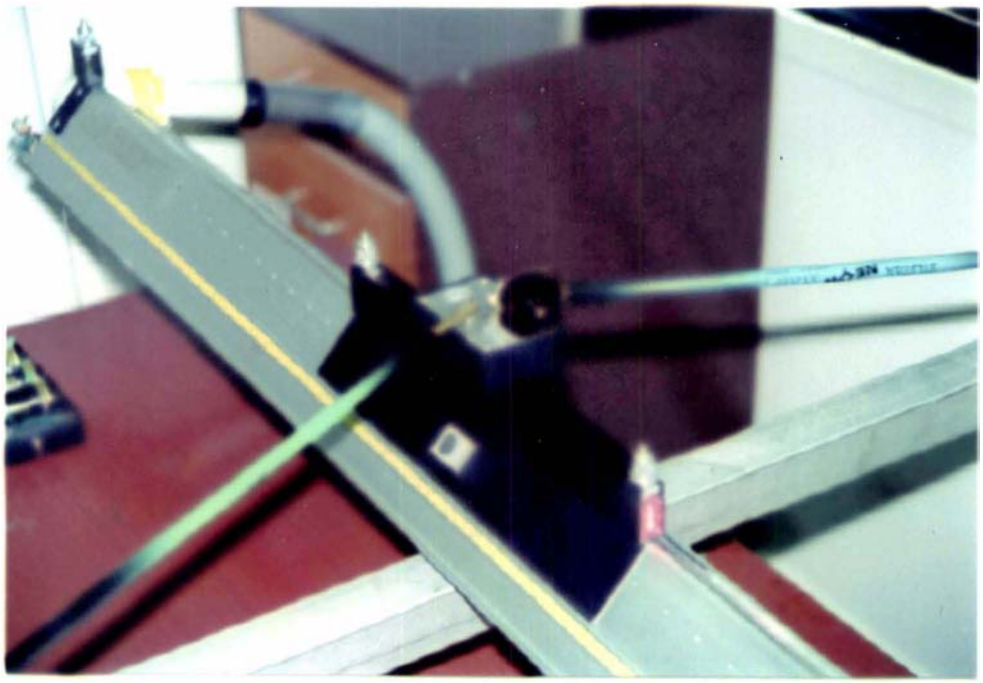

Figure 2.14: Detail of the glider showing the V-scope 'button' transmitter, rod connections and, on the side, the damping magnet attachment.

Figure 2.15: (left to right) PC2, PC1, stepping motor (between table legs, near the floor), control box, power supplies and V-scope microprocessor.

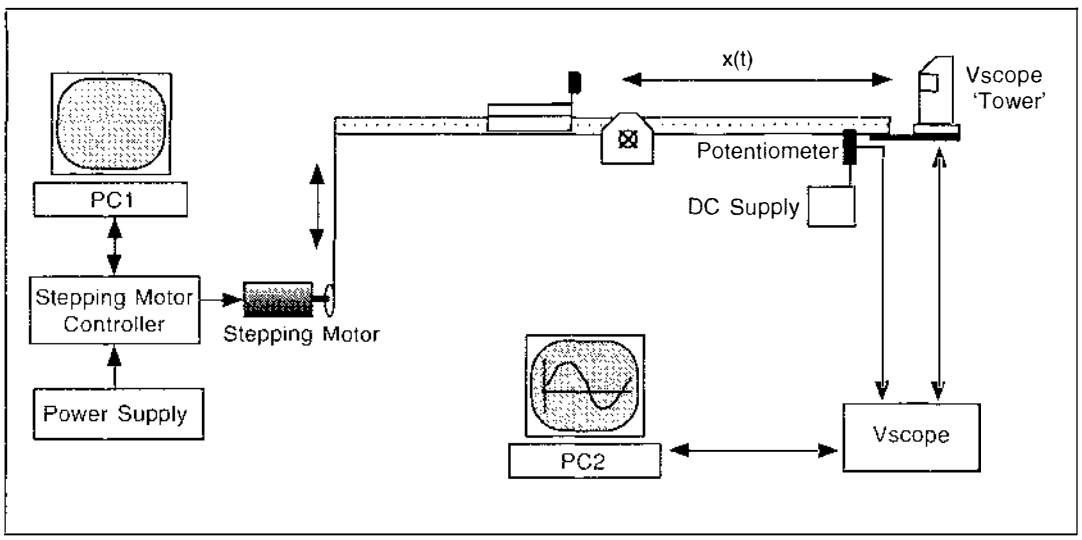

Figure 2.16: Schematic of the experimental apparatus.

with the pivot point of the axle being level with the path of the glider - thereby minimising inertial effects. A steel cable, attached to the perimeter of a wheel on the stepping motor axle leads, via pulleys on the ceiling, to a counter-weight. Part way up, the cable is attached to the end of the air track. Sinusoidal variation by the stepping motor of the cable's vertical displacement thereby translates to sinusoidal variation of the track slope and hence a sinusoidal force on the glider. This driving force is, we note, in addition to but independent of the position-dependent restoring force from the springs. A magnet attached to the side of the glider induces eddy currents in the track surface and hence damps the oscillations (see figure 2.14). Table 2.1 gives the physical dimensions of the apparatus.

Table 2.1: Apparatus Dimensions and Parameters.

Rod length	l	0.855 m
Spring position	L	0.826 m
Glider mass	m	0.352 kg
Glider length	h	0.300 m
Air track Length	L_A	2.030 m
Spring Length (Tensioned)	l_s	0.965 m

Figure 2.16 is a block diagram of the main electronic components which can be broadly divided into two groups, namely 'drive' or 'detection'. Those associated

with the driving force include a DC power supply, stepping motor and stepping motor control box which in turn is controlled by an AT computer, PC1. In addition, a small 'laser pointer' (not depicted in figure 2.16) mounted on the air track assists in levelling the track on start-up.

On the detection side is the V-scope apparatus which includes a small 'button' pulse transmitter on the glider itself and a 'tower' ultrasonic receiver at the end of the track which is connected to the V-scope microprocessor control box. This control box communicates, via RS-232 protocol, with PC2 which is a 486 DX2 66MHz IBM compatible. A linear potentiometer attached to the side of the air track provides a measure of the track slope in the form of an analogue 0-5V DC signal, which is fed into the V-scope control box analogue input.

2.2 The Stepping Motor Drive System

Previous drive systems employed electric motors attached to the end of the air track via a 'scotch yoke' mechanism (Whineray *et al.* [32], Reid and Whineray [25]). Such systems allow control of the motor speed and hence the driving frequency, ω, by variation of the supply voltage or gearing ratios. In the present work, both frequency and driving force amplitude are to be varied thereby allowing measurement of 'control space' boundaries between the oscillatory modes. This latter requirement is difficult to implement with conventional electric motors because it involves physically 're-bolting' the coupling between motor and air track for each new amplitude. Although this was attempted, it did not permit continuous variation of the forcing amplitude. Short of building a more elaborate mechanical system, a computer controlled, stepping motor system was designed. Through software control, the forcing amplitude can be set (at a resolution determined by the stepsize of the motor) while retaining continuous, 'on the run', frequency control. In addition, as this frequency is driven by the computer clock, it is very precise - an improvement on previous systems which always suffered from the minor speed fluctuations inherent in conventional electric motors.

2.2.1 Stepping Motor Control

The sinusoidal displacement of the end of the air track is obtained by controlling the timing and number of pulses to the stepping motor[1]. Low-distortion[2] sinusoidal motion is achieved when the total vertical displacement of the track end is made up of a sufficiently large number of motor steps. Table 2.2 lists the motor

Table 2.2: Parameters associated with the stepping motor system.

Shaft rotation	$\delta\phi$	0.72°/step
Wheel radius	R	39.79 mm
Vertical translation	d	0.50 mm/step
Air track 'pivot length'	l_a	1.117 m

shaft rotation per step and the wheel radius. These two parameters result in a vertical translation of $d = 0.50$ mm per step. Any output sinewave is quantised to this resolution. Thus a sinewave made up of N steps has amplitude $A = N.d$. The distance from the air track pivot to the cable attachment point is l_a and so the maximum track slope is $\phi_0 = N.d/l_a$. The amplitude of the sinusoidal force (in Newtons) exerted on the glider is then given by

$$\Gamma = mg\phi_0 = mg\frac{N.d}{l_a} \tag{2.31}$$

where m is the mass of the glider. In practice, the number of steps used never exceeded 170 and was rarely less than 50. For clarity, the example depicted in figure 2.17 is a 10-step sinewave.

The amplitude, in steps (N), and the period of the driving force are entered by the user to PC1. Software then calculates a table of stepping times and coil sequences based on the relevant sinewave. Upon running, the computer continuously loops through the table. Buttons on the control box facilitate altering the period 'on the run', a task achieved by scaling the table entries.

[1] Full details of the controlling software and hardware are to be found in Dingley *et al.* [7].
[2] The degree of distortion is considered in the next section.

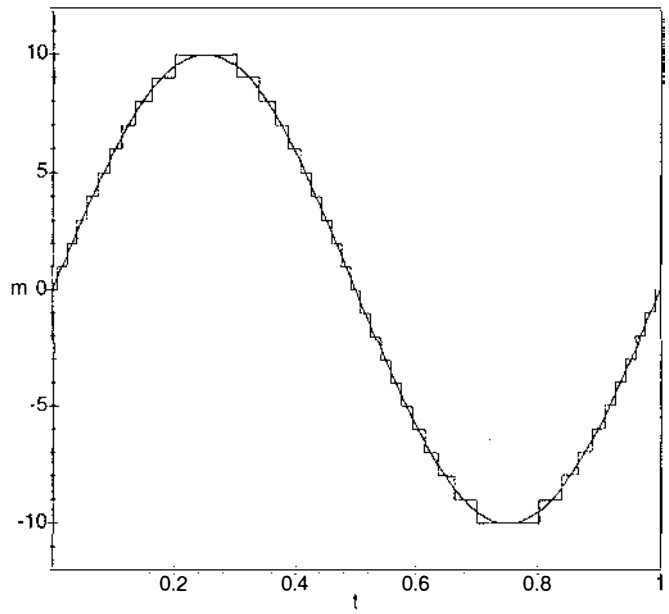

Figure 2.17: A 1 Hz 'stepped' sinewave, amplitude $N = 10$ steps, with its continuous counterpart.

2.2.2 Harmonic content of the stepped sinewave

A natural consequence of using a stepping motor is that the output 'sinewave' will contain spurious harmonics. Provided they are small however, the impurities should not have a detrimental effect on the experiment. The nature of a stepping motor demands that the sinewave is quantised by regular displacement steps at irregular points in time. The resulting Fourier spectrum is not obvious. By contrast, the perhaps more familiar case of regular time intervals (ΔT) and irregular displacements produces, in the Fourier spectrum, a well defined peak at $1/\Delta T$ Hz and multiples thereof.

In order to determine the harmonic content then, we calculate the Fourier series coefficients of the stepped sinewave, amplitude $A = N.d$ where d is the displacement stepsize and N is an integer.

We first define the square pulse $u_m(t)$ as

$$u_m(t) = \begin{cases} d & \text{when } a_m < t < \pi/\omega - a_m \\ 0 & \text{otherwise} \end{cases} \tag{2.32}$$

where

$$a_m = \frac{1}{\omega} sin^{-1}(\frac{m - \frac{1}{2}}{N}) \tag{2.33}$$

Thus the first half period of the stepped sinewave is given by

$$h(t) = \sum_{m=1}^{N} u_m(t) \tag{2.34}$$

An odd periodic extension of $h(t)$ with period $2\pi/\omega$ then gives the entire stepped sinewave. We now evaluate the Fourier series coefficients b_{nm}, for the odd periodic extension of a single pulse $u_m(t)$:

$$b_{nm} = \frac{2d\omega}{\pi} \int_{a_m}^{\pi/\omega - a_m} sin(n\omega t)dt \tag{2.35}$$

$$= \begin{cases} 0 & \text{n even} \\ \frac{4d}{n\pi} cosn\omega a_m & \text{n odd} \end{cases} \tag{2.36}$$

Summing b_{nm} over m gives, by virtue of the linearity of the Fourier representation and equation 2.34, the series coefficients, b_n, for the entire stepped sinewave:

$$b_n = \frac{4d}{n\pi} \sum_{m=1}^{N} cosn\omega a_m \tag{2.37}$$

Using equations 2.37 and 2.33, the coefficient of each harmonic can be calculated. (In particular, one may verify that $b_1 = A$ in the limit $d \to 0$). We may write the entire series as

$$y(t) = \frac{4d}{\pi} \sum_{nodd}^{\infty} \sum_{m=1}^{N} \frac{1}{n} cos(n\omega a_m) sin(n\omega t) \tag{2.38}$$

where $y(t)$ is the vertical position of the end of the air track. The full expression for the time dependent force on the glider is then

$$f(t) = mg \frac{4d}{\pi l_a} \sum_{nodd}^{\infty} \sum_{m=1}^{N} \frac{1}{n} cos(n\omega a_m) sin(n\omega t) \tag{2.39}$$

Using equations 2.37 and 2.33, the Fourier series coefficients have been evaluated for the 'worst-case' amplitude of 50 steps (refer algorithm *stepping*, appendix B.2) and their magnitudes, normalised to the fundamental are plotted in figure 2.18.

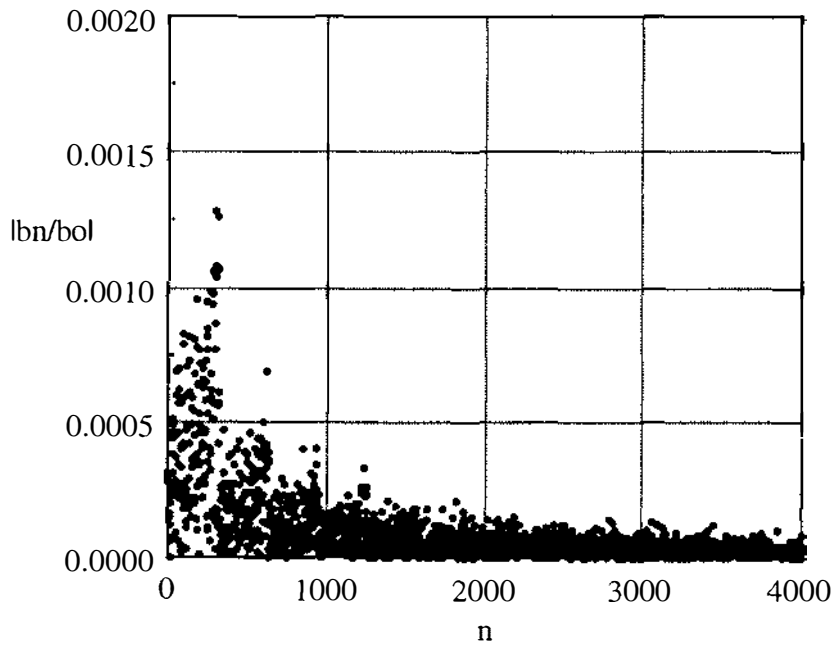

Figure 2.18: Odd Fourier series coefficients, normalised to the fundamental, for the 'worst case' stepped sinewave of amplitude $N = 50$ steps.

We note that the non-constant step rate produces non-zero harmonics from the fundamental upwards[3]. The spectrum does exhibit some pattern, however, with prominent peaks occurring at multiples of approximately 300, specifically, 307, 621, 935, 1243,.... This pattern is an artefact of the maximum step rate in each cycle. Consider the sinewave, $y = N.dsin\omega t$. The maximum slope is $\omega N.d$ and therefore the maximum step rate is ωN (Hz). As figure 2.17 suggests, this is a reasonable approximation to the step rate throughout the 'zero crossing' regions of the sinewave. We would then anticipate a prominence of peaks near $n = 2\pi N$ and multiples thereafter. For the particular case of $N = 50$, $2\pi N \approx 314$ which is consistent with the pattern observed above, and not surprisingly, a slight over-estimate.

We conclude that the amplitudes of higher harmonics, in the worst case, are less than 0.2% of the fundamental. This is a factor of 10 less than the inherent 'mechanical noise' level in the system from vibrations of the table, discreteness of the air jets, etc.

[3]cf. the Fourier spectrum of FM modulated signals.

An alternative method for driving the track is an analogue system with feedback. Because of the likelihood of small drift in such a system we decided in favour of the stepping motor for which the stability is intrinsically excellent.

2.3 Ultrasound Detection System

The ultrasound detection system measures, at a predetermined sampling rate, the distance between the tower and the button. This is achieved by the tower emitting a pulse of infrared light which triggers the button to emit an ultrasonic pulse (40kHz) in reply. The V-scope microprocessor measures the time delay between the outgoing and incoming signals and, multiplying this value with the velocity of sound in air, computes the tower-button distance. A temperature sensor in the base of the tower provides the V-scope microprocessor with the current ambient temperature. This information is used to allow for the air temperature variation of the speed of sound.

Through techniques such as phase comparison the manufacturer claims an accuracy of "a fraction of a millimetre". Specifically, the tower-button distance is measured and recorded to 0.1 mm. The system as we have employed it, does not produce precision this good due to noise interference from the air track. It would appear that the efflux from the track holes gives rise to sound waves with frequencies in the vicinity of 40kHz, thereby interfering with the measurement signals. Many steps were taken to minimise this effect including reducing the air flow rate through the track, altering the 'gain' of the tower and positioning cardboard 'baffles' so as to eliminate 'line of sight' between the tower and the track. Averaging techniques were also employed on the position data, bringing the noise level to within 5%. In spite of these measures, the accuracy could never be recovered to 'fractions of a millimetre' and occasionally the interference would produce 'spikes' in the position signal.

V-scope allows for two modes of operation. In its typical usage, PC2 acts as a sort of 'position oscilloscope', displaying in real time the glider position as relayed to it from the V-scope microprocessor. The software provided by V-scope allows control of various parameters such as the sample rate (10 ms, 20 ms etc.). This

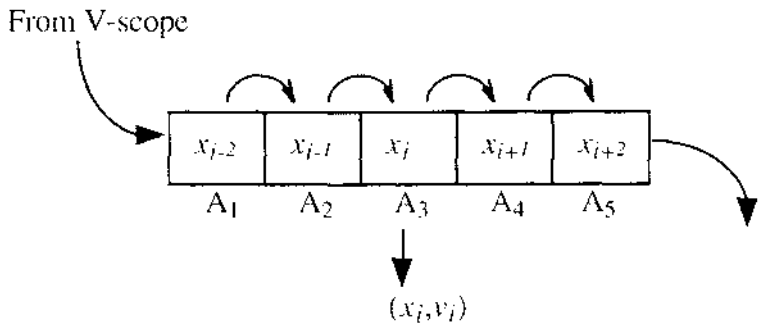

Figure 2.19: Data array for calculation of velocity.

software also differentiates the position-time data to produce plots of velocity and acceleration, all of which can be exported to ASCII data files.

V-scope also provides a 'direct communication protocol' which allows user-produced software to interact with the V-scope microprocessor, thus enabling custom designed experiments. This facility is used to produce Poincaré plots. Pre-existing, public domain RS-232 communications software was modified to enable control of the V-scope microprocessor from PC2, using the command set supplied with V-scope. Such commands include control of the communication Baud rate (typically 9600), the time between samples (typically 30 ms) and the start/stop signals. On receiving the command "@STARt;" from PC2, the V-scope microprocessor starts measuring the tower-button distance and sending it to PC2. The incoming 'location data records' (refer appendix A.1) consist of 10 bytes each, which include, among identification and checksum information, four bytes describing the position, x, of the glider. Concatenating these four bytes produces a number which is the tower-button distance in units of tenths of millimetres. This incoming stream of position information is fed into a five element array shown in figure 2.19. As each new position reading reaches PC2, the array elements are moved one place to the right, successively through each element of the array and then discarded. On each iteration, the velocity corresponding to the position value held in element 'three' is calculated. Due to the presence of noise and the exacerbating effect differentiation has on it, the formula used to calculate

the velocity is a four-point differentiator and smoother (Williams [35]):

$$v_i = \frac{2(x_{i+2} - x_{i-2}) + x_{i+1} - x_{i-1}}{10\delta t} \tag{2.40}$$

where δt is the time between samples.

In addition to the 'Location Data Records', the V-scope sends 'Input Data Records' (see appendix A.1) which contain data fed in to the V-scope microprocessor via its analogue and digital ports. The analogue port is connected to the potentiometer and gives the track slope information. The V-scope performs analogue to digital conversion of the voltage (range 0-5V) seen at this port and transmits the value as one byte. A value of 128 corresponds to the track being level.

Plotting each successive point (x_i, v_i) produces a phase plane curve in real time but, by using the track slope value, these points can be sampled at a chosen phase of the driving force thereby generating a Poincaré section. Sampling at the period of the driving term, one obtains the Poincaré section $P_\phi = \sum_n (x(t_n - \phi), \dot{x}(t_n - \phi))$ for $t_n = n2\pi/\omega$. In the particular case of the program *poincare* given in appendix B.1, the analogue level is (arbitrarily) set to 192 (negative slope) and thereby gives rise to the Poincaré section for $\phi = 60^\bullet$.

Chapter 3

Experimental Results

The apparatus described in chapter 2 was used to investigate the dynamics of the twin-well Duffing oscillator in general and to measure the chaos boundary in particular. The experiment was then extended (section 3.5) to include the boundaries of stability for a double well orbit .

3.1 System Parameters

The position dependent restoring force, $f(r)$, for the twin-well spring configuration was measured *in situ*. A force was applied to the glider by tilting the air track to a known slope. The new position at which the glider settles was measured with V-scope. The force *vs* position data is shown in figure 3.20 along with the least squares curve fit. Neglecting the small r^2 and constant terms, the fit, to third order is

$$f(r) = 2.54r - 45.66r^3 \tag{3.41}$$

This establishes the parameters α and β of equation 1.6. To measure the damping coefficient, γ, the rods were uncoupled from the glider and linear springs were attached to the glider, parallel to the track. The exponential decay of unforced oscillations of the resulting SHO enabled measurement of the logarithmic decrement and hence γ. The decay curve is shown in figure 3.21 together with the log plot of successive peak heights (normalised to the first). The slope of the least squares linear fit to the curve in figure 3.21(b) is -0.129 which is equal to $-\gamma/2m$.

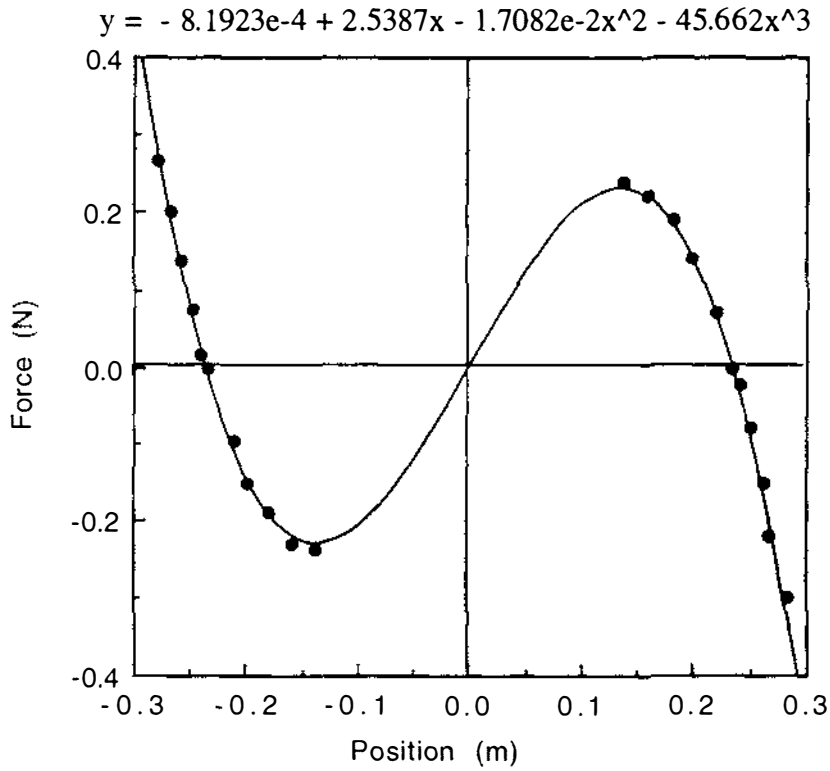

Figure 3.20: Measured restoring force $f(r)$ *vs* r with polynomial fit.

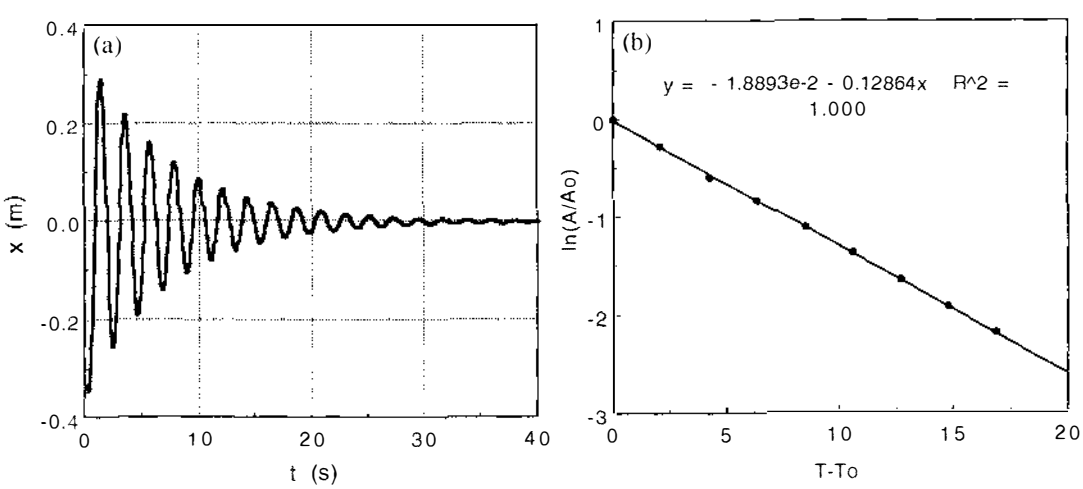

Figure 3.21: (a) Decay oscillation and (b) Log plot of the (normalised) amplitudes.

The mass of the glider is 0.352 kg and hence $\gamma = 0.091$. This technique does not take into account the friction of the rod-glider or rod-spring pivot points which we assume to be slight by comparison with the damping effect of the magnet (refer section 2.1). The measured parameters are summarised in table 3.3 together with their scaled[1] counterparts.

Table 3.3: Experimental system parameters.

α	2.54	a	7.21
β	45.66	-	-
γ	0.091	c	0.257
m	0.352 kg	-	1.00

3.2 'Typical' Behaviour

3.2.1 Unforced Oscillations

With the track level and stationary ($\Gamma = 0$), the glider is released from a non-equilibrium position and the resulting 'relaxation' oscillation is captured with V-scope (figure 3.22(a)). The glider settles in either well - depending on the initial conditions at release. Plotting the derivative of the position signal (velocity) versus position gives the phase space diagram (figure 3.22(b)). We note that the 'phase space' described in section 1.4 can adequately be described in the $(x, \dot{x})$-plane since the system is undriven. Figure 3.22(b) confirms the phase plane behaviour, particularly the action of the stable spiral, predicted in section 1.4.

3.2.2 Forced Oscillations

The apparatus permits observation of many of the solutions predicted numerically (see Ueda [29], Ueda *et al* [30]). For forced oscillations ($\Gamma \neq 0$), the phase space is 3-D, but the z-coordinate, ωt, increases linearly with time and for illustrative purposes, can be omitted. We must bear in mind however, that trajectories in the resulting phase plane may cross over each other at different times (or at least,

[1] Refer section 1.4.

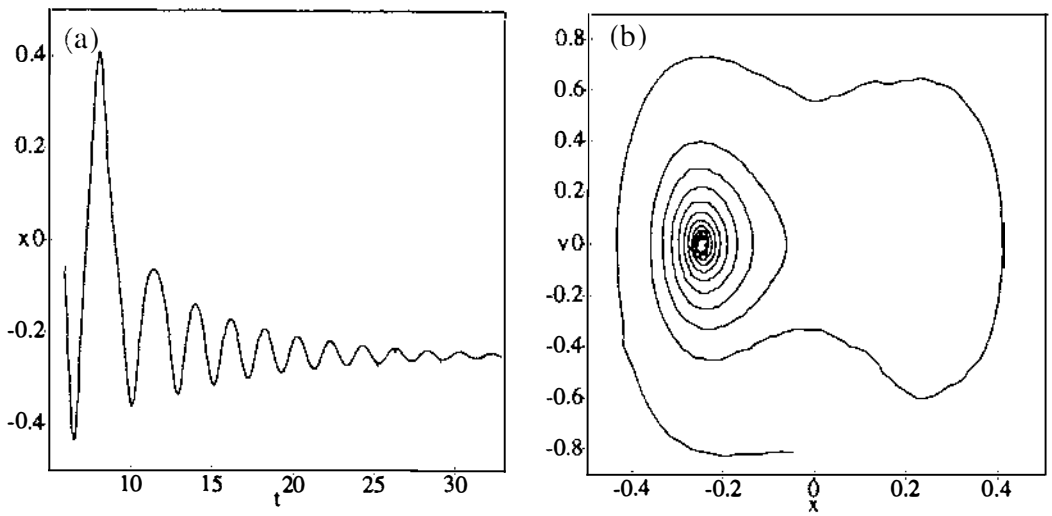

Figure 3.22: Relaxation oscillation ($\Gamma = 0$) (a) x *vs* t (b) v *vs* x.

different phases of the driving force). That is to say, the diagram is no longer a true 'state space' for the system.

Figure 3.23 shows the single-well (SW) orbit $x(t)$ and phase space. We note that in accordance with symmetry, if any particular SW orbit is stable, then it may exist in either well - a choice determined by initial conditions. Generally speaking, for our parameters, oscillatory behaviour in one well is dominated by this orbit[2].

We determine the frequency response of the SW orbit by keeping Γ fixed and varying ω. The 'amplitude' of the oscillation is measured, first as ω is slowly increased from a low value and then for decreasing ω. 'Amplitude' here means half of the x-range of the oscillation. The results are shown in figure 3.24. The hysteresis effect is evident and confirms that the SW response resembles that of a 'soft' spring. The position of the resonance curve on the ω axis agrees with the theoretical $\sqrt{2\alpha/m} = 3.80\ rad.s^{-1}$.

The SW behaviour does not die away entirely on both sides of the 'resonance peak'. For low frequencies at least, a slightly different single well orbit becomes stable and appears to undergo its own response - rising in 'amplitude' as ω decreases, but eventually losing stability. Figure 3.25 is one such orbit.

[2]Or a variation of it. See figure 3.25 for a low-frequency single-well oscillation.

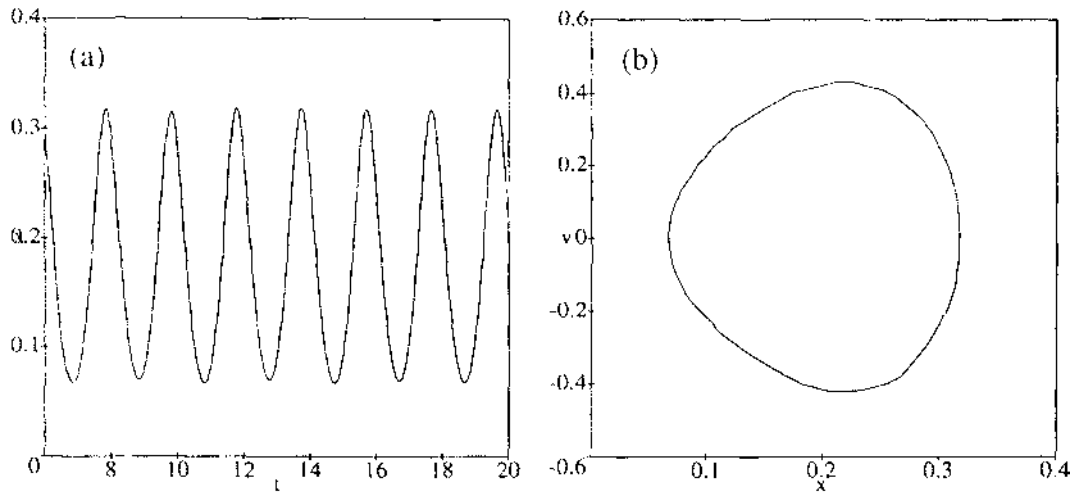

Figure 3.23: SW orbit for $\Gamma = 0.093$ N, $\omega = 3.19\ rad.s^{-1}$. (a) x *vs* t (b) v *vs* x.

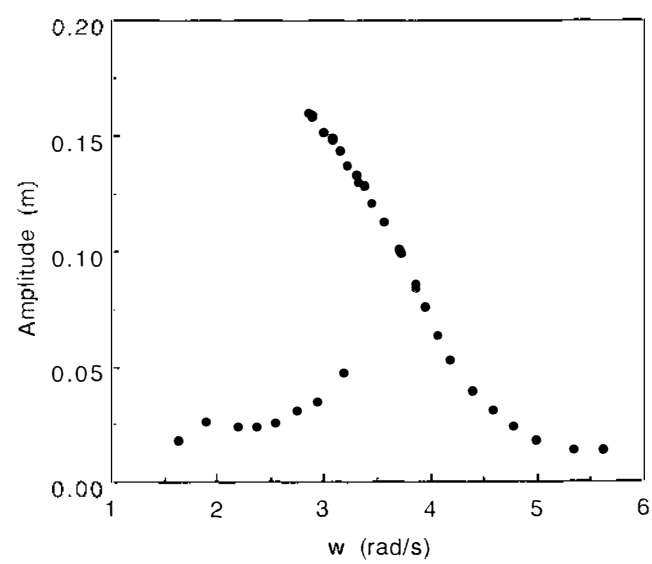

Figure 3.24: SW frequency response curve for $\Gamma = 0.06$ N.

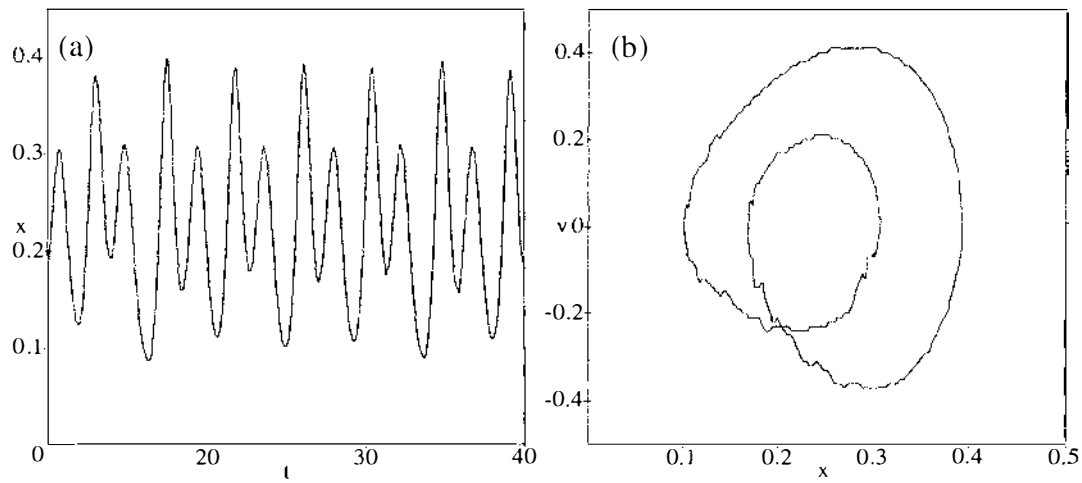

Figure 3.25: SW orbit at low frequency $\Gamma = 0.143$ N, $\omega = 1.44\ rad.s^{-1}$ (a) x *vs* t (b) v *vs* x.

For higher Γ ($\Gamma > 0.09$ N), the response of the SW orbit is similar to figure 3.24, but when the amplitude gets 'large', the glider 'escapes' from the well and the resulting double-well motion typically appears chaotic. From the low frequency side, as ω increases, this escape occurs when the vertical 'jump' point is reached. In making the sudden transition from low to high amplitude, the oscillation is no longer contained in the well. From the high frequency side, as ω decreases, the amplitude increases and is observed to suffer a period-doubling bifurcation. Figure 3.26 shows this transition as ω is decreased. Further decrease in ω results in double-well chaos. Figure 3.27 clearly shows the period-two oscillation and phase space where we note that the 'splitting' is most pronounced on one side of the orbit - that nearer the origin.

We can monitor the extent of the bifurcation by recording the two minimum x values as ω decreases. Figure 3.28 shows the experimental results from decreasing ω and measuring these two points. The splitting increases until around $\omega \approx 3.13\ rad.s^{-1}$ where the oscillation appeared to period double again, although this mode did not remain 'settled' for long enough periods to be conclusive. All of the bifurcated orbits exhibited fluctuations. It is difficult to distinguish between further bifurcation or some transient behaviour due to the adjustment of frequency or spurious vibrations in the apparatus. Below $\omega \approx 3.13\ rad.s^{-1}$ the oscillation simply

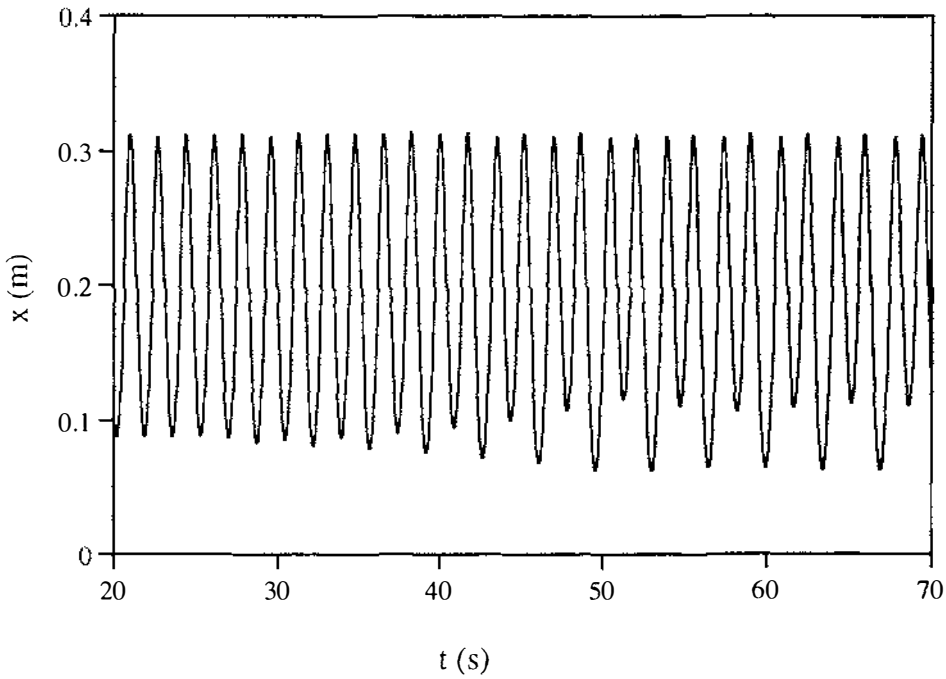

Figure 3.26: Bifurcation of SW orbit occurs as ω decreases; in this case a frequency change of $\Delta\omega = 0.06\ rad.s^{-1}$.

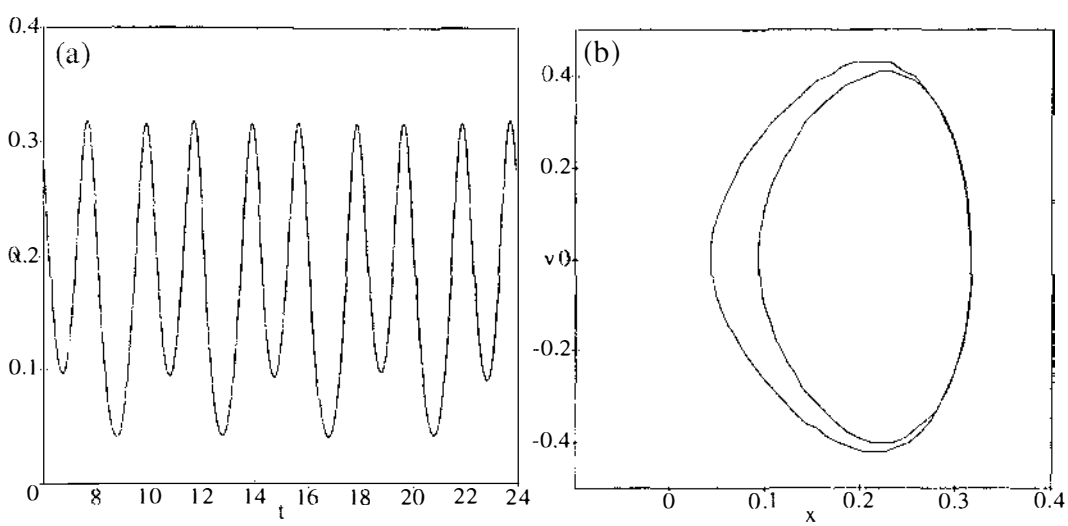

Figure 3.27: SW orbit after period doubling for $\Gamma = 0.093$ N, $\omega = 3.15\ rad.s^{-1}$ (a) x *vs* t (b) v *vs* x.

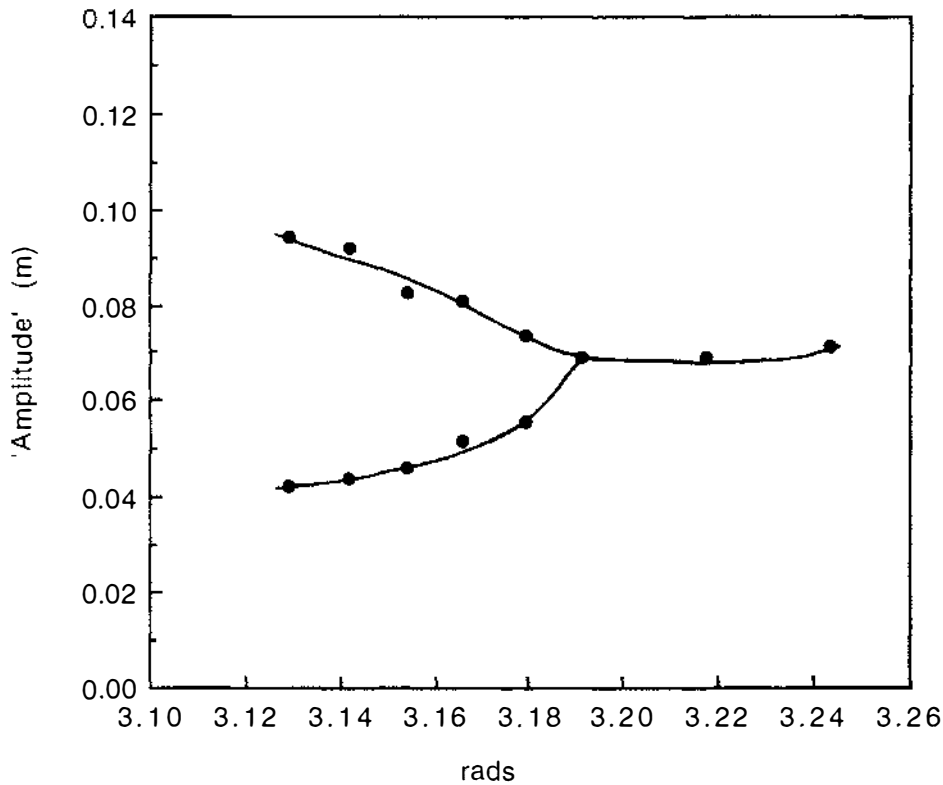

Figure 3.28: Bifurcation diagram for $\Gamma = 0.093$ N.

'spills over' into the other well and double-well chaos results. Finer observation of a bifurcation sequence (predicted numerically in De Souza-Machado *et al.* [6] and elsewhere) is beyond our present apparatus.

Figure 3.29 summarises the SW behaviour which leads to double-well chaos. From low frequencies, chaos occurs at the jump point (a). From high frequencies, a period doubling bifurcation (sequence) precedes chaos - point (b). This leaves a 'band of chaos' in the frequency sense, between the points (a) and (b). Figure 3.29 suggests that chaos will typically occur at frequencies less than ω_0. We conclude that escape from a well leading to chaos is not purely an 'amplitude effect'; that is, in both cases the onset of chaos occurs at different amplitudes and via distinct routes.

Figure 3.30 shows a typical time history of a chaotic oscillation and the corresponding phase plane trajectory. The phase plane appears to 'fill up' as time passes. As described in section 2.3, a Poincaré section is obtained by sampling such data at the frequency of the driving force. Figure 3.31 shows the result of

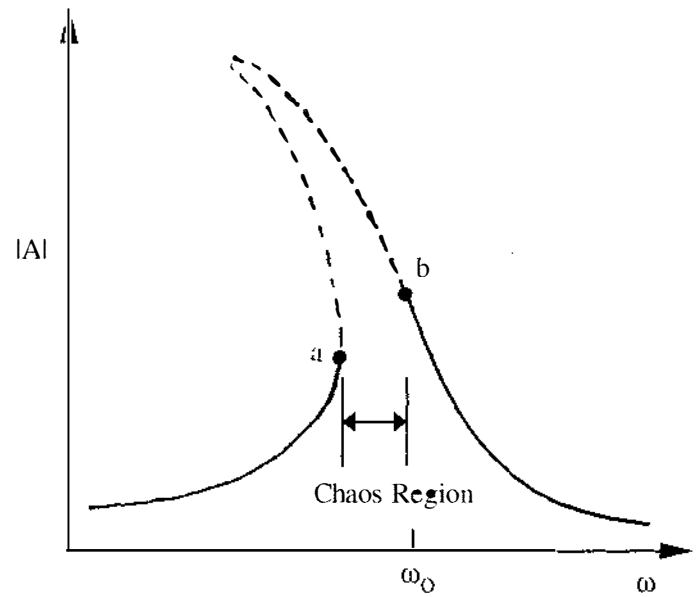

Figure 3.29: Sketch of the SW response for Γ large.

plotting only the points which coincide with a driving force phase angle of 120 degrees. Such a reduction of information reveals the chaotic strange attractor and its underlying structure. Variation of the sampling phase through 360 degrees is shown in figure 3.32. Each Poincaré section in figure 3.32 contains approximately 5000 points sampled (real time) from 4 hours of chaotic trajectory.

The preceding discussion has implied that escape from a well, achieved by either increasing or decreasing ω, results in double-well chaotic motion. This is not always the case. Depending on initial conditions at escape (and Γ, ω), a double-well periodic orbit (see figure 3.33), hereafter abbreviated to 'DW orbit', can also be observed. Furthermore, this orbit was found to co-exist with double-well chaotic motion. This is possible, as the orbit and the strange attractor occupy different regions of phase space. Initial conditions determine which motion prevails. Thus, in suffering a perturbation, the system may make a transition from one mode of oscillation to the other. This coexistence, predicted numerically (Guckenheimer and Holmes [11]), is demonstrated in figure 3.34 where, with no change in parameters, a chaotic oscillation is disturbed (by human intervention) and 'locks on' to the stable DW orbit. The reverse effect is also possible. Once in the DW orbit mode, the system does not necessarily revert back to the SW orbit

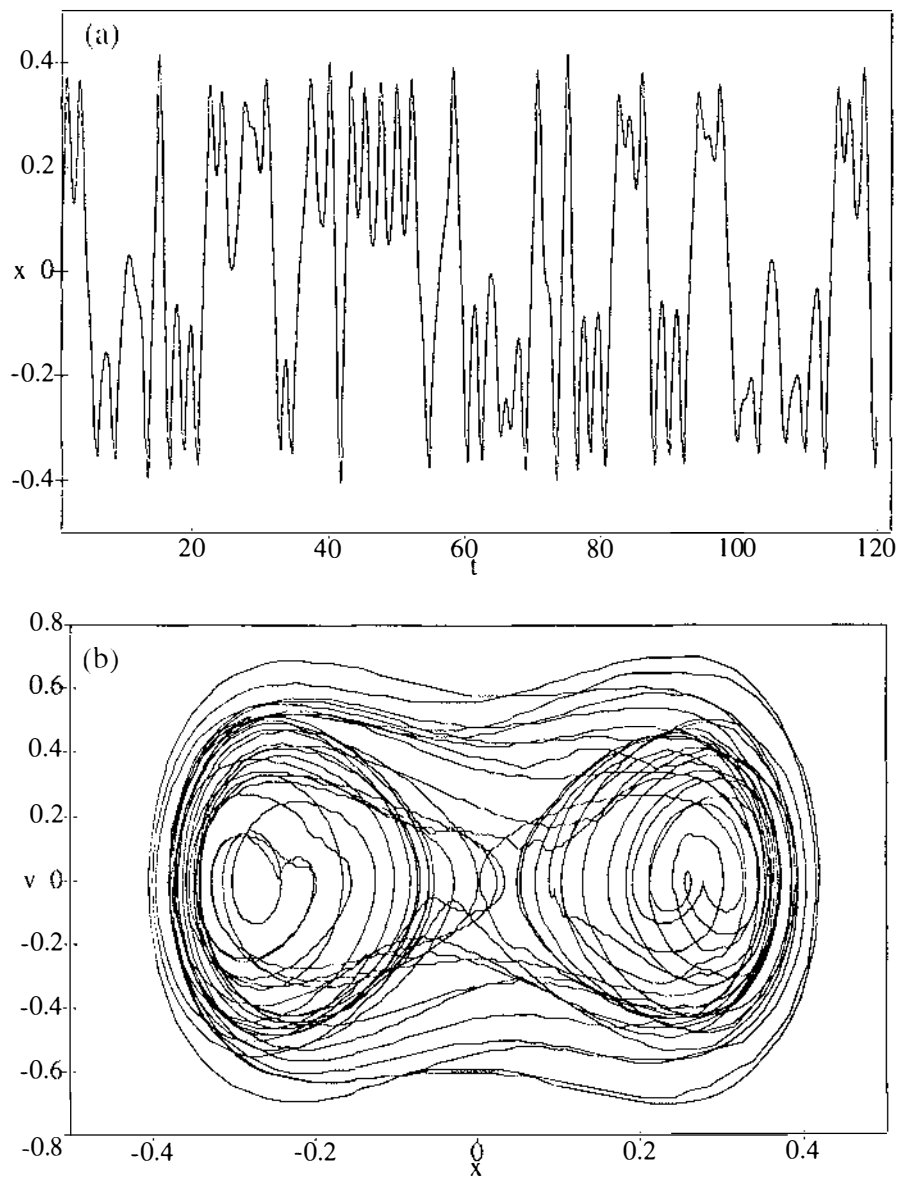

Figure 3.30: 122 s of chaos for $\Gamma = 0.143$ N, $\omega = 2.92\ rad.s^{-1}$. (a) x *vs* t (b) v *vs* x.

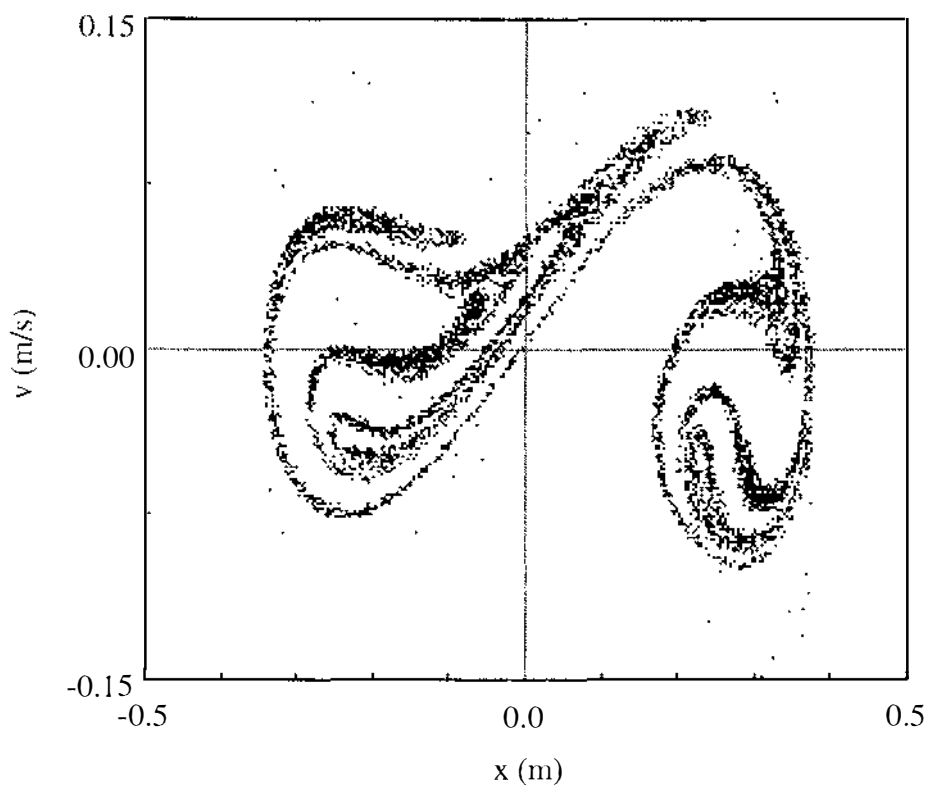

Figure 3.31: Poincaré section for $\phi = 120°$.

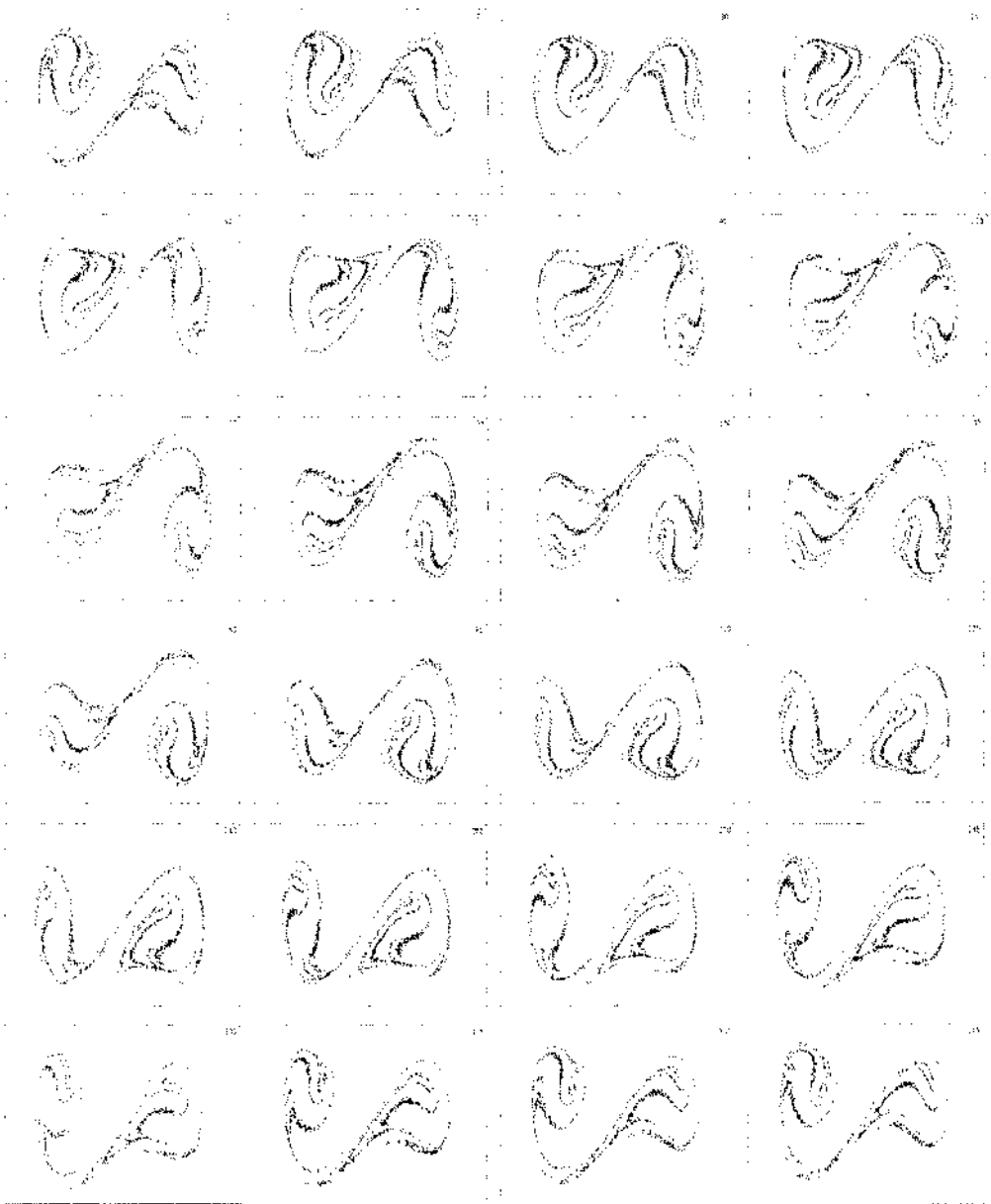

Figure 3.32: Experimentally obtained Poincaré sections, P_ϕ, with the drive phase angle given in degrees.

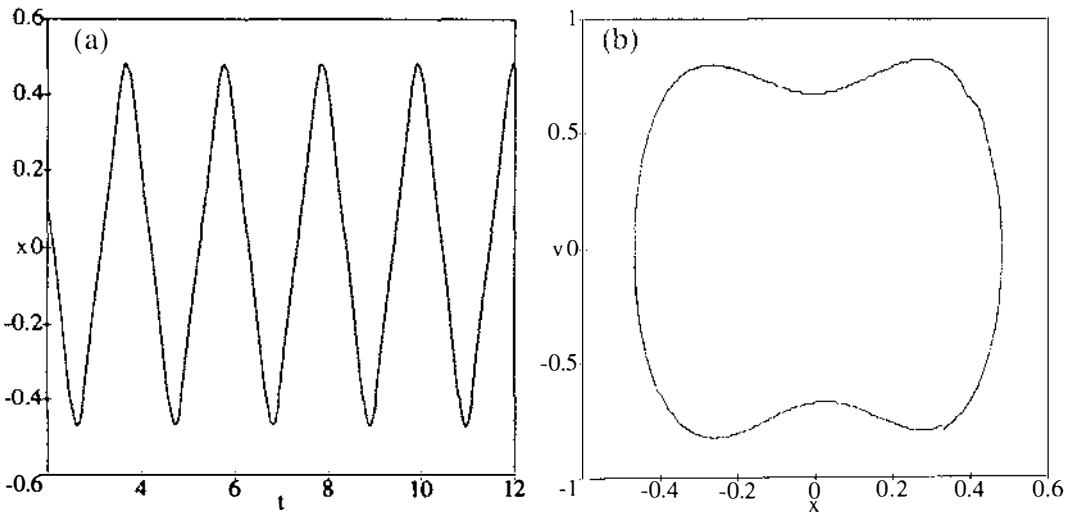

Figure 3.33: DW orbit for $\Gamma = 0.143$ N, $\omega = 3.13\ rad.s^{-1}$. (a) x *vs* t (b) v *vs* x.

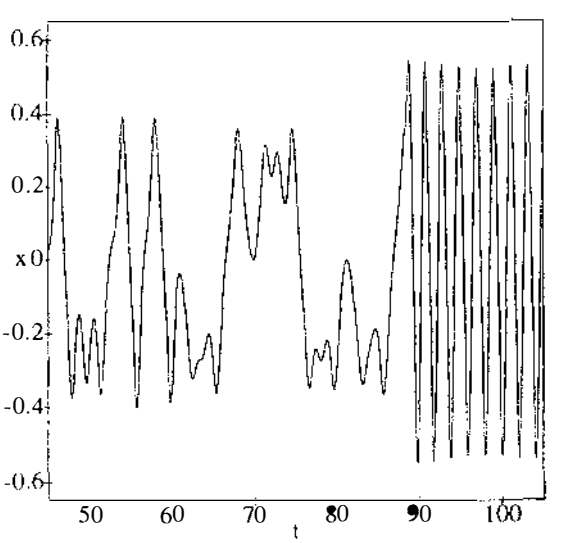

Figure 3.34: $\Gamma = 0.152$ N, $\omega = 3.14\ rad.s^{-1}$ (a) x *vs* t (b) v *vs* t. (opposite)

v
1
0
-1
t
50
60
70
80
90
100

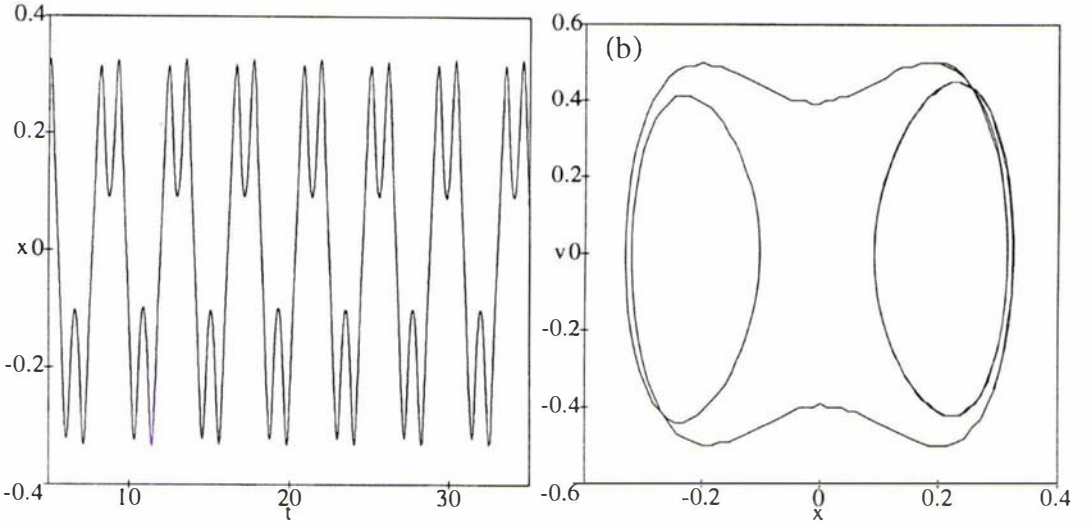

Figure 3.35: DW orbit at low frequency: $\Gamma = 0.152$ N, $\omega = 1.51\ rad.s^{-1}$ (a) x *vs* t (b) v *vs* x.

at the same frequency (Γ constant) at which escape occurred. Thus, hysteresis separates the two modes - similar to the 'hard' spring (figure 1.6). This highlights an important qualitative characteristic of the twin well oscillator: The response of local, SW orbits is similar to a 'soft' spring whereas the response of large DW orbits is like that of a 'hard' spring.

The DW orbit loses stability as ω is increased and reverts to the SW-orbit (symmetry breaking) or chaos. Similar effects are observed by Olson and Olsson [22] for the ($\alpha < 0$, $\beta > 0$) case.

3.3 Experimental Lyapunov Exponents

In the experimental context, observation of chaos (or periodicity) is largely a visual process. An orbit is deemed 'periodic' simply because the $x(t)$ *vs* t plot appears to repeat; similarly, if the trajectory appears random (and gives rise to a Poincaré section like those of figure 3.32) over long time periods, we assume chaos. This does not hamper our detection of the onset of chaos, since this is marked by 'escape' from a well, but it is less than rigorous. Indeed, Guckenheimer and Holmes [11] cast doubt on the authenticity of the 'strange attractor' observed in section 3.1, leaving open the possibility that it may be "an artefact of the noise and is absent in the ideal deterministic system". We cannot settle such a subtle issue through experiment, but we can estimate the largest Lyapunov exponent and through this, obtain strong justification for identifying chaotic behaviour.

The standard (Liapunov) definition of stability states that a solution, $x(t)$, is asymptotically stable if all other solutions within a neighbourhood tend to it as time tends to infinity. A chaotic solution on the other hand, may be thought of as a 'completely unstable' solution, that is, neighbouring solutions diverge with time and, moreover, they do so exponentially. These exponential rates of separation are characterised by the Lyapunov exponents where a positive exponent indicates chaos.

The properties of Lyapunov exponents, which characterise the orthogonal, local flow rate of points in phase space, are well established ([36], [3], [9], [10]). Wolf *et al* [36] define the ith one-dimensional Lyapunov exponent for a continuos dynamical system in n-dimensional phase space as

$$\lambda_i = \lim_{t\to\infty} \frac{1}{t} log_2 \frac{p_i(t)}{p_i(0)} \tag{3.42}$$

where $p_i(t)$ is the length of an ellipsoidal principle axis, evolved from an infinitesimal n-sphere of initial conditions. (refer figure 3.36). For the driven Duffing system in particular, $n = 3$, giving rise to three Lyapunov exponents, λ_i, one of which is 0 ([36], [11], [6]) as it corresponds to the variable $z = \omega t$, which increases linearly with time. It therefore makes no contribution to the rate of separation

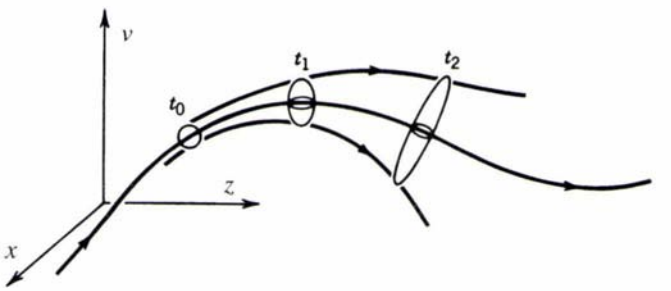

Figure 3.36: Evolution of trajectories from a small sphere of initial points.

between trajectories. The possibilities for the other two are (+, -) and (-, -) corresponding to a strange attractor and a limit cycle respectively. Due to the fact that, with the passage of time, all initial condition vectors tend to be pulled into the direction of maximum growth rate, algorithms for the computation of the λ_i typically involve repeated Gram-Schmidt renormalisation (GSR). (This involves repeatedly establishing the direction of maximum growth rate and setting up new initial condition vectors orthogonal to it.). This property of vector direction changing means that the two exponents do not have a one-to-one correspondence with the phase space variables.

The above process lends itself to a numerical analysis where any number of trajectories neighbouring the reference trajectory (fiducial) can be generated. Experimentally, it is impractical to record hours of phase space trajectory (sampled at 30 ms) with a view to monitoring the evolution of neighbouring initial conditions. The closest we come to this, however, is the thousands of phase space points which make up the Poincaré sections of figure 3.32. Furthermore, these points are stored in chronological order in the data file and, as such, are discrete recordings of the state of the system, separated in time by the period of the driving force.

Wolf *et al.* [36] proposes an estimation method for the largest exponent from experimental data with such a 'fixed evolution time' as do Kantz [15], Abarbanel *et al.* [1] and Briggs [5]. Any such algorithm must however, be sufficiently discriminatory to cope, for example, with the outliers visible in the Poincaré section of figure 3.31, that is, noise to the extent of 'spikes' in the data. The algorithm we employ is most similar to [36]. To bring the rather general definition of equation

3.42 into the particular case of the Duffing twin well, we proceed as in [15] and define the largest Lyapunov exponent in terms of the phase space position $\mathbf{X}(t)$ where $\mathbf{X}(t)$ is the vector (x, v, z) as described in section 1.4.

$$\lambda_{max} = \lim_{t\to\infty} \lim_{\epsilon\to 0} \frac{1}{t} ln \left(\frac{|\mathbf{X}(t) - \mathbf{X}_\epsilon(t)|}{\epsilon} \right) \tag{3.43}$$

where $|\mathbf{X}(0) - \mathbf{X}_\epsilon(0)| = \epsilon$. That is, it doesn't matter what direction we choose the initial separation vector to be in, as the dominating effect of the positive exponent will always ensure '$exp(\lambda_{max}t)$' growth after sufficient time ($t \to \infty$). This assumes that the local behaviour in phase space is purely 'stretching' (or 'shrinking') and that no 'folding' has occurred - an assumption which is justified by choosing the initial points to be arbitrarily close, a condition secured by the $\epsilon \to \infty$ limit of equation 3.43. Experimentally, neither limit can be achieved due to only a finite amount of data being available and the presence of noise.

Our Poincaré section data files have the form:

$$P_\phi = \{\ldots \mathbf{X}_{i-1}, \mathbf{X}_i, \mathbf{X}_{i+1}, \ldots\} \tag{3.44}$$

We start with the first point in the file, $\mathbf{X}_1$, and scan through the rest for a neighbouring point, within a certain distance ϵ (in the Euclidean sense), but not too close, as the percentage error in the separation of close points will be highest. Possible candidates lie therefore, on an annulus about $\mathbf{X}_1$ defined by $\epsilon_0 < d_{1,j} < \epsilon$ where $d_{1,j} = |\mathbf{X}_1 - \mathbf{X}_j|$. Having found a suitable neighbouring point, the time-evolved separation is found by using the points which lie immediately after $\mathbf{X}_1$ and $\mathbf{X}_j$, specifically, $d_{2,j+1} = |\mathbf{X}_2 - \mathbf{X}_{j+1}|$. The growth rate, λ, between the initial conditions $\mathbf{X}_1$, $\mathbf{X}_j$, over the time $\tau = 2\pi/\omega$, is then given by

$$\lambda = \frac{1}{\tau} ln \frac{d_{2,j+1}}{d_{1,j}} \tag{3.45}$$

A replacement separation vector is now sought by looking at points which lie on the annulus about $\mathbf{X}_2$ but in a direction similar to the current separation vector $\mathbf{X}_2 - \mathbf{X}_{j+1}$. Thus, two criteria must now be satisfied - proximity and direction.

The process repeats until the end of the data file is reached with the average λ being taken as the estimate of the largest Lyapunov exponent. The directional requirement ensures that the separation vector 'tracks' maximum growth. If a suitable separation vector cannot be found then the pair $(\mathbf{X}_{i+1}, \mathbf{X}_{j+1})$ are allowed to evolve to their successive points where the new separation direction, but not λ, is calculated.

The program *lyapunov* (appendix B.5) implements this algorithm. We compare the results of *lyapunov* and CDW in estimating the maximum Lyapunov exponent, λ_{max}, by running *lyapunov* with Poincaré section data generated numerically by CDW. The results are shown in table 3.4 together with the CDW generated exponents using conventional GSR techniques.

Table 3.4: Comparison of algorithms to estimate λ_{max}. In each case, $m = 1$.

α	β	γ	Γ	ω	λ_{max} (CDW)	λ_{max} (*lyapunov*)
1	1	0.5	0.42	1	1.01	1.19
8	100	1	0.66	3	1.20	1.39
4	40	0.70	0.82	2.50	0.86	0.81
7.21	129.73	0.24	0.48	3.28	1.18	1.20

Here the exponents are stated in units of 'bits/drive period' - determined by using logs to the base 2 and $\tau = 1$ in equation 3.45 above. Thus an exponent of 1 bits/drive period indicates that, on average, two points initially close together will be at twice this separation after one drive period. Table 3.4 shows reasonable agreement between the two methods and so we now run *lyapunov* using the experimental Poincaré section data from $\phi = 135°$ of figure 3.32, giving $\lambda_{max} = 1.17$ bits/drive period. Running CDW with the same parameter values (3, 84, 0.284, 0.183, 2.14) gives $\lambda_{max} = 1.13$ bits/drive period. We conclude, therefore, that the algorithm *lyapunov* provides satisfactory estimation of λ_{max} for the experimental data where the use of conventional techniques are not possible.

Here *lyapunov* has been applied to the data retrospectively; however the possibility of a 'hybrid' between this algorithm and *poincare* providing 'real time' estimation of λ_{max} is feasible. Such an algorithm, however, would offer only slight advantages as the statistical nature of exponent estimation typically requires the passage of several thousand drive periods before the λ_{max} value stabilises.

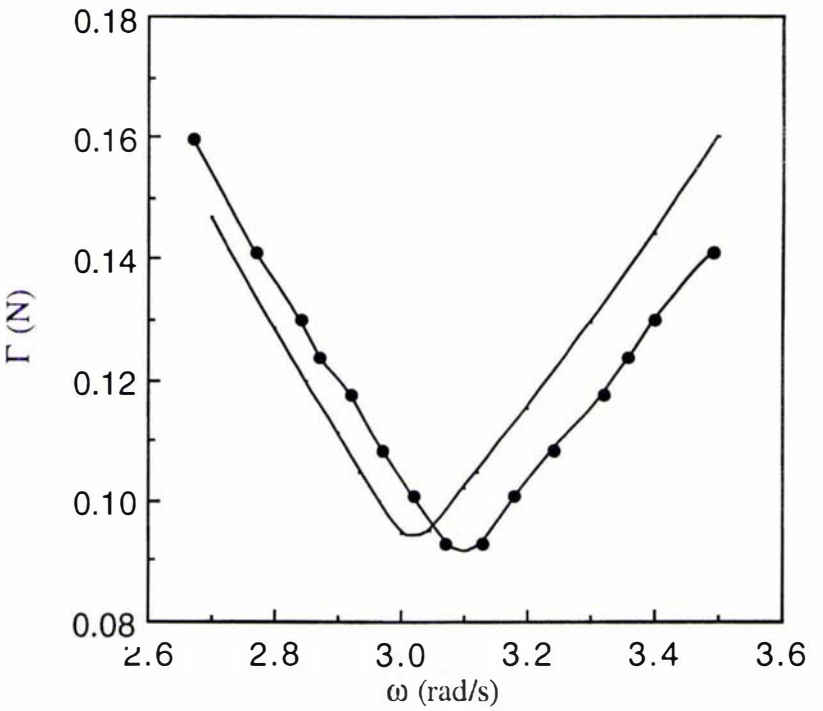

Figure 3.37: Boundary in the (ω, Γ)-plane between chaotic and SW-orbit periodic motion. Experimental data (connected dots); Numerical data (plain line).

3.4 SW orbit - Chaos Boundary

As hysteresis is not a characteristic of the SW orbit - chaos transition, we can fix one of the parameters, in practice, Γ, and vary ω. The boundary in the (ω, Γ)-plane, is defined by the points (a) and (b) in figure 3.29. Having chosen a driving force amplitude, and, with the system in the SW orbit, the frequency is slowly increased until escape occurs. A similar process is performed for ω decreasing, thereby measuring the two frequencies, ω_a and ω_b, of escape. Figure 3.37 is a plot of these experimental points for various Γ together with a numerically generated[3] boundary for comparison. Parameter values in the region above the line give rise to chaotic oscillations; those below, SW orbits. The system has a well defined minimum Γ below which no chaos is observed for any frequency (approximately $\Gamma = 0.09$ N.). This minimum occurs, as anticipated, at a frequency lower than the small amplitude natural frequency of oscillation in either well ($\omega_0 = 3.80\ rad.s^{-1}$ for our parameters). The 'sides' of the boundary appear almost linear. Least-squares linear regression on each side gives slopes of -0.166 and $0.133\ N.rad^{-1}.s$

[3]Points found numerically using CDW [26].

for the experimental data and -0.174 and 0.143 $N.rad^{-1}.s$ for the numerical data.

While the level of agreement between the experimental and numerical data is less than perfect, we can observe strong similarity in terms of general shape and line slope. The experimental data deviates from the numerical by a frequency shift of approximately 0.08 $rad.s^{-1}$. A smaller difference in Γ terms of approximately 0.003 N is also evident. The latter difference could be accounted for by uncertainty in the mass value. The value of $m = 0.352$ kg does not take into account the mass of the connecting rods. While the rod mass was minimised, any effect they do have will be one of slightly increasing the effective mass of the glider. This slight underestimate of m leads (refer equation 2.31) to an underestimate of Γ (by no more than 3%, however). The frequency shift is less easily understood, but is most likely due to inaccuracies in the parameters α and β. It is difficult to predict how their variation would affect the boundary, but we can make an estimate based on the dependence[4] of ω_0 on α, specifically, $\omega_0 \approx \sqrt{2\alpha/m}$. We take this as a measure of the overall 'position' of the response curve. For the present parameters, we obtain $\omega_0 = 3.80$ $rad.s^{-1}$. Shifting this to 3.88 $rad.s^{-1}$ gives rise to $\alpha = 2.64$. Thus a 4% difference in α may cause the observed deviation. Other sources of error include the possibility of the force function being better described by the inclusion of fifth order or other such higher powers in the polynomial fit.

Similarity between the boundary line above and that of Moon [19] (refer figure 4.45) is slight indeed. Furthermore, fractal properties of the boundary, reported in [19] are not seen here experimentally, or numerically.

3.5 DW orbit Behaviour

If Γ is large enough, the DW orbit may become stable, and, depending on ω, may coexist with both chaos and the SW orbit. Because there is a hysteresis effect between the DW orbit and these modes, the description of parameter regions of stability comprises two lines. One of these lines (upper) indicates forces above

[4] An increase in m clearly has the effect of slightly decreasing ω_0 also.

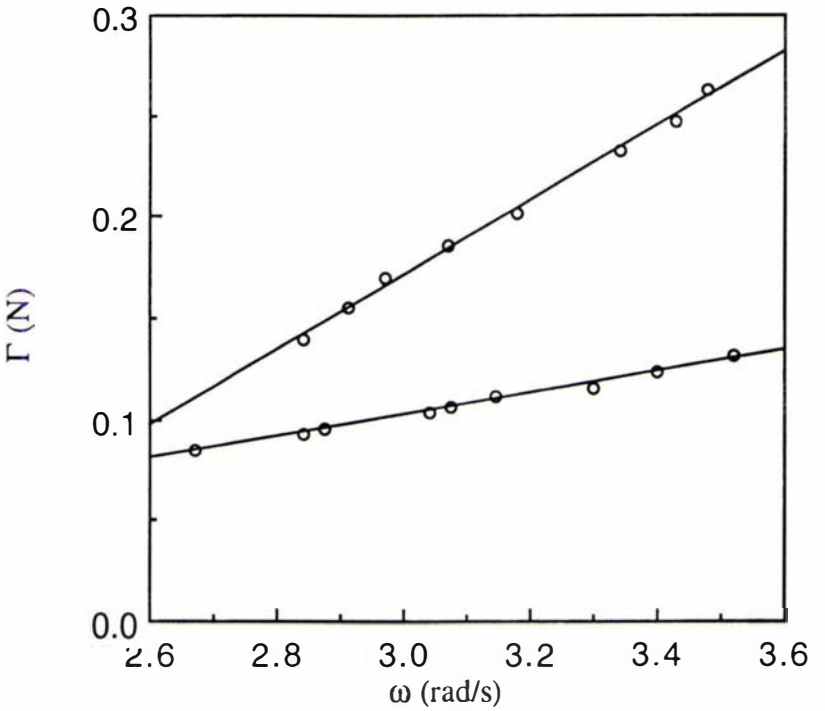

Figure 3.38: Experimental boundaries in the (ω, Γ)-plane for the stability of the DW orbit (lower) and transition to the DW orbit from chaos (upper).

which, *only* the DW orbit is stable and corresponds to a chaos-to-DW orbit transition. The other indicates the lower limit of DW orbit stability. The area in between is a coexistence region.

The experimental results are shown in figure 3.38. The data is obtained as in section 3.4, by choosing a Γ value and varying ω 'on the run'. With the system in the DW mode, ω is increased until the mode loses stability - reverting to chaos or the SW orbit. This defines the lower line in the (ω, Γ)-plane. The upper line is found by reducing ω while the system is in the chaotic mode - at a particular frequency chaos ceases and the DW orbit dominates. The data shown are accompanied by linear least squares fits.

Numerically obtained versions of these lines reveal a frequency shift similar to that observed in section 3.4.

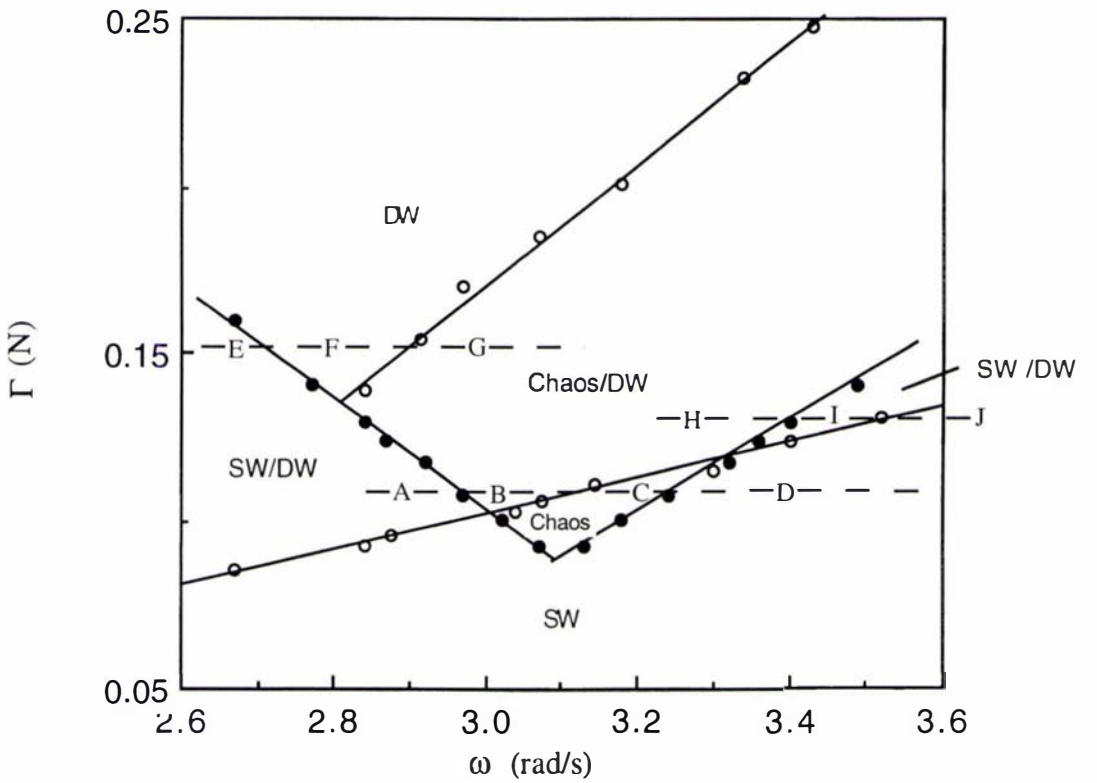

Figure 3.39: Plot of all experimental boundaries in the (ω, Γ)-plane.

3.6 Summary

All three experimentally obtained boundaries are shown in figure 3.39. Labels indicate what motions are possible in each region. No suggestion is made that these boundaries are in fact, straight lines, yet they display sufficient linearity over the parameter ranges of interest for us to depict them as such. We note that the region which gives rise only to chaos is very small - approximately triangular and barely 0.3 $rad.s^{-1}$ wide and 0.02 N high. Chaos more often, coexists with the DW orbit at higher Γ, where such phenomena as that depicted in figure 3.34 are possible.

To illustrate the transitions between modes, we move along each of the three broken horizontal lines in figure 3.39 (as was done experimentally). Thus, starting at A, consider ω increased, taking the system through B and C to D. At A two possibilities exist: an SW or a DW orbit. If originally in an SW orbit, on crossing the boundary into B, the orbit can become chaotic or DW. If chaotic, it stays chaotic going to C and crossing into D, it becomes SW again. But if it becomes

DW at B, it will become chaotic in C and change to SW at D.

Moving in the reverse direction, the SW orbit at D becomes chaotic at C and remains so, becoming SW or DW at A.

On the other hand if were DW at the outset, then at B it remains DW, going chaotic at C and SW at D.

Moving to the second line, we consider an SW orbit at E. At F it is DW and remains so moving to G. Reversing direction from G, the DW orbit will remain so through F and E. But chaotic behaviour at G will become DW at F and remain in DW at E.

Finally consider the H-I-J line. Chaos at H becomes SW or DW at I and SW at J. In the reverse direction, SW stays SW at I and becomes chaotic or DW at H. On the other hand, a DW orbit at H stays DW at I and changes to SW going to J.

Where two outcomes are possible, which is established depends on the state of the system at the time of frequency change, that is, initial conditions. Thus whenever 'or' has been used in the previous paragraphs, initial conditions determine the outcome. In general, the DW orbit is favoured at higher Γ and the SW at lower Γ.

Hysteresis then, characterises transitions between SW and DW orbits and DW and chaos, but *not* SW orbits and chaos. While we must regard the numerical results as the definitive description, we conclude that the experimental results achieve very good precision - if not accuracy - in reproducing the predicted behaviour of the oscillator.

Figure 3.40 is an enlarged section of figure 0.2 reproduced from Janicki and Szemplińska-Stupnicka [14] in the area of parameter space which we cover experimentally. Lines to compare (qualitatively) with the experimental data (figure 3.39) have been highlighted. [14] uses the parameter values $\alpha = \beta = 0.5$, $\gamma = 0.1$ ($m = 1$). The '3T' and '5T' subharmonics reported in [14] were not seen here experimentally.

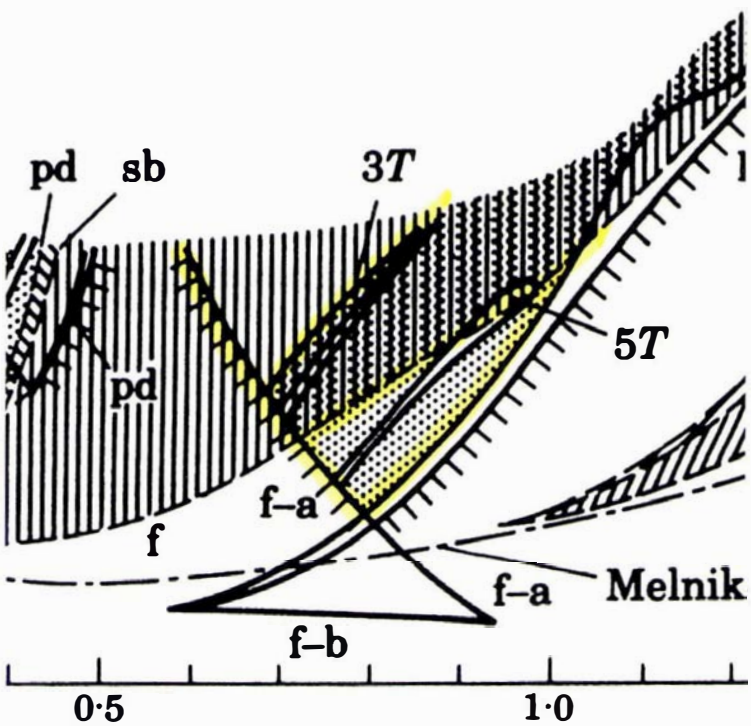

Figure 3.40: Detail reproduced from figure 4, Janicki and Szemplińska-Stupnicka [14].

Chapter 4

Modelling the Chaos Boundary

The aim is to develop a fully analytic model for the chaos boundary. Strictly speaking, the main boundary of interest, the 'V-shape' of figure 3.39, is the boundary for escape from one well as, (for certain parameter values) the system can pass from the SW orbit to the DW orbit directly. More specifically then, we seek the (ω, F)-plane boundary of stability for the SW orbit, part of which is also the boundary for chaos. Modelling single-well behaviour is therefore essential in predicting the onset of chaos.

Duffing's equation (4.46) has no general solution. The widely reported method employed by Duffing (see Duffing [8], Stoker [28], Hayashi [12]) - a variation of which is seen in section 1.4 - is iterative in nature and essentially requires 'a' to be small in order to secure convergence. Janicki and Szemplińska-Stupnicka [14] employ a perturbation method, namely the KBM[1] technique, to obtain the amplitudes of harmonic solutions. Such techniques typically involve transforming the equation to a near linear form with nonlinear terms being scaled as μ, a small parameter. For our parameters however, the strength of the nonlinearity is such that the nonlinear terms cannot be treated as perturbations to a linear equation. Moreover, [14] models a different chaos boundary to the one we investigate (specifically, referring to figure 0.2, the chaos boundary located near $\nu = 1.8$, $F = 0.35$) and makes use of numerical methods in the stability analysis of the solutions,

[1] Krylov-Bogoliubov-Mitropolsky perturbative method of solution as described in Nayfeh [21] for example.

which [14] reports, provides a "rough estimation of the line".

Kapitaniak [16] uses the domains of existence of period doubling cascades as boundaries for chaos, but, again, uses numerical procedures to solve the resulting algebraic equations.

In constructing a fully analytic model, we employ (section 4.1) a harmonic balance method to obtain solutions to Duffing's equation, but make use of perturbative techniques in analysing their stability (section 4.3). In sections 4.2.1-4.2.2 we outline several analytic methods for predicting the boundary, in particular the use of 'threshold' conditions for escape.

4.1 Modelling the Single Well orbit

We restate Duffing's equation (1.18) in its scaled form (refer section 1.4).

$$\ddot{x} + c\dot{x} - ax(1 - x^2) = Fcos\omega t \tag{4.46}$$

where (from table 3.3) $a = 7.21$ and $c = 0.257$.

That the SW orbit consists primarily of first and second harmonics can be demonstrated in several ways. A Fourier representation[2] (figure 4.41(b)) of the $x(t)$ time history of a numerically generated SW orbit justifies a two frequency solution. The amplitude of higher harmonics (≥ 3) are less that 3% of the fundamental. The SW orbit is therefore assumed to be well described by the following:

$$x(t) = E + Acos(\omega t) + Bsin(\omega t) + Ccos(2\omega t) + Dsin(2\omega t) \tag{4.47}$$

In what follows we regard upper case symbols as variables whereas lower case symbols, except t, are parameters of the system.

The coefficients of the '2ω' frequency terms, while included in the solution, are considered small and therefore, in what follows, terms containing powers or products of C or D are neglected. We also note that the *sine* terms in equation

[2]Fourier coefficients evaluated using program FT - appendix B.3.

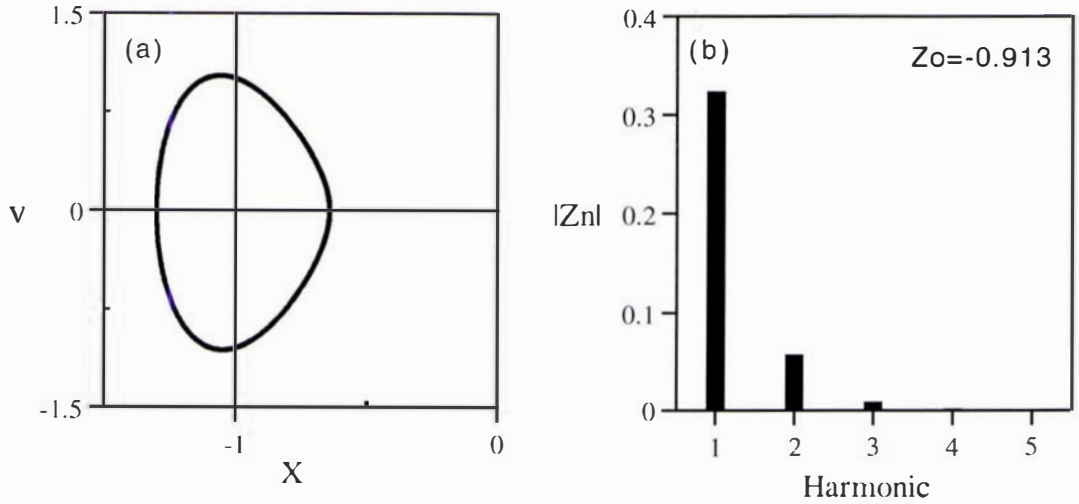

Figure 4.41: (a) SW orbit for $\omega = 2.78\ rad.s^{-1}$, $F = 1.57$. and (b) Harmonic components of $x(t)$.

4.47 are necessary due to damping in the system. If $c = 0$ these terms vanish and the solution 4.47 is either completely in-phase with the $Fcos(\omega t)$ drive term (A, $C > 0$), or π radians out of phase (A, $C < 0$).

The harmonic balance technique proceeds by substituting into equation 4.46 the assumed solution (4.47), with unknown coefficients, and expanding. We note that as $x(t)$ comprises 5 terms, the cubic term in equation 1.18, on expansion, generates 125 terms alone, making for 139 in all (see appendix C.1 for greater detail). This number of terms is greatly reduced by neglecting harmonics of order ≥ 3 in addition to the approximations mentioned above.

By equating coefficients of each harmonic to zero, we obtain five equations:

$$E(E^2 + \frac{3}{2}Z^2 - 1) + \frac{3}{4}aC(A^2 - B^2) = 0 \qquad (4.48)$$

$$A(\frac{3}{4}aZ^2 + 3aE^2 - a - \omega^2) + 3aE(AC + BD) + cB\omega - F = 0 \qquad (4.49)$$

$$B(\frac{3}{4}aZ^2 + 3aE^2 - a - \omega^2) + 3aE(AD - BC) - cA\omega = 0 \qquad (4.50)$$

$$C(\frac{3}{2}aZ^2 + 3aE^2 - a - 4\omega^2) + \frac{3}{2}aE(A^2 - B^2) + 2\omega Dc = 0 \qquad (4.51)$$

$$D(\frac{3}{2}aZ^2 + 3aE^2 - a - 4\omega^2) + 3aEAB - 2\omega Cc = 0 \qquad (4.52)$$

where $(A^2 + B^2)$ has been replaced by Z^2, Z therefore being the amplitude of fundamental harmonic of the oscillation.

Of the two terms in equation 4.48, $\frac{3}{4}aC(A^2 - B^2)$ is clearly much smaller than the other and we neglect it, enabling solution for E, the 'midpoint' of the oscillation:

$$E = 0, \pm\sqrt{1 - \frac{3}{2}Z^2} \tag{4.53}$$

For $Z^2 = 0$ equation 4.53 produces the three equilibria expected (0, $\pm$1). For $Z^2 \neq 0$ we note that $|E|$ decreases as Z^2 increases, approaching 0 as Z^2 approaches $\frac{2}{3}$.

Neglecting the terms $2\omega Dc$ and $-2\omega Cc$ from equations 4.51 and 4.52 respectively and eliminating all but Z from equations 4.49 - 4.53, we obtain:

$$Z^2\left\{c^2\omega^2 + \left[2a - \omega^2 - \frac{15}{4}aZ^2 - \frac{9}{2}\frac{a^2Z^2(1 - \frac{3}{2}Z^2)}{(2a - 4\omega^2 - 3aZ^2)}\right]^2\right\} - F^2 = 0 \tag{4.54}$$

Equation 4.54 relates the amplitude of the fundamental, Z, to the parameters of the system and is, therefore, a response curve. The character of the oscillation, for small Z^2, is identical to that of the SHO. Thus, equation 4.54 gives, for small Z^2:

$$Z = \pm\frac{F}{\sqrt{(2a - \omega^2)^2 + c^2\omega^2}} \tag{4.55}$$

where the 'resonant' frequency, $\omega = \frac{\sqrt{8a - 2c^2}}{2}$, implied by equation 4.55, is the same as that obtained by local linearisation of the force function (equation 1.5) about either of the nonzero equilibrium positions.

What then of larger oscillations? From the roots to equation 4.54, readily computed using an interval bisection algorithm (refer appendix B.4), we obtain figure 4.42, a plot of Z *vs* ω for different driver amplitudes F. The curves depicted in figure 4.42 do not necessarily correspond to stable solutions; they merely indicate the size of the fundamental if the solution takes the form of equation 4.47.

Consider for the moment the set of curves centred around $\omega_0 = 3.80$. As expected, for small driver amplitudes, the response curve resembles that of the driven SHO, but for larger F, the peak 'tilts' to the left - similar to the response

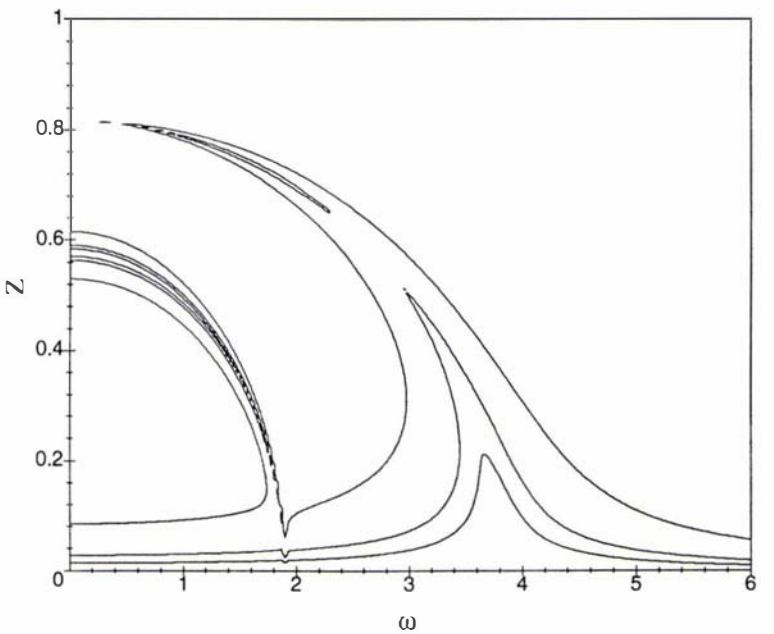

Figure 4.42: Z *vs* ω for $a = 7.21$, $c = 0.257$, $F = 0.2, 0.39, 1.2$.

of a soft spring. Equation 4.54 shows that for small ω, Z^2 tends towards 2/3, irrespective of F. The 'spine' on which these response curves are centred is therefore the first quadrant of the ellipse $\frac{3}{2}Z^2 + \frac{1}{2a}\omega^2 = 1$. This is made most evident by plotting Z^2 *vs* ω^2 with c and F small (figure 4.43). Also seen in figure 4.42 are a set of curves near $\omega = 2$. Their position, at a discontinuity in the Z *vs* ω curve, corresponds to the denominator of the quotient term in the square brackets of equation 4.54 being 0 for $Z = 0$; that is, for $\omega = \sqrt{a/2} = 1.90$. The solution described by these curves, while not completely stable, is in fact the low-frequency variation of the SW orbit (depicted in figure 3.25), an orbit which was observed experimentally.

The quotient term in the square brackets of equation 4.54 is the result of including the second harmonic component of the solution. If this is neglected ($C = D = 0$) as well as damping ($c = 0$), we obtain:

$$Z^2 \left\{ 2a - \omega^2 - \frac{15}{4} a Z^2 \right\}^2 - F^2 = 0 \tag{4.56}$$

This result is equivalent to equation 1.30 from section 1.4, obtained by applying Duffing's method. Thus, to first order, the methods produce the same results. The

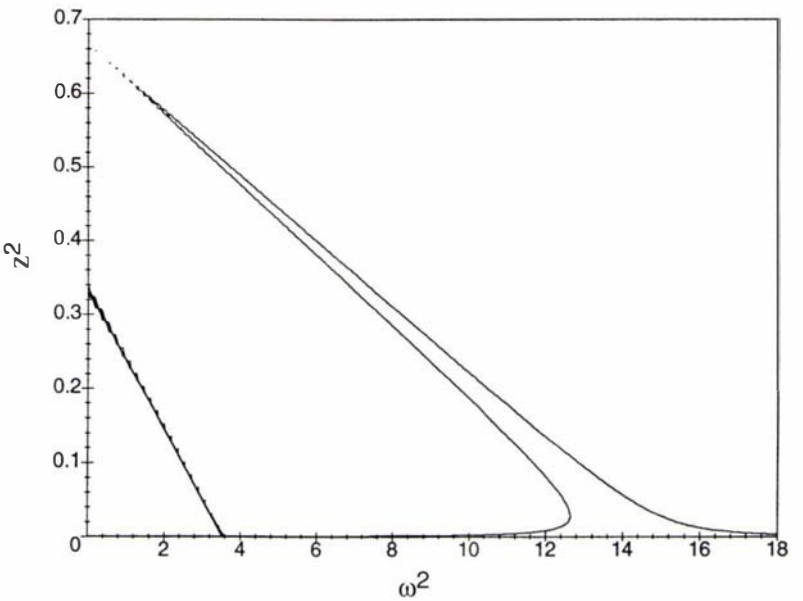

Figure 4.43: Z^2 *vs* ω^2 for $a = 7.21$, $c = 0.02$, $F = 0.2$.

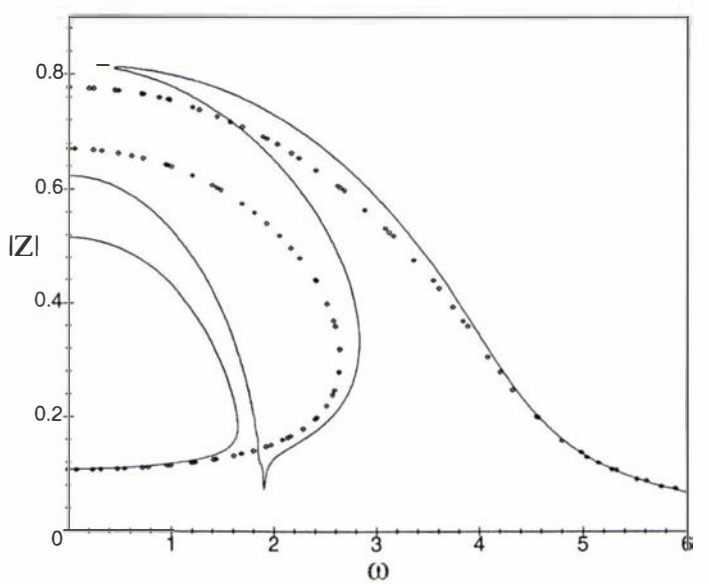

Figure 4.44: Comparison of response curves generated by Duffing's method (equations 1.30, 4.56) (points) and Harmonic Balance (equation 4.54) (solid line) for $F = 1.5$, $a = 7.21$, $c = 0$.

two response curves are shown in figure 4.44 where there is strong agreement for Z small. For larger Z there is a significant and, as we shall see, crucial, difference between the two - in addition to the extra set of curves equation 4.54 generates at low ω.

It is important to distinguish between the Harmonic balance technique used here and 'Duffing-style' iterative methods. Duffing nominates a first harmonic solution and integrates the differential equation. The result determines not only the amplitudes as a function of the parameters but also the form of the solution (in the twin well case, generating a second harmonic as expected). The Harmonic balance process, as we have employed it, requires the form of the solution to be nominated at the outset, thereby possibly gaining a 'head start'. Hayashi [12] presents a more comprehensive comparison of these and related techniques.

4.2 Criteria for Escape and Chaos

It is observed experimentally, that the onset of chaos, on the low frequency side, occurs at the point of vertical tangency in the response function and, on the high frequency side, when the SW orbit undergoes a bifurcation sequence[3] - facts also recognised by [14]. On the high frequency side, the bifurcation sequence begins when the SW orbit (as we have defined it) loses stability. On the low frequency side the SW orbit doesn't so much lose stability as cease to exist or, rather, at the point of vertical tangency, the anticipated hysteretic 'jump' leads to an unstable part of the response curve. Before attempting a stability analysis of the SW orbit however, it is worth exploring other avenues of enquiry.

4.2.1 Threshold Criteria

Perhaps the most intuitive approach to predicting escape from a well is to estimate the 'energy of escape' required to overcome the 'barrier' between the wells. Moon [18] estimates this energy from the Hamiltonian (refer section 1.4), thereby obtaining a 'critical amplitude' (or velocity). An (ω, F)-plane boundary can then be

[3] refer to figure 3.29, points 'a' and 'b' respectively.

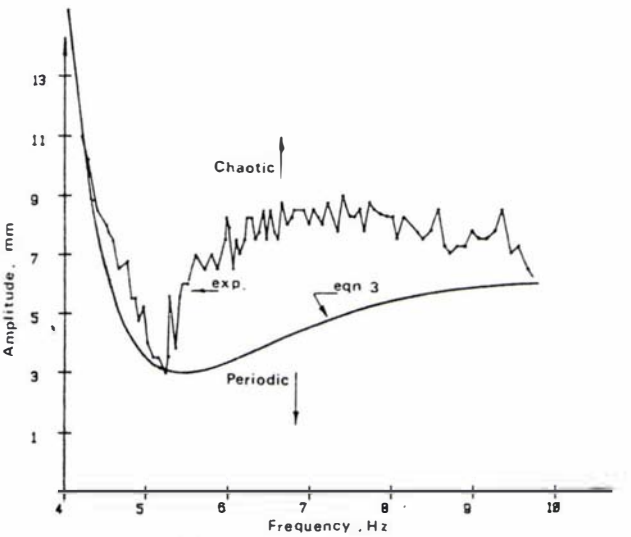

FIG. 3. Comparison of experimental and theoretical boundaries between periodic and chaotic vibrations.

Figure 4.45: Figure 3. reproduced from Moon [19]. Experimental data is accompanied by a curve given by equation 4.58.

obtained by substitution of this amplitude into a suitable SW orbit response function. Moon derives, via a perturbation method, the following response equation (using our symbols):

$$Z^2\left\{\left[2a-\omega^2-3aZ^2\right]^2+c^2\omega^2\right\}-F^2=0 \tag{4.57}$$

(Moon uses $a = 1/2$). The same expression can be obtained by neglecting the quotient term in equation 4.54 and approximating $\frac{15}{4}aZ^2$ with $3aZ^2$. The velocity of escape for the Hamiltonian, undriven case, $\sqrt{a/2}$, is then equated with ωZ. Recognising that escape occurs, in general, before this velocity is reached, Moon inserts an 'adjustable parameter', σ, to enable experimental data to be fitted, giving the following boundary equation

$$F=\frac{\sigma}{\omega}\sqrt{\frac{a}{2}}\left\{c^2\omega^2+\left[2a-\omega^2-\frac{3a^2\sigma^2}{2\omega^2}\right]^2\right\}^{1/2} \tag{4.58}$$

Moon's [19] experimental results are reproduced in figure 4.45 along with equation 4.58 fitted to the data.

There would seem to be little advantage in deriving such an equation if one

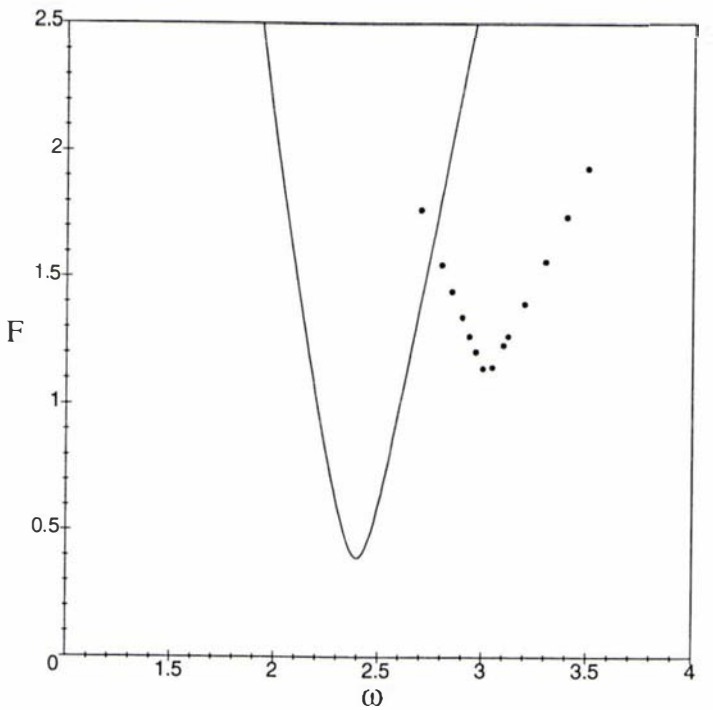

Figure 4.46: Theoretical escape boundary (solid line) derived from the response equation 4.54 with a 'critical amplitude' together with the numerically obtained boundary (points).

must then resort to using a 'fit factor'. One can, for example, achieve good fits to the chaos boundaries with straight lines - as was done in section 3.4. Continuing with the 'critical amplitude' theme, however, we may deduce that escape would occur approximately when $E^2 = Z^2$, that is, when the distance from the origin to the center of the oscillation is equal to the amplitude (of the fundamental). Substituting this condition in to equation 4.53 and solving, we obtain an 'escape amplitude' of $Z = \pm\sqrt{\frac{2}{5}} \approx \pm 0.63$. Substituting this value into the response equation (4.54) yields the curve shown in figure 4.46. Here we note a qualitative similarity in shape to the numerically obtained boundary but a distinct offset.

It is conceivable, given the definition of the low frequency side (point of vertical tangency in the response curve), that the estimate for this boundary could come from the response function alone. Regarding ω as dependent on Z, the point we seek is given by $\frac{d\omega}{dZ} = 0$. Implicit differentiation of equation 4.54 leading to solution for this point is not straight forward, and unlikely to be successful, although a simpler expression for the response (such as equation 1.30) will allow solution.

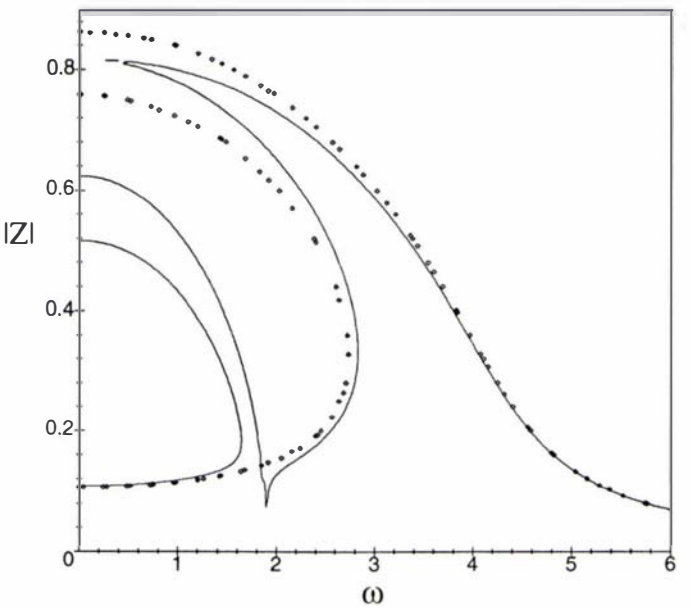

Figure 4.47: Simplified response curve (points) obtained from equation 4.60 together with the original response curve from equation 4.54 (solid line).

We therefore attempt to factorise equation 4.54, to produce a simpler expression for Z. The number of terms involved makes the process prohibitive and so we set $c = 0$ (system undamped) at the outset, enabling square roots to be taken throughout equation 4.54. Multiplying throughout then by $(2a - 4\omega^2 - 3aZ^2)^2$ however, and expanding, produces a polynomial of fifth order in Z with no obvious factors:

$$18\,a^2\,Z^5 + (-18\,a^2 + 18\,a\,\omega^2)\,Z^3 + 3\,F\,a\,Z^2 + (4\,a^2 + 4\,\omega^4 - 10\,a\,\omega^2)\,Z + (-2\,a + 4\,\omega^2)\,F = 0 \tag{4.59}$$

By trial and error it is found that the above factorises approximately to the following

$$2\,(3\,a\,Z^2 - a + 2\,\omega^2)\,(3\,a\,Z^3 - 2\,a\,Z + Z\,\omega^2 + F) = 0 \tag{4.60}$$

which, on expansion reproduces equation 4.59 except for the $3\,F\,a\,Z^2$ term which becomes $6\,F\,a\,Z^2$. This approximation has the effect of reducing the 'extra' set of curves at low ω to their spine i.e. the ellipse described by the first factor of equation 4.60. The rest of the response is therefore described by the second

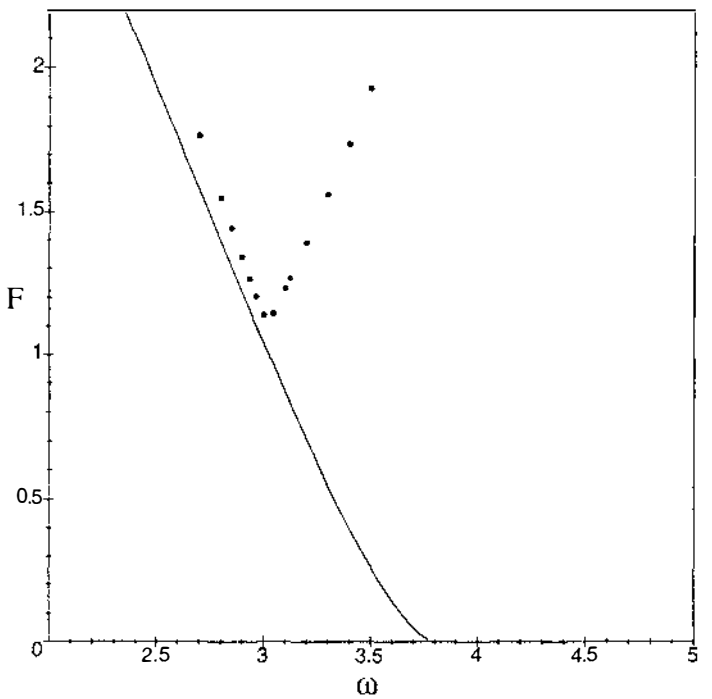

Figure 4.48: 'Low frequency' boundary from equation 4.61 (solid line) with the numerical boundary (points) for comparison.

factor, which is plotted in figure 4.47. After implicit differentiation and solution for $\frac{d\omega}{dZ} = 0$, we obtain the 'low frequency' boundary equation:

$$F = \frac{2}{9\sqrt{a}}(2a - \omega^2)^{3/2} \tag{4.61}$$

A plot of this boundary appears in figure 4.48 and shows a slight shift from the numerical points. This shift appears to be a consequence of the approximations made in obtaining the simplified response equation (4.47) as, in figure 4.47, a similar difference, $(\Delta\omega)$, exists between the vertical tangency points. Nevertheless, equation 4.61 is a reasonable 'first approximation' to the low frequency side of the boundary.

Encouraged by the relative success of the low frequency boundary analysis, one would hope that the high frequency side would also emerge from the analysis, however, the response equation gives no similar clues to predicting the high frequency side and, as well, we conclude that 'threshold' criteria are generally unsuccessful in reproducing the entire chaos boundary.

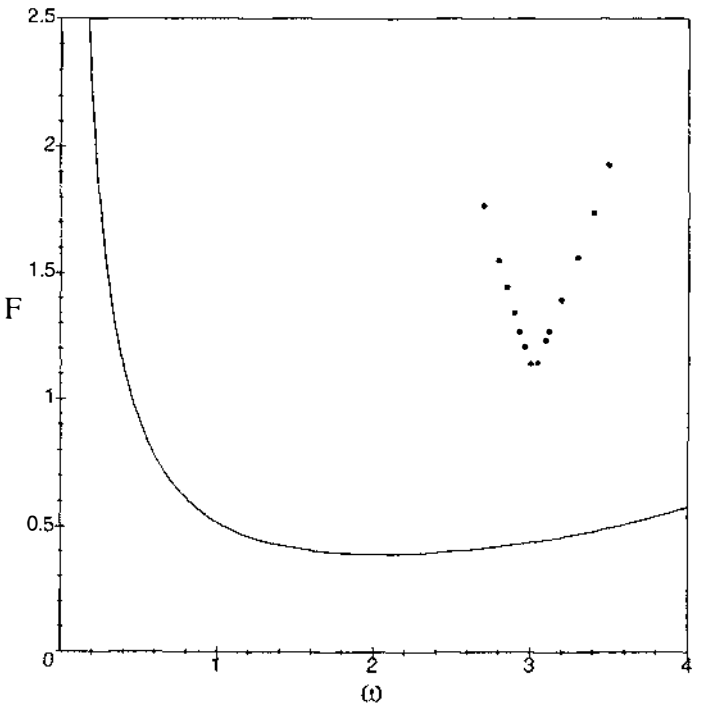

Figure 4.49: Holmes-Melnikov criterion for chaos (solid line) together with the numerical data.

4.2.2 Holmes-Melnikov Criterion

Guckenheimer and Holmes [11] present necessary conditions for a chaotic strange attractor in the Duffing twin-well system, based on a Melnikov homoclinic function, where the driven, damped system is regarded as a perturbation to the Hamiltonian, undriven system. In particular, conditions for homoclinic orbits to occur, are established from the 'level curves' of the undriven Hamiltonian system (refer to figure 1.9 of section 1.4) corresponding to $H = 0$ (refer equation 1.19). Without reproducing the theory, we state the result using our symbols

$$F_c = \frac{2c\sqrt{a}}{3\pi\omega} cosh(\frac{\pi\omega}{2\sqrt{a}}) \tag{4.62}$$

where homoclinic motions may occur for $F > F_c$. Equation 4.62 is then regarded as a lower bound for chaos. Figure 4.49 depicts this curve with our parameter values, and the numerical data for comparison. The similarity is remote but, as a necessary condition for chaos, the Holmes-Melnikov function does not *disagree*

with the numerical data.

4.3 Stability analysis of the SW orbit

The somewhat ad hoc methods of the previous sections enjoy mixed success in reproducing the chaos boundary, yet in theory, the answer is straightforward: We have a solution, $x = x(t)$, for the SW orbit which neighbours, in parameter space, the chaos region. Determining the regions of stability for the SW orbit solution will therefore determine the boundary with chaos. Here we mean stability in the Liapunov sense, that is, small perturbations to a solution die out with time (asymptotic orbital stability). If the perturbation grows with time, the SW orbit is unstable. If it neither grows nor decays then the SW orbit is orbitally stable but 'on the edge of stability', parameter-wise. It is this last situation which will indicate the boundary sought.

We perturb the solution and examine the equation which governs the perturbation. We do not necessarily require the full solution for the perturbation, but rather conditions establishing its growth or decay.

Let $\delta_0 = \delta_0(t)$ be a small perturbation to the SW solution $x = x(t)$ from equation 4.47. Substituting $X(t) = x(t) + \delta_0(t)$ in equation 1.18 gives:

$$\ddot{x} + \ddot{\delta_0} + c(\dot{x} + \dot{\delta_0}) + a(x + \delta_0)[(x + \delta_0)^2 - 1] = Fcos\omega t. \tag{4.63}$$

Recognising that $x = x(t)$ is a solution, expanding, neglecting δ_0 terms of order ≥ 2 and scaling, we obtain :

$$\ddot{\delta} + a\delta(3x^2 - \frac{c^2}{4a} - 1) = 0 \tag{4.64}$$

where $\delta(t) = exp(-\frac{c}{2}t)\delta_0(t)$.

As $x(t)$ is periodic (period $2\pi/\omega$), equation 4.64 has periodic coefficients and is a form of Hill's equation (Whittaker and Watson [34]). Floquet's theorem[4] implies that solutions may be expressed as $\delta(t) = p(t)exp(r_i t)$, where $p(t)$ is a periodic

[4]refer to a text on differential equations and stability theory of which Sanchez [27] is an example

function with period $2\pi/\omega$. Equation 4.64 is second-order and so there exist two linearly independent solutions of this form. Thus, the boundary we seek occurs when at least one of the r_i exceed $c/2$. One could, conceivably, find the boundary by numerically integrating equation 4.64 and looking for solutions with $exp(\frac{c}{2}t)$ growth, but there is probably no advantage in this over numerical integration of Duffing's equation itself.

The stability of solutions to Duffing's equation is often expressed in the form of equation 4.64 (see Stoker [28] for example). Our expression for $x(t)$ (equation 4.47) however, contains essentially three terms - a constant and two harmonics. Upon squaring we generate a constant plus four harmonics. In order to proceed, we must limit this number of terms without such an approximation being to the detriment of the overall analysis. This point is crucial. Although inclusion of the second harmonic in the SW orbit solution was vital to the harmonic balance procedure of section 4.1, we now neglect it and approximate the SW solution by the constant term and the fundamental:

$$x(t) = E + Zcos(\omega t + \phi) \tag{4.65}$$

which, after expressing E in terms of Z (equation 4.53) and substituting in equation 4.64, gives

$$\ddot{\delta} + J(\omega t)\delta = 0 \tag{4.66}$$

where $J(\omega t) = a\left(2 - 3Z^2 + 6\left(\sqrt{1 - \frac{3}{2}Z^2}\right)Zcos\omega t + \frac{3}{2}Z^2 cos2\omega t\right)$. The $\frac{c^2}{4a}$ in equation 4.64 term being small, is omitted as is the phase of $x(t)$ since this omission will simply 'shift' the phase of the solution. We note that while we have omitted the second harmonic from the solution $x(t)$, squaring produces another. If this new 2ω frequency term is omitted from $J(\omega t)$ then equation 4.66 becomes Mathieu's equation:

$$\ddot{\delta} + (q + pcos\omega t)\delta = 0 \tag{4.67}$$

where $q = a(2 - 3Z^2)$ and $p = 6a\left(\sqrt{1 - \frac{3}{2}Z^2}\right)Z$. Stability diagrams based on Mathieu's equation are common[5] but (as we shall see) our analysis will not tolerate such a degree of approximation. We must retain this second harmonic component of $J(\omega t)$ and the perturbation is governed by the more general form of Hill's equation that results.

In the context of Mechanics, equations such as 4.66 and 4.67 represent 'parametrically excited' systems. That is, they may be regarded as being driven by (sinusoidal) fluctuation of one of the parameters. We could, for example, regard equation 4.67 as governing the displacement, δ, of a mass hanging on a spring, whose stiffness constant, k varies as $k = q + pcos\omega t$. Pippard [24] tackles such problems as sinusoidal variation of the plate separation of a capacitor in a resonant LCR circuit and a simple pendulum which is driven by sinusoidal variation of its length. The former case is governed by Mathieu's equation and the latter, while being slightly more complex, is solved in [24] via Floquet's theorem and suitable approximations.

Retention of the second harmonic leaves us with a slightly more complex situation. Whittaker and Watson [34] deal with the more general form of equation 4.66, cited in [34] as arising from an 'astronomical' problem of Hill's, where $J(\omega t)$ is an infinite (convergent) series. Our problem is similar in spirit and we adopt the notation therein (replacing [34]'s z with $\omega t/2$). We express $J(\omega t)$ as

$$J(\omega t) = \theta_0 + 2\sum_{n=-\infty}^{\infty} \theta_n cosn\omega t \tag{4.68}$$

where $\theta_{-n} = \theta_n$, $\theta_{-n} = 0$ for $n \geq 0$ and

$$\theta_0 = 2aE^2, \quad \theta_1 = 3aZE, \quad \theta_2 = \frac{3}{4}aZ^2 \tag{4.69}$$

We express the solution (via Floquet's theorem) of equation 4.66 as

$$\delta = e^{\mu\omega t/2}\sum_{n=-\infty}^{\infty} b_n e^{ni\omega t} \tag{4.70}$$

[5]see Stoker [28] or Hagedorn [23] for example, or for comprehensive plots of the unstable regions of Mathieu's equation, Abramowitz and Stegun [2].

where μ may be complex. Substituting the expressions for $J(\omega t)$ and δ in equation 4.66 gives

$$\sum_{n=-\infty}^{\infty} (\mu+2ni)^2 b_n e^{(\mu/2+ni)\omega t} + \frac{4}{\omega^2}\left(\sum_{n=-\infty}^{\infty}\theta_n e^{ni\omega t}\right)\left(\sum_{n=-\infty}^{\infty} b_n e^{(\mu+ni\omega)t}\right) = 0 \quad (4.71)$$

Expanding and equating coefficients of $e^{ni\omega t}$ to zero, we obtain the following system of equations

$$(\mu+2ni)^2 b_n + \sum_{m=-\infty}^{\infty}\theta_m b_{n-m} = 0 \quad (n=-2,-1,0,1,2) \qquad (4.72)$$

where the θ_n have been adjusted to absorb the $\frac{4}{\omega^2}$ coefficient:

$$\theta_0 = \frac{8}{\omega^2}aE^2, \quad \theta_1 = \frac{12}{\omega^2}aZE, \quad \theta_2 = \frac{3}{\omega^2}aZ^2 \qquad (4.73)$$

We denote the determinant solution implied by the above (4.72) set of linear equations as $\Delta(\mu)=0$, where $\Delta(\mu)$ is given by

$$\begin{vmatrix}
(i\mu+4)^2-\theta_0 & -\theta_1 & -\theta_2 & -\theta_3 & -\theta_4 \\
-\theta_1 & (i\mu+2)^2-\theta_0 & -\theta_1 & -\theta_2 & -\theta_3 \\
-\theta_2 & -\theta_1 & i^2\mu^2-\theta_0 & -\theta_1 & -\theta_2 \\
-\theta_3 & -\theta_2 & -\theta_1 & (i\mu-2)^2-\theta_0 & -\theta_1 \\
-\theta_4 & -\theta_3 & -\theta_2 & -\theta_1 & (i\mu-4)^2-\theta_0
\end{vmatrix} \qquad (4.74)$$

Possible phase differences between δ and $J(\omega t)$ are handled by allowing the b_n to be complex, in which case phase terms of the form $e^{i\phi_n}$ will cancel throughout equation 4.71.

Careful consideration must now be given to choice of μ and hence the form of the perturbation. Let us write μ as $\mu = \epsilon + \sigma i$. The (exponential) growth or decay of δ is governed by positive or negative values of ϵ respectively. Thus the boundary between asymptotic orbital stability and instability occurs when $\epsilon = 0$. In order to determine σ, let us consider for the moment, the high frequency side of the boundary where the SW orbit undergoes a period-doubling bifurcation sequence prior to chaos, as seen experimentally in figures 3.26, 3.27 and 3.28.

Technically, the SW orbit has lost stability at the moment the first bifurcation occurs. Clearly then, the extra harmonics needed in the Fourier expansion of the SW orbit are those of the form $cos\frac{1}{2}\omega t$, $cos\frac{3}{2}\omega t \ldots$, that is, $cos\frac{n}{2}\omega t$ where n is odd: In other words, when $\sigma = \pm 1$, and hence $\mu = \pm i$. More simply, a period doubling cannot be described by equation 4.70 unless $\sigma = \pm 1$ and $\epsilon = 0$ at the bifurcation point (a similar choice of μ is made by Pippard [24] to describe oscillations of the pendulum which have twice the period of the excitation).

The condition for the high frequency side (at least) of the boundary is then described by

$$\Delta(i) = 0 \tag{4.75}$$

where the (4×4)[6] determinant corresponding to $\mu = i$ is

$$\Delta(i) = \begin{vmatrix} 9-\theta_0 & -\theta_1 & -\theta_2 & 0 \\ -\theta_1 & 1-\theta_0 & -\theta_1 & -\theta_2 \\ -\theta_2 & -\theta_1 & 1-\theta_0 & -\theta_1 \\ 0 & -\theta_2 & -\theta_1 & 9-\theta_0 \end{vmatrix} \tag{4.76}$$

The course of action now is to solve $\Delta(i) = 0$ for Z^2, given the expressions for θ_n. This would establish Z^2 as a function of ω which upon substitution in equation 4.54 will give rise to a relationship between F and ω which is the boundary that we seek. A difficulty arises in determining how large a matrix one requires (to retain accuracy) while still enabling solution. That is, how many harmonics of $J(\omega t)$ are required. A first approximation (with $\theta_2 = 0$, equation 4.66 becomes equivalent to Mathieu's equation) gives rise to the central 2×2 matrix, with $\Delta(i) = 0$ giving[7]

$$(1-\theta_0)^2 - \theta_1{}^2 = 0 \tag{4.77}$$

Substituting in the expressions for θ_0 and θ_1 (from 4.69), we obtain the approximate[8] result $Z^2 \approx \frac{2}{5}$ which is the same result obtained in section 4.2.1 via the

[6] as, for $\mu = i$, the determinant 4.74 becomes asymmetric, we omit the fifth row and column.

[7] cf. Hayashi's [12] condition $\theta_0 = n^2 \pm \theta_n$ for the boundary lines of the nth unstable region, assuming θ_n are small.

[8] for $a >> 1$

'escape condition' $E = Z$. More harmonics must be included and so we try the 4×4 determinant 4.76. The full expansion for which is given in appendix C.2 and factorises to:

$$(\theta_1{}^2 - 9\,\theta_1 - 9 - 2\,\theta_2\,\theta_1 + \theta_2{}^2 + \theta_1\,\theta_0 + 10\,\theta_0 - \theta_0{}^2)\times$$
$$(\theta_1{}^2 + 9\,\theta_1 - 9 + 2\,\theta_2\,\theta_1 + \theta_2{}^2 - \theta_1\,\theta_0 + 10\,\theta_0 - \theta_0{}^2) = 0 \qquad (4.78)$$

The terms obtained by substituting in (each factor) of equation 4.78 the expressions for the θ_n (equation 4.73), include those of order Z, Z^2, EZ^3 and Z^4 - preventing a convenient factorisation (and hence solution for Z^2).

Progress can be made however, by representing δ differently. With $\mu = i$ the expression for δ can be rearranged to the following:

$$\delta = \sum_{n=-\infty}^{\infty} b_n e^{ni\frac{1}{2}\omega t} \qquad (4.79)$$

where $b_n = 0$ for n even. This is equivalent to the previous description with $\mu = 0$ and new θ_n given by

$$\theta_0 = \frac{32}{\omega^2}aE^2, \quad \theta_1 = \frac{48}{\omega^2}aZE, \quad \theta_2 = \frac{12}{\omega^2}aZ^2 \qquad (4.80)$$

The corresponding (5×5) determinant is

$$\Delta(0) = \begin{vmatrix} 16-\theta_0 & -\theta_1 & -\theta_2 & 0 & 0 \\ -\theta_1 & 4-\theta_0 & -\theta_1 & -\theta_2 & 0 \\ -\theta_2 & -\theta_1 & -\theta_0 & -\theta_1 & -\theta_2 \\ 0 & -\theta_2 & -\theta_1 & 4-\theta_0 & -\theta_1 \\ 0 & 0 & -\theta_2 & -\theta_1 & 16-\theta_0 \end{vmatrix} \qquad (4.81)$$

Upon expansion (refer appendix C.2) this determinant factorises to the following

$$-(-16\,\theta_2 + \theta_2\,\theta_0 - 64 + 20\,\theta_0 - \theta_0{}^2 + \theta_1{}^2)(2\,\theta_2{}^3 + 2\,\theta_2{}^2\,\theta_0 - 8\,\theta_2{}^2 - \theta_2\,\theta_0{}^2$$
$$+ 16\,\theta_2\,\theta_0 - \theta_0{}^3 + 20\,\theta_0{}^2 - 64\,\theta_0 - 4\,\theta_2\,\theta_1{}^2 - 32\,\theta_1{}^2 + 3\,\theta_0\,\theta_1{}^2) = 0 \qquad (4.82)$$

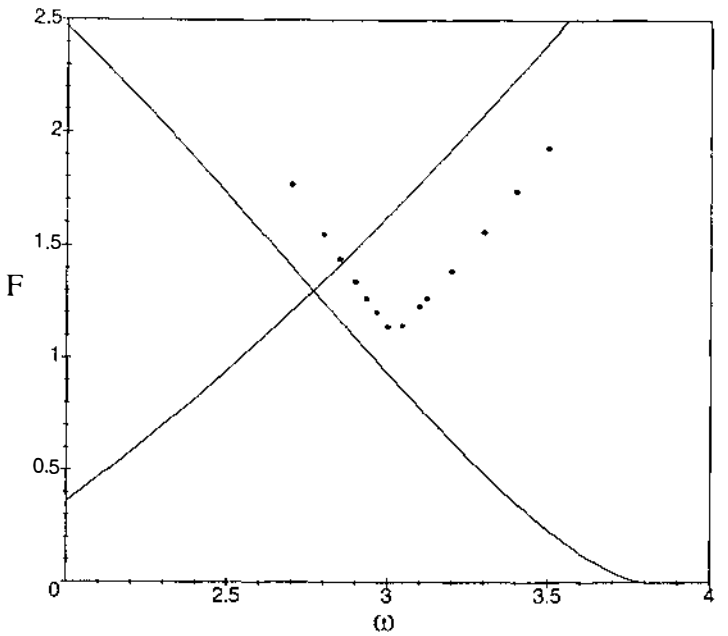

Figure 4.50: Boundary lines generated using the stability condition equation 4.84 with the response equation generated via Duffing's method (equation 1.30) together with numerically obtained points for the same parameters.

Substituting in the expressions for the θ_n (4.80) in the second factor, we see that the only terms which won't give rise to products containing E^2 are ${\theta_2}^3$ and $8{\theta_2}^2$ which, for the sake of factorisation, we neglect[9]. Making these substitutions and multiplying throughout by ω^6, we obtain

$$256\,a\,E^2\,(477\,a^2\,Z^4 - 300\,a^2\,Z^2 + 96\,a\,\omega^2\,Z^2 + 32\,a^2 - 20\,a\,\omega^2 + 2\,\omega^4) = 0 \quad (4.83)$$

The second factor of equation 4.83, being a quadratic in Z^2, gives rise to the following expression

$$Z^2 = \frac{1}{159a}\,(50\,a - 16\,\omega^2 \pm \sqrt{804\,a^2 - 540\,a\,\omega^2 + 150\,\omega^4}) \qquad (4.84)$$

The above is a stability condition, which, upon substitution in a response equation will give rise to the chaos boundary. In order to emphasise the importance of an accurate response equation, we first substitute equation 4.84 in the response

[9]this is justified by the fact that θ_2 is smaller than θ_0, θ_1.

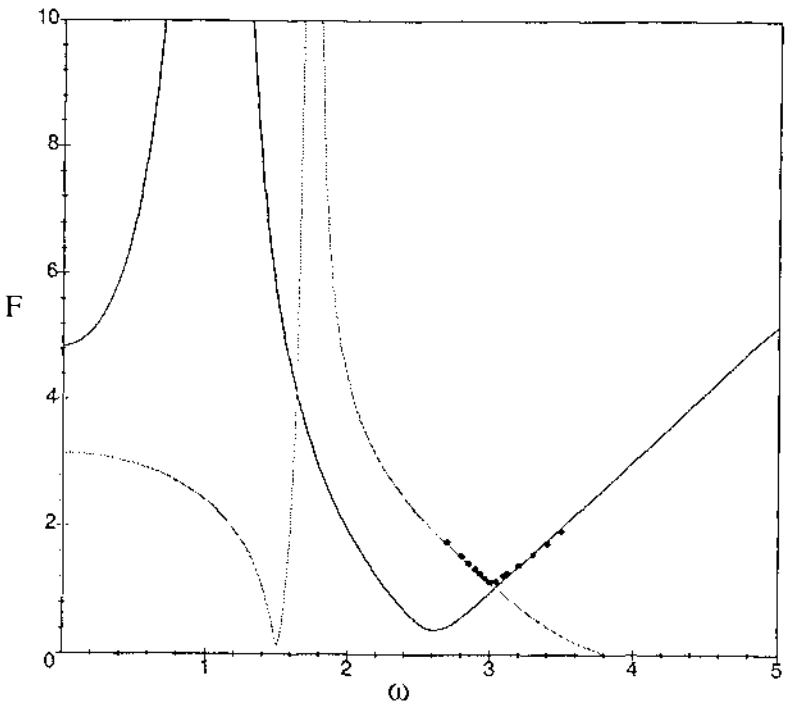

Figure 4.51: Boundary lines generated by equation 4.85 for the system parameters together with the numerical points; F_+: heavy line, F_-: light line.

equation generated via Duffing's method (refer equation 1.30). Eliminating Z^2 thereby establishes F as a function of ω and gives rise to the lines shown in figure 4.50. The distinct difference between the boundary lines and the numerical points seen in figure 4.50 is remedied by using the harmonic balance derived response equation (equation 4.54). Eliminating Z^2 between equations 4.84 and 4.54 establishes the boundary lines of stability for the SW orbit, that is, $F = F_\pm(\omega)$ where the $+/-$ denote high and low frequency sides respectively. The full, closed expression for $F_\pm(\omega)$ is ungainly and so we define the boundary lines by the following

$$F_+(\omega) = \sqrt{Z^2\left\{\omega^2\omega^2 + \left[2a - \omega^2 - \frac{15}{4}aZ^2 - \frac{9}{2}\frac{a^2Z^2(1-\frac{3}{2}Z^2)}{(2a-4\omega^2-3aZ^2)}\right]^2\right\}} \qquad (4.85)$$

where

$$Z^2 = \frac{1}{159a}\left(50\,a - 16\,\omega^2 \pm \sqrt{804\,a^2 - 540\,a\,\omega^2 + 150\,\omega^4}\right) \qquad (4.86)$$

Figure 4.51 shows the boundary lines generated by equation 4.85 for the system

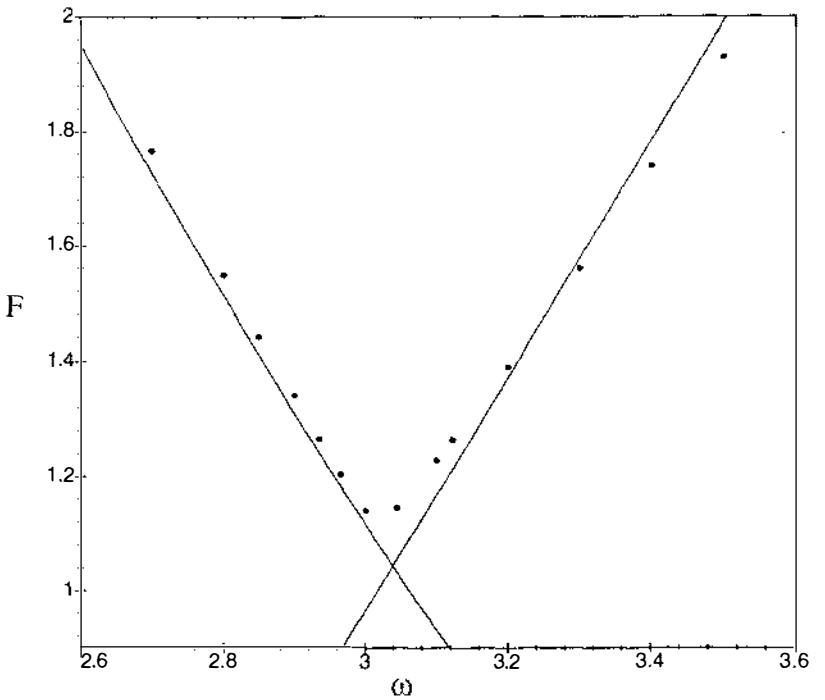

Figure 4.52: Detail of the plot of the analytic boundaries (solid lines) from equation 4.85 for the system parameter values (table 3.3) together with the numerical points in the chaos region.

parameters of table 3.3. While the lines show much character over a broad range of ω and Γ, they are reasonably linear near the chaos region. An enlarged scale in figure 4.52 shows strong agreement between equation 4.85 with the numerically obtained points.

What is perhaps surprising about the above results is that the preceding analysis was expected to yield an expression for the high frequency boundary alone as the choice of $\mu = i$ is specific to the period doubling bifurcation. It would appear then, that the low frequency boundary, being very much a consequence of the nature of the response curve, is largely *insensitive* to the form of the perturbation and, conveniently, is modelled by the *same* analysis.

Strictly speaking, the high frequency boundary, given by $F_+(\omega)$, is the boundary for the onset of the bifurcation sequence rather than chaos or escape, but, as the experimental and numerical results reveal, the bifurcation sequence is narrow enough in ω terms for us to regard $F_+(\omega)$ as a strong indicator of the chaos boundary. The validity of this assumption is borne out in figure 4.52.

Chapter 5

Conclusion

Performing experiments in nonlinear dynamics (or physics in general) provides one with an 'acid test' for any analysis be it by computer simulation and/or theoretical modelling. Moreover, an experiment forces one to use realistic parameters in such analyses, removing the temptation to use approximations that would simplify the theory but lack significance or to just wander off into distant and unattainable regions of parameter space.

The resolution limitations of a real experiment are also exposed, a situation clearly shown in the bifurcation sequence which, though predicted numerically, is not observed past the second bifurcation with the present apparatus.

In short, the experiment imposes a sober resolve both on the data and on the analysis. The experimental data then make the theory more relevant and, given an analytical - rather than a numerical - approach, the whole is intellectually satisfying. (Note that the numerical solution (e.g. RK4) is not necessarily the ultimate 'fall-back' position for determining the actual behaviour of a dynamical system; the delicate matter of the 'stability of the integration algorithm' and the possible spurious behaviour so generated casts a shadow over all such calculations. This matter is generally ignored in the hope that it is not happening.)

The essence of this thesis is contained in figure 3.39, reproduced again below. The experimental boundary lines in parameter space were determined corresponding to the various patterns of oscillatory behaviour. Stability analysis then enabled

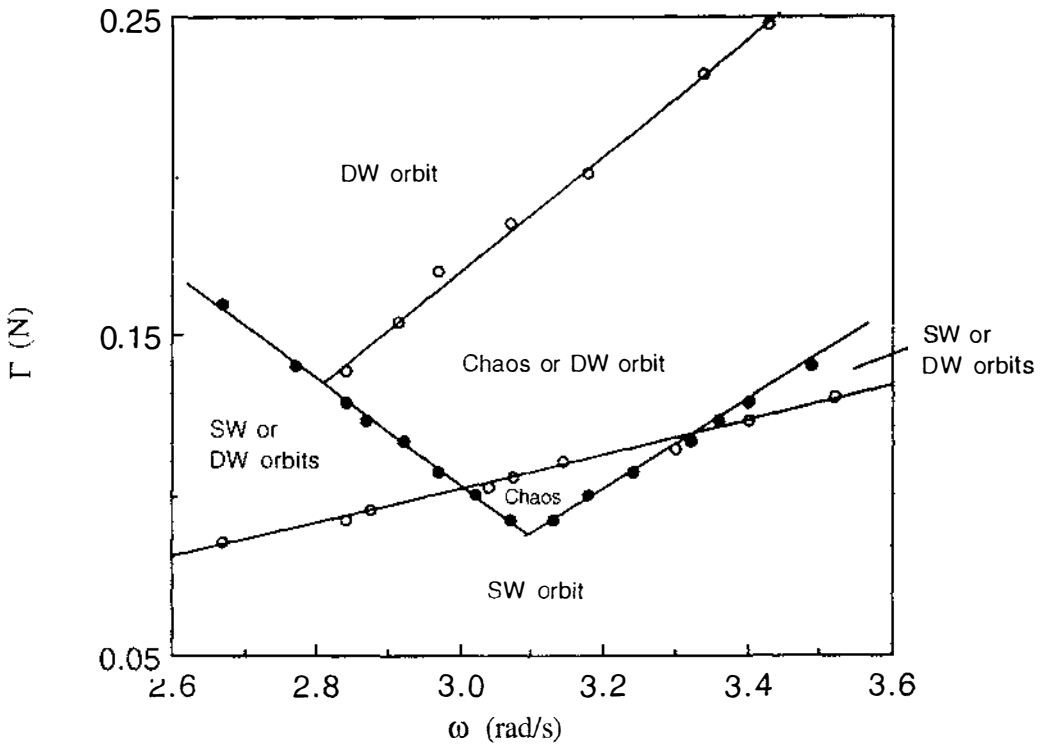

Figure 5.53: Plot of all experimental boundaries in the (ω, Γ)-plane. Reproduced from figure 3.39, section 3.6.

two of the boundary lines to be well reproduced analytically. Software here developed enabled Poincaré sections to be measured and displayed in real time and, using only this data, a reliable estimation of the maximum Lyapunov exponent was made.

Given the relative success of the apparatus in reproducing the dynamics of the twin-well oscillator, we conclude that it is a substantial improvement on the 'magneto-elastic' systems of [19] or [4]. The improvement clearly stems from the fact that the force function is, in the present case, mathematically simple and minimal, a property which enables the parameter space boundaries to be analytically determined. This being the case, the character of the twin well system is the more clearly revealed.

Moreover, the apparatus is flexible in its application since any smoothly varying driving force can be programmed and applied to the oscillating mass through the stepping motor system. Therefore, if the potential function can be configured on the track with the appropriate springs, barriers, etc., the system can be experimentally examined. In these respects the apparatus is an improvement

over the two previous twin-well systems. Also, the V-scope detection system and the software here developed allows rapid implementation of such custom designed experiments with storage and retrieval of the results. A Poincaré section for example, could be performed for any oscillation configured on the air track.

The theoretical component of this investigation has been an exercise in making feasible approximations. It is fair to say that the analysis has been 'near Hamiltonian', that is, damping has always been considered as slight, as is observed experimentally. The quality of the approximations would likely be degraded under conditions of higher damping, where, it has been mooted (Moon [18]), the accuracy of the Holmes-Melnikov criterion for chaos improves.

Notwithstanding the above, the analytic result for the chaos boundary developed here shows splendid agreement both with experiment and the numerical results. The importance of such a *fully* analytic solution should not be understated. If criteria for chaos, as Kapitaniak [16] suggests, are to be used to predict areas of parameter space where "strange phenomena" may take place, then not having to rely on numerical methods results in a vast saving of time.

In summary then, the theory developed here accurately models the chaos boundary in the Duffing twin-well oscillator. Harmonic balance techniques are used to accurately model the single well response. The stability of these solutions are established via perturbation techniques, Hill's equation and Floquet's theorem. The solution thus obtained gives rise to a closed expression for F in terms of ω.

In any investigation the process of answering questions poses more. Thus the boundary for double well orbit stability and the boundary for the chaos-DW orbit transition (refer figure 5.53) have eluded analysis. Of these, analysis of the former is probably the most likely to yield a result, which in theory might be accomplished by a stability analysis of the DW orbit. Like the SW orbit analysis, this would involve modelling the response curve - which may be difficult as the oscillations are large and harmonics above the fundamental are likely to be much more significant. This consideration alone would have implications for the rest of the analysis.

The chaos-DW orbit transition poses an even greater challenge as this boundary is not defined by the loss of stability of any given periodic mode, but rather of chaos itself. Does this mean a stability analysis for chaos? Perhaps the way forward is to think of the chaotic regions of parameter space as those where positive Lyapunov exponents are possible. This definition is not without difficulty since it would require establishing analytic expressions for the Lyapunov exponents as functions of the parameters. Given the inherent statistical nature of the exponents, this task appears formidable, possibly intractable. Nevertheless, the boundaries exist and are well defined.

Appendix A

Apparatus Specifications

A.1 V-scope Data Records

(a)

Data i.d.	record no.	length	x	Button no.	x	Button no.	check sum
1 byte	1 byte	1 byte	2 bytes	1 byte	2 bytes	1 byte	1 byte

(b)

Data i.d.	status	Binary info.	Analog info.
1 byte	1 byte	1 byte	1 byte

Appendix B

Pascal Code

B.1 Poincaré plot algorithm

```
program poincare;
 {       For direct communication between Vscope and the PC      }

 uses
  Crt, comms, Graph;

 var
  grdriver, grmode, i, x, a, b, d, n: integer;
  origin: longint;
  f, g, h: text;
  k, v, p, samp, total, t, ov, inf, ka: real;
  s, letter: string;
  c: char;
  started: boolean;
  dataid, recordno, length, hix, lox, button, checksum: byte;
  bininf, bininf1, bininf2, bininf3, aninf, status: byte;
  y: array[1..5] of real;

 label
  1;

 procedure waitdata;
 begin
  while (BytesInBuffer = 0) do
   ;
 end;

procedure drawaxes;
```

```
begin
 setcolor(10);
 a := round(getmaxX / 2);
 b := round(getmaxY / 2);
 d := 9;
 Rectangle(0, 0, getmaxX, GetmaxY - d);
 line(a, 1, a, 20);
 line(a, getmaxY - d - 1, a, getmaxy - 20 - d);
 line(1, b - round(d / 2), 20, b - round(d / 2));
 line(getmaxX - 1, b - round(d/2),getmaxX-20,b-round(d/2));
 line(a, b - 20 - round(d / 2), a, b + 20 - round(d / 2));
 line(a - 20, b - round(d / 2), a + 20, b - round(d / 2));
 Setcolor(15);
 SetTextStyle(2, HorizDir, 4);
 RESET(g);
 readln(g, letter);
 OutText(letter);
end;

procedure readdata;
 var
  rec: byte;
begin
 repeat
  waitdata;
  dataid := ReadByteFromBuffer;
 until (dataid = ord('D'));
 waitdata;
 rec := ReadByteFromBuffer;
 waitdata;
 length := ReadByteFromBuffer;
 waitdata;
 hix := ReadByteFromBuffer;
 waitdata;
 lox := ReadByteFromBuffer;
 waitdata;
 button := ReadByteFromBuffer;
 waitdata;
 checksum := ReadByteFromBuffer;
 waitdata;
 dataid := ReadByteFromBuffer;
 waitdata;
 status := ReadByteFromBuffer;
 waitdata;
 bininf1 := ReadByteFromBuffer;
 waitdata;
 bininf2 := ReadByteFromBuffer;
```

```
  waitdata;
  bininf3 := ReadByteFromBuffer;
  waitdata;
  aninf := ReadByteFromBuffer;
  x := hix;
  x := ( x shl 8 ) or lox;
  recordno := recordno + 1;
end;

procedure Setorigin;
 begin
 write('Place Glider at Reference Frame origin');
 writeln('and press SPACE else RET');
  c := readkey;
  writeln;
  origin := 10057;{DEFAULT}
  if c = ' ' then
   begin
    Sendstring('START');
    repeat
     readdata;
     n := n + 1;
     total := total + x;
    until n = 100;
    origin := round(total / 100);
    Sendstring('PAUSe');
   end;
 end;

begin
 inf := 0;
 ka := 0;
 t := 0;
 n := 0;
 total := 0;
 samp := 0.03;
 recordno := 0;
 i := 0;
 setserialport;
 enableport;
 clearbuffer;

 assign(f, 'commands.txt');
 reset(f);

 while not eof(f) do
  begin
```

```
  readln(f, s);
  Sendstring(s);
  delay(500);
  while (BytesInBuffer <> 0) do
   write(chr(ReadByteFromBuffer));
 end;

Sendstring('VSOU=A');
assign(g, 'details.txt');
rewrite(g);
assign(h, '5th.txt');
rewrite(h);
SetOrigin;

writeln('Hit anything to start reading');
c := readkey;
grdriver := Detect;
grmode := 2;
InitGraph(grdriver, grmode, 'C:\BP\BGI');
ClearViewPort;
drawaxes;
Sendstring('START');

while not keypressed do
 begin
  readdata;
  t := t + samp;
  {code to process x}
  i := 1;
  repeat
   i := i + 1;
   y[i] := y[i - 1];
  until i = 5;
  Nosound;
  if length = 3 then
   begin
    y[1] := (origin - x) / 10000;
    v := (2 * (y[5] - y[1]) + y[4] - y[2]) / (10 * SAMP);
     { if (((v - ov) < 0.1) and ((v - ov) > -0.1)) then}
    if aninf >= 192 then
     begin
      inf := 0;
      if ka <> inf then
      begin
putpixel(round(a*(1.7*(y[3])+1)),round((b*(5*v+1))-d/2),15);
write(h, y[3] : 3 : 4, chr(9));
write(h, -v : 3 : 4, chr(9));
```

```
 writeln(h, t : 5 : 4, chr(9));
 sound(1000);
       end;
      end;
     if aninf < 133 then
      inf := 1;
     ka := inf;
    end;
  end;

 c := readkey;
 Sendstring('STOP');
 drawaxes;

 repeat
  delay(200);
 until keypressed;

 c := readkey;
 disableport;
end.
```

B.2 Stepped sinewave Fourier analysis

```
program stepping;

 var
  k, m: integer;
  A, x, s, sum: real;
  f: text;
 const
  d = 1; {step size}
  N = 50; {amplitude in steps}
  pi = 3.14159;
  terms = 5001; {no. of terms in series expansion}

begin
 rewrite(f, '130796.out');
 A := d * N;
 k := -1;
 repeat
  k := k + 2;
  sum := 0;
  s := 0;
```

```
  for m := 1 to N do
   begin
    x := (m - 0.5) / N;
    s := cos(k * arctan(x / sqrt(1 - x * x)));
    sum := sum + s;
   end;
  sum := sum * 4 * d / (k * pi);
  writeln(f, k, chr(9), sum : 2 : 5);
 until k = terms;
 close(f);
end.
```

B.3 Fourier Representation Algorithm

```
program FT;

 const
  n = 10;
  npts = 600;
  hnpts = 300;
  pi = 3.14159;

 var
  T, dt, cso, sso, cs1, ss1, cs2, ss2, amp, phase, tot: real;
  foo, fo1, fo2, Ao: real;
  i, m: integer;
  input, output: text;
  x: array[0..npts, 1..2] of real;
  y: array[0..npts, 1..2] of real;
  A: array[1..n, 1..2] of real;

 function sgn (u: real): integer;
 begin
  if u < 0.0 then
   sgn := -1
  else
   sgn := 1;
 end;

begin
{Program to accept data file of npts points sampled from a periodic signal}
{dt apart, period T. One cycle only.}

 showtext;
```

```
 reset(input, '15398.TXT');
 tot := 0;
 for i := 0 to npts do {read in the input file to array x}
  begin
   read(input, x[i, 1]);
{writeln(x[i, 1] : 2 : 3);}
   readln(input, x[i, 2]);
  end;
 writeln;
 rewrite(output, NewFileName(''));

 dt := x[2, 1] - x[1, 1];
 T := x[npts, 1] - x[0, 1];

 writeln;
 for m := 1 to n do
  begin
   for i := 0 to npts do
    begin
     y[i, 1] := 2 * x[i, 2] * sin(m * 2 * pi * x[i, 1] / T);
     y[i, 2] := 2 * x[i, 2] * cos(m * 2 * pi * x[i, 1] / T);
    end;

   ss1 := 0;
   cs1 := 0;
   ss2 := 0;
   cs2 := 0;
   sso := y[0, 1] + y[npts, 1];
   cso := y[0, 2] + y[npts, 2];

   for i := 1 to hnpts do
    begin
     ss1 := y[2 * i - 1, 1] + ss1;
     cs1 := y[2 * i - 1, 2] + cs1;
    end;

   for i := 2 to hnpts do
    begin
     ss2 := y[2 * i - 2, 1] + ss2;
     cs2 := y[2 * i - 2, 2] + cs2;
    end;


   A[m, 1] := (sso + 4 * ss1 + 2 * ss2) * dt / (3 * T);
   A[m, 2] := (cso + 4 * cs1 + 2 * cs2) * dt / (3 * T);

   amp := sqrt(A[m, 1] * A[m, 1] + A[m, 2] * A[m, 2]);
```

```
   tot := tot + amp * amp;
   phase := arctan(A[m, 2] / A[m, 1]);

   write(m, '     ');
   if sgn(A[m, 2]) > 0 then
    write(' ');

   write(A[m, 2] : 2 : 5, '     ');

   if sgn(A[m, 1]) > 0 then
    write(' ');

   write(A[m, 1] : 2 : 5, '     ', amp : 2 : 5, '          ');


   if sgn(A[m, 1]) = sgn(A[m, 2]) then
    write(' ');

   writeln(A[m, 1] / A[m, 2] : 2 : 5);
   writeln(output, m, chr(9), A[m, 2] : 2 : 5, chr(9), A[m, 1] : 2 : 5);

  end;

{constant term:}

 fo1 := 0;
 fo2 := 0;
 foo := x[1, 2] + x[2 * hnpts, 2];

 for i := 1 to hnpts do
  begin
   fo1 := x[2 * i - 1, 2] + fo1;
  end;

 for i := 2 to hnpts do
  begin
   fo2 := x[2 * i - 2, 2] + fo2;
  end;

 writeln;
 Ao := (foo + 4 * fo1 + 2 * fo2) * dt / (3 * T);
 writeln('      ', Ao : 2 : 6);
 writeln;

 writeln(output);
 writeln(output, Ao : 2 : 5);
 close(input);
```

```
 close(output);
 writeln;


end.
```

B.4 Interval Bisection algorithm

```
 program util;

 const
  c = 0.2573;
  a = 7.21;
  b = 129.73;
  pi = 3.14159;
  zo = 0.13;
  winc = 0.025; {0.025}
  finc = 0.1; {0.01}

 var
  z, T, Tdash, w, f, zold, marker, znew, zinc: real;
  n, j: integer;
  roots: array[1..8] of real;
  input, output: text;

 function sgn (u: real): boolean;
 begin
  if u < 0.0 then
   sgn := false
  else
   sgn := true;
 end;

 function res (x: real): real;
  var
   ws, zs, brb, brc: real;
 begin
  zs := x * x;
  ws := w * w;
  brb := 14.42 - ws - 21.63 * zs;
  brc := (-233.92845 * zs +350.892675*zs*zs)/(14.42-4*ws-21.63*zs);
  res := x * sqrt(0.06620329 * ws + (brb + brc) * (brb + brc)) - f;
 end;
```

```
begin
 showtext;
 zinc := 0.0001; {0.0001}
 rewrite(output, 'test.txt');
 f := 0.1 - finc;
 repeat
  f := f + finc;
  w := 0;
  writeln(f : 2 : 3);
  repeat
   z := 0.001;
   if w > 0.8 then
    zinc := 0.01;
   w := w + winc;
  repeat
     if sgn(res(z)) <> sgn(res(z + zinc)) then
     begin
      n := 0;
      marker := z;
      zold := z + zinc;
      znew := z + zinc / 2;
      repeat
       n := n + 1;
      if sgn(res(znew)) <> sgn(res(z)) then
       begin
        zold := znew;
        znew := (z + znew) / 2
       end
       else
       begin
        z := zold;
        zold := znew;
        znew := (z + zold) / 2;
       end;
  until (sqrt((z - znew) * (z - znew)) < 0.0000001) or (n>1000);
  writeln(output, w : 2 : 3, chr(9), z : 2 : 5, chr(9), f : 2 : 3);
{writeln((z - znew) : 2 : 8, '     ', n);}
     end;
     z := z + zinc;
   until z > 0.88;
  until w > 8;
 until f > (2);
 close(output);
end.
```

B.5 Lyapunov Exponents

```
program lyapunov;

 var
  i, k, z, marker: integer;
  xp: array[1..3000, 1..2] of real;
  d, dn, l, value, dir, direction, prox: real;
  total, old, ang: real;
  f, g: text;

 const
  max = 0.05;
  min = 0.01;
  w = 3;
  pi = 3.14159;
begin

 ang := 5;
 assign(f, '530699.asc');
 reset(f);
 marker := 3;
 old := 4;
 dir := 1.4;

 for i := 1 to 3000 do
  begin
   read(f, xp[i, 1]);
   readln(f, xp[i, 2]);
  end;

 writeln('Finished read');
 i := 1;
 total := 0;
 k := 0;
 z := 0;
 repeat
  i := i + 1;
  z := i;
  repeat
   z := z + 1;
   dn:=sqrt(sqr(xp[i,1]-xp[z,1])+sqr(xp[i,2]-xp[z,2]));
   direction := pi / 2;
   if (xp[i, 1] - xp[z, 1]) <> 0 then
    begin
 direction:=arctan((xp[i,2]-xp[z,2])/(xp[i,1]-xp[z,1]));
```

```
    end;

   prox := sqrt(sqr(direction - dir));

until(((dn<=max)and(dn>= min))and(prox<ang))or(z>(2900));

  if (z < (2900)) then
   begin
   d:=sqrt(sqr(xp[i+1,1]-xp[z+1,1])+sqr(xp[i+1,2]-xp[z+1,2]));
    l := ln(d / dn) / ln(2);
   if i > 250 then
     begin
      total := total + l;
      k := k + 1;
      writeln(total / k : 2 : 3, '     ', dir : 2 : 3);
      ang := 0.1;
     end;
   dir := pi / 2;
   if (xp[i + 1, 1] - xp[z + 1, 1]) <> 0 then
   dir:=arctan((xp[i+1,2]-xp[z+1,2])/(xp[i+1,1]-xp[z+1,1]));
   marker := z + 1;
   end;

  if (z > (2900)) then
   begin
    z := marker + 1;
    dir := pi / 2;
    if (xp[i + 1, 1] - xp[z, 1]) <> 0 then
    dir:=arctan((xp[i+1,2]-xp[z,2])/(xp[i+1,1]-xp[z,1]));
    marker := z;
    writeln('*      ', dir : 2 : 3);
   end;

 until i > 2900;
 close(f);
 end.
```

Appendix C

Derivations for chapter 4.

C.1 Derivation of response function by Harmonic Balance

We start with the two frequency solution (equation 4.47):

$$x(t) = E + Acos(\omega t) + Bsin(\omega t) + Ccos(2\omega t) + Dsin(2\omega t) \tag{C.87}$$

differentiating and substituting in equation 1.18 we obtain:

$$\begin{aligned}
&-A\cos(w\,t)\,w^2 - B\sin(w\,t)\,w^2 - 4\,C\cos(2\,w\,t)\,w^2 - 4\,D\sin(2\,w\,t)\,w^2 \\
&+ c\,(-A\sin(w\,t)\,w + B\cos(w\,t)\,w - 2\,C\sin(2\,w\,t)\,w + 2\,D\cos(2\,w\,t)\,w) + \\
&a((E + A\cos(w\,t) + B\sin(w\,t) + C\cos(2\,w\,t) + D\sin(2\,w\,t))^3 - E \\
&- A\cos(w\,t) - B\sin(w\,t) - C\cos(2\,w\,t) - D\sin(2\,w\,t)) = f\cos(w\,t)
\end{aligned} \tag{C.88}$$

expanding the above gives:

$$\begin{aligned}
&-\frac{3}{4}B^2\,C\,a + \frac{3}{2}B^2\,E\,a + \frac{3}{2}B\,a\,A\,D + \frac{3}{2}C^2\,E\,a + \frac{3}{4}C\,a\,A^2 + E^3\,a + \frac{3}{2}E\,a\,A^2 \\
&+ \frac{3}{2}E\,a\,D^2 - E\,a + (\frac{3}{4}B^3\,a + \frac{3}{2}B\,C^2\,a - 3\,B\,C\,E\,a + 3\,B\,E^2\,a + \frac{3}{4}B\,a\,A^2 \\
&+ \frac{3}{2}B\,a\,D^2 + 3\,E\,a\,A\,D - w^2\,B - w\,A\,c - B\,a)\sin(w\,t) + (\frac{3}{4}B^2\,a\,A \\
&+ 3\,B\,E\,a\,D + \frac{3}{2}C^2\,a\,A + 3\,C\,E\,a\,A + 3\,E^2\,a\,A + \frac{3}{4}a\,A^3 + \frac{3}{2}a\,A\,D^2 - w^2\,A
\end{aligned}$$

$$
\begin{aligned}
&+ w\,B\,c - a\,A)\cos(w\,t) + (-\frac{3}{4}\,B^2\,a\,A + \frac{3}{2}\,B\,C\,a\,D - 3\,B\,E\,a\,D + \frac{3}{4}\,C^2\,a\,A \\
&+ 3\,C\,E\,a\,A + \frac{1}{4}\,a\,A^3 - \frac{3}{4}\,a\,A\,D^2)\cos(3\,w\,t) + (\frac{3}{2}\,B^2\,a\,D + 3\,B\,E\,a\,A \\
&+ \frac{3}{4}\,C^2\,a\,D + 3\,E^2\,a\,D + \frac{3}{2}\,a\,A^2\,D + \frac{3}{4}\,a\,D^3 - 4\,w^2\,D - 2\,w\,C\,c - a\,D) \\
&\sin(2\,w\,t) + (\frac{3}{2}\,B^2\,C\,a - \frac{3}{2}\,B^2\,E\,a + \frac{3}{4}\,C^3\,a + 3\,C\,E^2\,a + \frac{3}{2}\,C\,a\,A^2 + \frac{3}{4}\,C\,a\,D^2 \\
&+ \frac{3}{2}\,E\,a\,A^2 - 4\,w^2\,C + 2\,w\,c\,D - C\,a)\cos(2\,w\,t) \\
&+ (\frac{3}{4}\,C^2\,a\,D - \frac{1}{4}\,a\,D^3)\sin(6\,w\,t) \\
&+ (-\frac{3}{2}\,B\,C\,a\,D + \frac{3}{4}\,C^2\,a\,A - \frac{3}{4}\,a\,A\,D^2)\cos(5\,w\,t) \\
&+ (\frac{1}{4}\,C^3\,a - \frac{3}{4}\,C\,a\,D^2)\cos(6\,w\,t) \\
&+ (-\frac{3}{4}\,B^2\,a\,D + \frac{3}{2}\,B\,C\,a\,A + 3\,C\,E\,a\,D + \frac{3}{4}\,a\,A^2\,D)\sin(4\,w\,t) + (-\frac{1}{4}\,B^3\,a \\
&- \frac{3}{4}\,B\,C^2\,a + 3\,B\,C\,E\,a + \frac{3}{4}\,B\,a\,A^2 + \frac{3}{4}\,B\,a\,D^2 + \frac{3}{2}\,C\,a\,A\,D + 3\,E\,a\,A\,D) \\
&\sin(3\,w\,t) \\
&+ (-\frac{3}{4}\,B^2\,C\,a - \frac{3}{2}\,B\,a\,A\,D + \frac{3}{2}\,C^2\,E\,a + \frac{3}{4}\,C\,a\,A^2 - \frac{3}{2}\,E\,a\,D^2)\cos(4\,w\,t) \\
&+ (\frac{3}{4}\,B\,C^2\,a - \frac{3}{4}\,B\,a\,D^2 + \frac{3}{2}\,C\,a\,A\,D)\sin(5\,w\,t) = f\cos(w\,t) \qquad \text{(C.89)}
\end{aligned}
$$

we now discard harmonics higher than 2ω and products $\mathcal{O}(C^2)$ or greater, and equate the remaining harmonic coefficients (and the constant terms) to zero:

$$
\begin{aligned}
&\frac{1}{2}\,E\,a\,(2\,E^2 + 3\,A^2 + 3\,B^2 - 2) = 0 \\
&\frac{3}{4}\,A^3\,a + (3\,E^2\,a - a - w^2 + 3\,E\,C\,a + \frac{3}{4}\,B^2\,a)\,A + 3\,D\,E\,B\,a + w\,B\,c - f = 0 \\
&\frac{3}{4}\,B^3\,a + (-3\,E\,C\,a + \frac{3}{4}\,A^2\,a + 3\,E^2\,a - w^2 - a)\,B + 3\,D\,E\,A\,a - A\,w\,c = 0 \\
&(3\,E^2\,a + \frac{3}{2}\,A^2\,a + \frac{3}{2}\,B^2\,a - 4\,w^2 - a)\,D + 3\,E\,A\,B\,a - 2\,w\,C\,c = 0 \\
&(3\,E^2\,a + \frac{3}{2}\,A^2\,a + \frac{3}{2}\,B^2\,a - 4\,w^2 - a)\,C + \frac{3}{2}\,E\,A^2\,a - \frac{3}{2}\,E\,B^2\,a + 2\,D\,w\,c = 0
\end{aligned}
\qquad \text{(C.90)}
$$

The above set of five equations (C.90) become equivalent to equations 4.48 to 4.52 respectively, if we replace $(A^2 + B^2)$ by Z^2.

C.2 The determinants of section 4.3

Expanding the determinant $\Delta(i)$ (equation 4.76), we obtain

$$\begin{aligned}\Delta(i) = {} & 81 - 18\theta_2{}^2 + 20\theta_2{}^2\theta_0 - 180\theta_0 + 38\theta_0\theta_1{}^2 - 36\theta_2\theta_1{}^2 + 118\theta_0{}^2 \\ & - 99\theta_1{}^2 - 3\theta_0{}^2\theta_1{}^2 - 2\theta_2{}^2\theta_1{}^2 - 2\theta_2{}^2\theta_0{}^2 + \theta_2{}^4 + 4\theta_0\theta_2\theta_1{}^2 + \theta_1{}^4 + \theta_0{}^4 \\ & - 20\theta_0{}^3 \end{aligned} \tag{C.91}$$

Expanding the determinant $\Delta(0)$ (equation 4.81), we obtain

$$\begin{aligned}\Delta(0) = {} & -528\theta_0{}^3 + 2560\theta_0{}^2 + 40\theta_0{}^4 - 56\theta_2{}^2\theta_1{}^2 + 32\theta_1{}^4 + 32\theta_2{}^4 - 112\theta_0{}^2\theta_1{}^2 \\ & - 80\theta_2{}^2\theta_0{}^2 + 2\theta_0\theta_2{}^2\theta_1{}^2 - 3\theta_0\theta_1{}^4 - 2\theta_0\theta_2{}^4 + 4\theta_0{}^3\theta_1{}^2 + 3\theta_2{}^2\theta_0{}^3 - \theta_0{}^5 \\ & - 6\theta_0{}^2\theta_2\theta_1{}^2 - 2\theta_2{}^3\theta_1{}^2 + 4\theta_2\theta_1{}^4 + 896\theta_0\theta_1{}^2 - 2048\theta_1{}^2 + 544\theta_2{}^2\theta_0 \\ & - 512\theta_2{}^2 - 768\theta_2\theta_1{}^2 - 4096\theta_0 + 144\theta_0\theta_2\theta_1{}^2 \end{aligned} \tag{C.92}$$

Bibliography

[1] H. D. I. Abarbanel, R. Brown, and M. B. Kennel. Local Lyapunov Exponents Computed from Observed Data. *J. Nonlinear Sci.*, 2:343–365, 1992.

[2] M. Abramowitz and I. A. Stegun. *Handbook of Mathematical Functions*, chapter 20. Dover, New York, 1965.

[3] G. Benettin, L. Galgani, A. Giorgilli, and J.-M. Strelcyn. Lyapunov Characteristic Exponents for Smooth Dynamical systems and for Hamiltonian Systems: A Method for Computing all of them. *Meccanica*, 15:9–30, 1980.

[4] J. E. Berger and G. Nunes, Jr. A Mechanical Duffing Oscillator for the undergraduate laboratory. *Am. J. Phys.*, 65(9):841–846, 1997.

[5] K. Briggs. An improved method for estimating Liapunov exponents of chaotic time series. *Phys. Lett. A*, 151(1,2):27–32, 1990.

[6] S. De Souza-Machado, R.W. Rollins, D.T. Jacob, and J.L. Hartman. Studying chaotic systems using microcomputer simulations and Lyapunov exponents. *Am. J. Phys.*, 58(4):321–329, 1990.

[7] G. W. Dingley, J. Wang, C. I. Reid, and S. Whineray. Sinusoidal Drive for a Nonlinear Oscillator. To be published.

[8] G. Duffing. *Erzwungene Schwingungen bei veränderlicher Eigenfrequenz und ihre technische Bedeutung.* Freidr. Vieweg and Sohn, Braunschweig, 1918.

[9] J. C. Earnshaw and D. Haughey. Lyapunov exponents for pedestrians. *Am. J. Phys.*, 61(5):401–407, 1993.

[10] K. Geist, U. Parlitz, and W. Lauterborn. Comparison of Different Methods for Computing Lyapunov Exponents. *Progress of Theoretical Physics*, 83(5):875 -893, 1990.

[11] J. Guckenheimer and P. Holmes. *Nonlinear Oscillations, Dynamical Systems, and Bifurcations of Vector Fields.* Springer-Verlag, Fourth edition, 1993.

[12] C. Hayashi. *Nonlinear Oscillations in Physical Systems.* McGraw-Hill, 1964.

[13] P. J. Holmes. A Nonlinear Oscillator with a Strange Attractor. *Philos. Trans. R. Soc. London A*, 292:419–448, 1979.

[14] K. L. Janicki and W. Szemplińska-Stupnicka. Subharmonic resonances and criteria for escape and chaos in a driven oscillator. *J. Sound Vib.*, 180(2):253–269, 1995.

[15] H. Kantz. A robust method to estimate the maximal Lyapunov exponent of a time series. *Phys. Lett. A*, 185:77–87, 1994.

[16] T. Kapitaniak. Analytical condition for chaotic behaviour of the Duffing oscillator. *Phys. Lett. A*, 144(6,7):322–324, 1990.

[17] Erwin Kreyszig. *Advanced Engineering Mathematics.* Wiley, Sixth edition, 1988.

[18] F.C. Moon. Experiments on chaotic motions of a forced nonlinear oscillator: Strange Attractors. *J. App. Mech.*, 47:638–644, 1980.

[19] F.C. Moon. Fractal Boundary for Chaos in a Two-State Mechanical Oscillator. *Phys. Rev. Lett.*, 53(10):962–964, 1984.

[20] F.C. Moon. *Chaotic Vibrations.* Wiley, 1987.

[21] A. H. Nayfeh. *Introduction to Perturbation Techniques.* Wiley, 1981.

[22] C.L. Olson and M.G. Olsson. Dynamical symmetry breaking and chaos in Duffing's equation. *Am. J. Phys.*, 59:907–911, 1991.

[23] Peter Hagedorn. *Non-Linear Oscillations.* Oxford University Press, Fourth edition, 1988.

[24] A. B. Pippard. *The Physics of Vibration*, chapter 10. Cambridge University Press, Omnibus edition, 1989.

[25] C.I. Reid and S. Whineray. The resonant response of a simple harmonic half-oscillator. *Phys. Lett. A*, 199:49–54, 1995.

[26] R. W. Rollins. *Chaotic Dynamics Workbench.* Physics Academic Software, AIP, New York, 1990.

[27] David. A. Sánchez. *Ordinary Differential Equations and Stability Theory: An Introduction.* Dover, New York, 1979.

[28] J. J. Stoker. *Nonlinear Vibrations in Mechanical and Electrical Systems*, chapter 9. Interscience, New York, 1950.

[29] Y. Ueda. Steady motions exhibited by Duffing's equation: A picture book of regular and chaotic motions. In P.J. Holmes, editor, *Proceedings of the Engineering Foundation conference on new approaches to Nonlinear Dynamics*, pages 311-322. SIAM, Philadelphia, 1979.

[30] Y. Ueda, S. Yoshida, H.B. Stewart, and J.M.T. Thompson. Basin explosions and escape phenomena in the twin-well Duffing oscillator: compound global bifurcations organizing behaviour. *Phil. Trans. R. Soc. Lond. A*, 332:169–186, 1990.

[31] VS-110 PRO. *V-scope(TM) System.* Litek Advanced Systems LTD, Israel.

[32] S. Whineray. A cube-law air track oscillator. *Eur. J. Phys.*, 12:90–95, 1991.

[33] S. Whineray, C. Rofe, and A. Ardekani. The resonant response of a cube-law air track oscillator. *Eur. J. Phys.*, 13:201–209, 1992.

[34] E. T. Whittaker and G. N. Watson. *A Course of Modern Analysis*, chapter 19. Cambridge University Press, Fourth edition, 1962.

[35] C. S. Williams. *Designing Digital Filters*, chapter 7. Prentice-Hall, 1986.

[36] A. Wolf, J.B. Swift, H.L. Swinney, and J.A. Vastano. Determining Lyapunov exponents from a time series. *Physica 16D*, pages 285--317, 1985.